


Review

# Enhancement of Electrochemical Performance of Aqueous Zinc Ion Batteries by Structural and Interfacial Design of MnO<sub>2</sub> Cathodes: The Metal Ion Doping and Introduction of Conducting Polymers <sup>†</sup>

Mikhail A. Kamenskii, Filipp S. Volkov , Svetlana N. Eliseeva , Elena G. Tolstopyatova \*   
and Veniamin V. Kondratiev

Institute of Chemistry, Saint Petersburg State University, 7/9 Universitetskaya nab,  
199034 Saint Petersburg, Russia; vkondratiev@spbu.ru (V.V.K.)

\* Correspondence: e.tolstopyatova@spbu.ru

<sup>†</sup> Dedicated to the 300th Anniversary of Saint Petersburg University.

**Abstract:** Aqueous zinc-ion batteries (AZIBs) and, in particular, Zn//MnO<sub>2</sub> rechargeable batteries have attracted great attention due to the abundant natural resources of zinc and manganese, low cost, environmental friendliness, and high operating voltage. Among the various ways to improve the electrochemical performance of MnO<sub>2</sub>-based cathodes, the development of MnO<sub>2</sub> cathodes doped with metal ions or composites of MnO<sub>2</sub> with conducting polymers has shown such advantages as increasing the specific capacity and cycling stability. This mini-review focuses on the strategies to improve the electrochemical performance of manganese-based cathodes of AZIBs.

**Keywords:** aqueous zinc-ion battery; manganese oxides; conducting polymers; composite cathodes; electrochemical performance



**Citation:** Kamenskii, M.A.; Volkov, F.S.; Eliseeva, S.N.; Tolstopyatova, E.G.; Kondratiev, V.V. Enhancement of Electrochemical Performance of Aqueous Zinc Ion Batteries by Structural and Interfacial Design of MnO<sub>2</sub> Cathodes: The Metal Ion Doping and Introduction of Conducting Polymers. *Energies* **2023**, *16*, 3221. <https://doi.org/10.3390/en16073221>

Received: 28 February 2023

Revised: 29 March 2023

Accepted: 1 April 2023

Published: 3 April 2023



**Copyright:** © 2023 by the authors. Licensee MDPI, Basel, Switzerland. This article is an open access article distributed under the terms and conditions of the Creative Commons Attribution (CC BY) license (<https://creativecommons.org/licenses/by/4.0/>).

## 1. Introduction

Since 1991, lithium-ion batteries have been at the forefront of modern science and technology in the field of energy storage materials due to their high energy density. Nevertheless, their recycling is still a global problem due to the high cost and insufficient efficiency of these processes [1,2]. In fact, the development of clean and safe metal-ion batteries with a low cost, high energy efficiency and cycle stability, and environmental friendliness, the so-called “beyond Li-ion batteries”, has attracted global attention. Among such batteries, aqueous zinc-ion batteries (AZIBs) are state-of-the-art due to their high zinc abundance, high volumetric and gravimetric theoretical capacity values (5854 mAh·cm<sup>-3</sup> and 820 mAh·g<sup>-1</sup>), safety, and non-flammability [3–7]. In addition, metallic Zn has a comparatively low redox potential (−0.76 V vs. Standard Hydrogen Electrode (SHE)), is non-toxic, and is inexpensive.

The key problem for multivalent metal-ion batteries is the selection of a suitable cathode material with high specific capacity and stable cycling performance. Bivalent zinc ions Zn<sup>2+</sup> have a strong electrostatic interaction with the host lattice, which leads to moderate Zn<sup>2+</sup> diffusion in the crystal lattice of the cathode material and consequently to unsatisfactory electrochemical properties. Among the studied cathode materials, manganese compounds have been the most widely used in the development of rechargeable AZIBs since their appearance in 2011 [8–14]. In particular, manganese dioxide MnO<sub>2</sub> occupies a leading position due to its wide variety of polymorphic phases, which allow the construction of materials with a given morphology, high theoretical specific capacity (308 mAh·g<sup>-1</sup> per one electron transfer Mn<sup>4+</sup>-Mn<sup>3+</sup> and 616 mAh·g<sup>-1</sup> per two-electron transfer Mn<sup>4+</sup>-Mn<sup>2+</sup>) and relatively high redox transition potential (≈1.3–1.5 V vs. Zn/Zn<sup>2+</sup>). Despite

all the advantages of  $\text{MnO}_2$  as a cathode material, there are two main problems that limit its further large-scale development [14,15]. First, the electrical conductivity of  $\text{MnO}_2$  is relatively low ( $\approx 5 \times 10^{-6} \text{ S}\cdot\text{cm}^{-1}$ ). The low electronic conductivity value affects the electron transport in the cathode material, reducing the rate capability and cycling stability during cycling. Second, during the one-electron redox process,  $\text{MnO}_2$  transforms to  $\text{Mn}^{3+}$ , which is unstable due to the Jahn–Teller effect and undergoes a disproportionation reaction to  $\text{Mn}^{4+}$  and  $\text{Mn}^{2+}$ . The second product has a high solubility in the aqueous solutions, leading to dissolution of the cathode material during the charge/discharge process. Third,  $\text{MnO}_2$ -based materials tend to undergo structural transformations due to the high number of polymorphs and electrostatic repulsion between  $\text{MnO}_6$  octahedra and  $\text{Zn}^{2+}$  ions. All of these drawbacks have a critical impact on the electrochemical performance, especially the cycling stability of  $\text{MnO}_2$ -based cathodes.

To overcome structural instability and suppress manganese dissolution during cycling, the addition of manganese salts to the aqueous electrolyte is widely used [16–19]. The mixed Zn–Mn aqueous electrolyte is commonly used to evaluate the electrochemical performance of  $\text{MnO}_2$  cathodes. However, in aqueous electrolytes at high potentials ( $E > 1.7 \text{ V}$  vs.  $\text{Zn}/\text{Zn}^{2+}$ ), a competitive reaction of oxygen evolution due to water oxidation may occur. A detailed study of Pourbaix diagrams of Zn–Mn aqueous solutions showed that the optimal composition of the electrolyte solution is 2 M  $\text{ZnSO}_4$  and 0.1 M  $\text{MnSO}_4$  (Figure 1) [20].

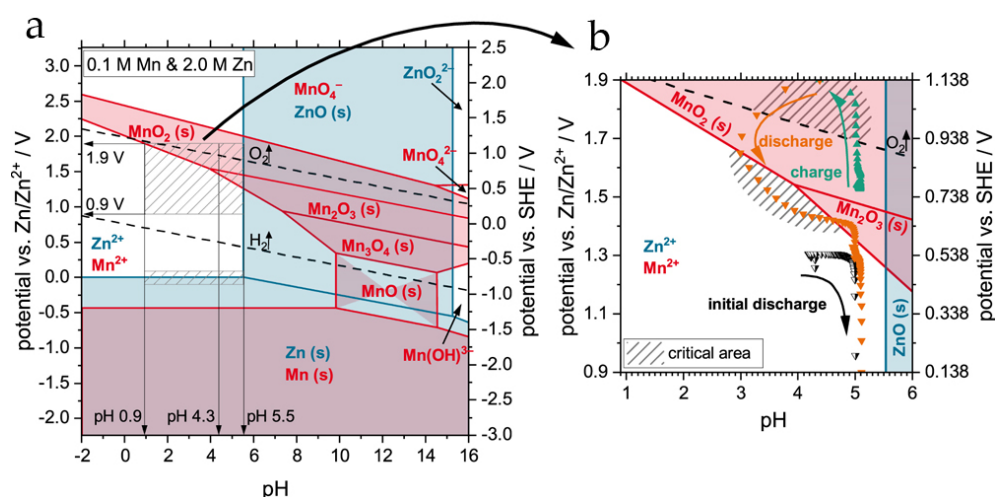


**Figure 1.** (a) Thermodynamic operating window of the zinc-ion battery with respect to the pH value. (b) Zoomed area and pH–E plot of the cycling path of the battery cell with the 2 M  $\text{ZnSO}_4$ /0.1 M  $\text{MnSO}_4$  electrolyte (positive orientation, shaded area should be avoided for cycling) [20].

To date, the studies of rechargeable aqueous Zn// $\text{MnO}_2$  batteries have accumulated a huge amount of experimental data on the electrochemical behavior of  $\text{MnO}_2$  cathodes, their structural and chemical characterization, and the approaches to improve their functional characteristics. Several strategies have been used to improve the properties of  $\text{MnO}_2$  cathodes, such as the synthesis of nanosized  $\text{MnO}_2$  with a given morphology, doping or pre-intercalation of metal ions into the manganese dioxide, oxygen defect engineering, and the development of composite materials with carbonaceous materials or conducting polymers, among others.

This mini-review focuses on a thorough analysis of the two hottest and most promising strategies for the modification of  $\text{MnO}_2$ . The first strategy is doping with metal ions, which has been the subject of a large number of recently published works. As reported in most of them, this approach resulted in an increased interlayer spacing, which allowed for improved ion intercalation kinetics. The second equally interesting strategy is the development of  $\text{MnO}_2$ -based composites with conducting polymers, which can also facilitate  $\text{Zn}^{2+}$  diffusion and increase the structural stability of the  $\text{MnO}_2$  cathodes. In addition, the combination

of these strategies was analyzed, and the structural and electrochemical properties of the modified materials were thoroughly compared.

The authors of this review deliberately limited themselves to reviewing a selected specific class of  $\text{MnO}_2$ -based cathode materials, since the review is part of a series of mini-reviews in which the role of metal ion pre-intercalation and conducting polymer can be presented as the main topic. The specific focus of this review, as opposed to the multidirectionality and similarity of many other reviews, is precisely on these aspects of cathode modification. We believe that this allows for a more in-depth analysis of the effects of the two aforementioned strategies of improvement of  $\text{MnO}_2$ -based composite cathodes, thereby emphasizing the novelty of the review.

Another important problem considered here is the issue of the complex mechanism of electrochemical transformations in aqueous  $\text{Zn}/\text{MnO}_2$  batteries. Such complexity arises due to the involvement of three types of species ( $\text{Zn}^{2+}$ ,  $\text{Mn}^{2+}$ , and  $\text{H}^+$  or water molecules). A high complexity is the presence of reversible  $\text{Zn}^{2+}$  movement into the crystal lattice of  $\text{MnO}_2$  due to high electrostatic repulsion. The most commonly described pathways of the cathodic reaction mechanism were compiled and are carefully analyzed here to find the most probable path of the electrochemical reaction.

## 2. Metal-Ions-Doped Manganese-Dioxide-Based Cathode Materials

Doping is usually defined as the introduction of a heteroatom into the structure of a host material in order to enhance its properties. It can result in interlayer doping or the substitution of Mn atoms in the lattice, depending on the initial material structure.

Metal ion doping is typically used for materials with good crystallinity, while nonmetal doping is associated with carbon-based materials [21]. In many cases, metal-ion-doped materials have increased interlayer spaces or stronger bonds between structural fragments, superior conductivity, and reduced electrostatic interaction forces, resulting in increased specific capacitance and cycling stability [22–31]. Various metal ions, such as alkali and alkaline earth metal ions ( $\text{Li}^+$ ,  $\text{Na}^+$ ,  $\text{K}^+$ , and  $\text{Ca}^{2+}$ ); transition metal ions, including VIII group metals ( $\text{Zn}^{2+}$ ,  $\text{Co}^{2+}$ , and  $\text{Cu}^{2+}$ ); rare-earth-metal ions ( $\text{La}^{3+}$  and  $\text{Ce}^{3+}$ ), and post-transition metals ( $\text{Al}^{3+}$ ,  $\text{Bi}^{3+}$ , and  $\text{Sn}^{4+}$ ), have been used as dopants for  $\text{MnO}_2$ -based cathodes.

### 2.1. Alkali and Alkaline-Earth Metal Ions

Light metal ions ( $\text{Li}^+$ ,  $\text{Na}^+$ , and  $\text{K}^+$ ) were chosen for the preparation of alkali-doped layered  $\delta\text{-MnO}_2$  cathode material [23] to decrease the additional mass of pre-intercalated cations, which can reduce the specific capacity of the material. All three materials (denoted as  $\text{Li-}\delta\text{-MnO}_2$ ,  $\text{Na-}\delta\text{-MnO}_2$ , and  $\text{K-}\delta\text{-MnO}_2$ ) were prepared by the precipitation method from the manganese chloride solution treated with  $\text{H}_2\text{O}_2$  in an alkaline environment formed by the corresponding hydroxide ( $\text{LiOH}$ ,  $\text{NaOH}$ , or  $\text{KOH}$ ) of the same concentration. Based on the XRD patterns of the synthesized materials, the layered crystal structure of birnessite ( $\delta\text{-MnO}_2$ ) was confirmed for  $\text{Li-}\delta\text{-MnO}_2$ ,  $\text{Na-}\delta\text{-MnO}_2$ , and  $\text{K-}\delta\text{-MnO}_2$ , with a small shift of the main peak to lower  $2\theta$  values, which is related to the increase of the interlayer spaces, as shown in Figure 2a. The molar ratios of the metals determined by ICP mass spectrometry were 0.42:1, 0.43:1, and 0.52:1 for K:Mn, Na:Mn, and Li:Mn pairs, respectively. The valence state of manganese in these doped materials determined from XPS spectra was 3.40, 3.42, and 3.46 for K-doped, Na-doped, and Li-doped, respectively. Scanning and transmission electron microscopy data showed that all alkali-doped materials have a two-dimensional nanosheet morphology; the structure of birnessite was further confirmed by HR-TEM and atomic force microscopy; and the interlayer spacings were determined to be 0.64, 0.55, and 0.52 nm for K-, Na-, and Li-doped materials, respectively. The electrochemical performance of these materials was tested in an aqueous solution of 2 M  $\text{ZnSO}_4/0.1$  M  $\text{MnSO}_4$ . For  $\text{Li-}\delta\text{-MnO}_2$ , the lowest specific capacity values were obtained at a current density of  $0.3 \text{ A}\cdot\text{g}^{-1}$  ( $192 \text{ mAh}\cdot\text{g}^{-1}$  after 100 cycles). At the same time,  $\text{K-}\delta\text{-MnO}_2$  delivered the highest specific capacity ( $282 \text{ mAh}\cdot\text{g}^{-1}$  after 100 cycles at  $0.3 \text{ A}\cdot\text{g}^{-1}$ ). In addition, the capacity retention for  $\text{K-}\delta\text{-MnO}_2$  and  $\text{Na-}\delta\text{-MnO}_2$  was greater than 50%, while this value was only 30% for

Li- $\delta$ -MnO<sub>2</sub> after 1000 cycles at 2.0 A·g<sup>-1</sup> (see Figure 2b). The rate performance evaluated in the current range 0.1–3.0 A·g<sup>-1</sup> was the highest for K- $\delta$ -MnO<sub>2</sub>: 270 mAh·g<sup>-1</sup> at 0.1 A·g<sup>-1</sup> and 95 mAh·g<sup>-1</sup> at 3.0 A·g<sup>-1</sup>. The reason for the superior performance of the K-doped material is the most significant interlayer expansion, which leads to facilitated ion diffusion through the crystal lattice.

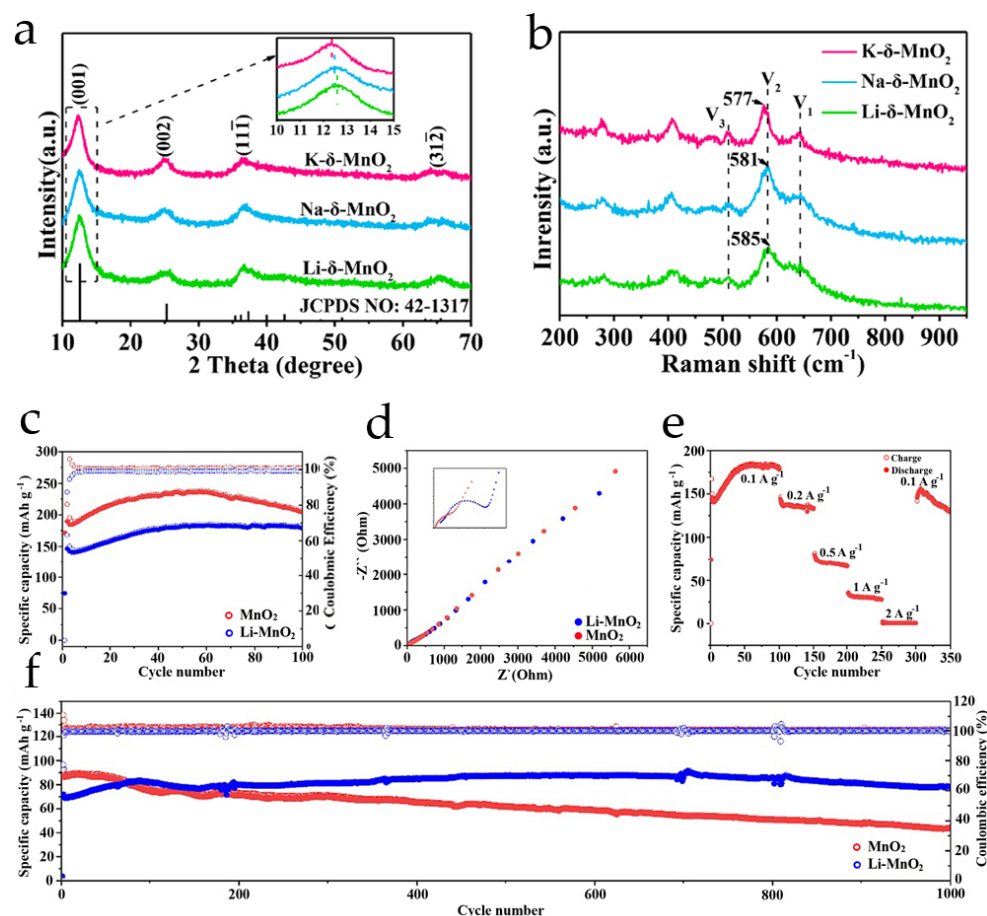


**Figure 2.** (a) XRD patterns and (b) cyclic performance at current density 0.3 A·g<sup>-1</sup> of X- $\delta$ -MnO<sub>2</sub> (X = Li, Na, K) [23]. (c) Cycling performance of MnO<sub>2</sub> and Li-MnO<sub>2</sub> electrodes at a current density of 0.1 A g<sup>-1</sup> [32]. (d) EIS spectra of MnO<sub>2</sub> and Li-MnO<sub>2</sub> at open-circuit voltage [32]. (e) Rate performance of Li-MnO<sub>2</sub> electrode at current densities from 0.1 to 2 A g<sup>-1</sup> [32]. (f) Long-term cycling performance of MnO<sub>2</sub> and Li-MnO<sub>2</sub> electrodes at a high current density of 1 A g<sup>-1</sup> [32].

Despite the rather modest electrochemical performance of lithium-doped layered-type MnO<sub>2</sub> cathode materials, Li<sup>+</sup> ions have been used as a dopant for  $\alpha$ -MnO<sub>2</sub> [32]. First, MnO<sub>2</sub> was obtained hydrothermally from KMnO<sub>4</sub> and MnSO<sub>4</sub> mixed solution, and then MnO<sub>2</sub> was transferred to organic solvent and N-butyllithium was used as lithium source to obtain Li-MnO<sub>2</sub>. The crystal structure of the tetragonal  $\alpha$ -MnO<sub>2</sub> was confirmed by XRD; the molar ratio of Li:Mn was close to 0.023:1 based on ICP emission spectroscopy. The valence state of manganese decreased from +4 to +3 after Li<sup>+</sup> insertion and more oxygen defects were observed in Li-MnO<sub>2</sub> from the XPS data. The morphology of the Li-MnO<sub>2</sub> was described as nanorods with slight lattice expansion. The crystal space in Li-MnO<sub>2</sub> expanded from 0.305 to 0.463 nm. The specific capacity values for the Li-doped material were even lower than those for the undoped manganese dioxide (185 mAh·g<sup>-1</sup> and 225 mAh·g<sup>-1</sup> at 0.1 A·g<sup>-1</sup>, respectively), while the capacity retention for Li-MnO<sub>2</sub> was close to 100% after 100 cycles at 0.1 A·g<sup>-1</sup> (Figure 2c). The artificial increase in specific capacity for Li-MnO<sub>2</sub> is associated with the deposition of an electroactive MnO<sub>x</sub> layer on the electrode surface. The charge transfer resistance evaluated from the impedance spectra

was higher for Li-MnO<sub>2</sub> (Figure 2d inset). Li-MnO<sub>2</sub> electrodes exhibited high reversibility of the charge/discharge processes at different current densities in the rate capability tests; the specific capacity recovered to 156 mAh g<sup>-1</sup> at 0.1 A·g<sup>-1</sup> after the current density of 2 A·g<sup>-1</sup> (Figure 2e). Over 1000 cycles at 1.0 A·g<sup>-1</sup>, the capacity retention for the Li-MnO<sub>2</sub> cathode was 89%, while for MnO<sub>2</sub>, only 50% of the capacity was retained; meanwhile, the coulombic efficiency was about 100% (Figure 2f).

Due to the more stable crystal lattice and enlarged crystal spaces of the Li-MnO<sub>2</sub> material, the diffusion of Zn<sup>2+</sup> and H<sup>+</sup> was facilitated despite the lower initial specific capacity and higher charge transfer resistance of the material due to the insufficient increasing of the interlayer distances and, as a consequence, high electrostatic repulsion of Zn<sup>2+</sup> ions [23].

The electrochemical deposition of Na-doped manganese oxide (Na:MnO<sub>2</sub>) on the graphene-like carbon film (GCF) was performed in [33]. The GCF was synthesized from the pristine graphite film via the electrochemical intercalation process, as shown in Figure 3a. The electrodeposition of Na:MnO<sub>2</sub> was performed at E = 1.2 V (vs. Ag/AgCl) for 400 s in a three-electrode cell from 0.1 M Na<sub>2</sub>SO<sub>4</sub> and 0.05 M MnSO<sub>4</sub> aqueous solution. The SEM images showed the uniform distribution of the deposited Na:MnO<sub>2</sub> nanosheets on the graphene sheets (Figure 3b), and the uniform distribution was also confirmed by an EDX analysis. The layered structure of the doped material was confirmed by the XRD diffraction pattern of the Na:MnO<sub>2</sub>/GCF, which was indexed to birnessite-type MnO<sub>2</sub> (Figure 3c). The peak at 1070.9 eV in the Na 1s XPS spectra (Figure 3d) confirmed the doping of MnO<sub>2</sub> by Na. The Na:Mn ratio was 0.15:1 based on ICP/atomic-emission-spectroscopy data. The resulting Na:MnO<sub>2</sub>/GCF composite was used as a binder-free electrode for further electrochemical tests. The binder-free Na:MnO<sub>2</sub>/GCF electrode in 2 M ZnSO<sub>4</sub>/0.1 M MnSO<sub>4</sub> aqueous electrolyte achieved the specific capacity of 382 mAh·g<sup>-1</sup> at 0.1 A·g<sup>-1</sup>, and at the high current density of 3.0 A·g<sup>-1</sup>, the specific capacity was 95 mAh·g<sup>-1</sup>. The capacity retention of Na:MnO<sub>2</sub>/GCF was 83% over 100 cycles at 0.1 A·g<sup>-1</sup>, and 75% over 1000 cycles at 1.0 A·g<sup>-1</sup>. This outstanding performance was associated with the highly porous 3D structure of the Na:MnO<sub>2</sub>/GCF composite and stronger electrostatic attractions between the Zn<sup>2+</sup> and MnO<sub>2</sub> lattice due to the presence of Na, which was confirmed by first-principles DFT calculations.

The doping of MnO<sub>2</sub> with potassium ions is the most commonly used strategy, especially for materials with a birnessite structure [28,34–36], because KMnO<sub>4</sub>, as a raw material, acts as a source of K<sup>+</sup> and Mn<sup>4+</sup> at the same time. Due to this fact, almost all birnessite-type structures have potassium ions in the interlayer spaces. By introducing the K<sup>+</sup> ions and oxygen defects into the crystal lattice, the electrochemical performance of MnO<sub>2</sub>-based materials was improved; e.g., the specific capacity was increased to 270–300 mAh·g<sup>-1</sup> at 0.1 A·g<sup>-1</sup> [34,35].

One of the strategies to prepare potassium-enriched MnO<sub>2</sub> (KMO) is the hydrothermal treatment of as-synthesized birnessite in KOH solution [36]. This allowed the crystal lattice of birnessite to be preserved, while the K:Mn ratio was 0.29:1, and the interlayer spacing was increased from 6.8 to 7.4 Å. The specific capacity values of KMO at I = 0.2 A·g<sup>-1</sup> and I = 3.0 A·g<sup>-1</sup> were 300 and 136 mAh·g<sup>-1</sup>, respectively. The capacity retention of KMO at I = 0.2 A·g<sup>-1</sup> was 92% during 500 cycles and 98% after 12,000 cycles at I = 2 A·g<sup>-1</sup>.

Another crystal structure that can be easily doped by K<sup>+</sup> ions is α-MnO<sub>2</sub>. Hydrothermal or polyol syntheses have been used to deposit K-doped manganese dioxide with a K<sup>+</sup> content less than 0.2 on different carbon substrates [37–39]. The morphology of the samples mainly depended on the substrate: nanotubes [37], nanoflowers [38], or nanowires [39]. It is interesting to note that α-K<sub>0.19</sub>MnO<sub>2</sub> nanotubes grown on the carbon nanofibers delivered 270 mAh·g<sup>-1</sup> at 1 C (1 C = 0.308 A·g<sup>-1</sup>) in 3 M Zn(CF<sub>3</sub>SO<sub>3</sub>)<sub>2</sub>/0.2 M Mn(CF<sub>3</sub>SO<sub>3</sub>)<sub>2</sub> electrolyte, while at 20 C, the specific capacity was as high as 113 mAh·g<sup>-1</sup>, and the capacity retention over 50 cycles at 1 C was 78%. The presence of K<sup>+</sup> ions in the electrolyte was shown to improve the cycling stability. The addition of 3 M K(CF<sub>3</sub>SO<sub>3</sub>) to the electrolyte allowed the researchers to increase the cycling stability at moderate C-rates: 98.5% of capacity retention

was achieved after 50 cycles at 1 C, 92% after 200 cycles at 2 C, and 90% after 400 cycles at 5 C [37].

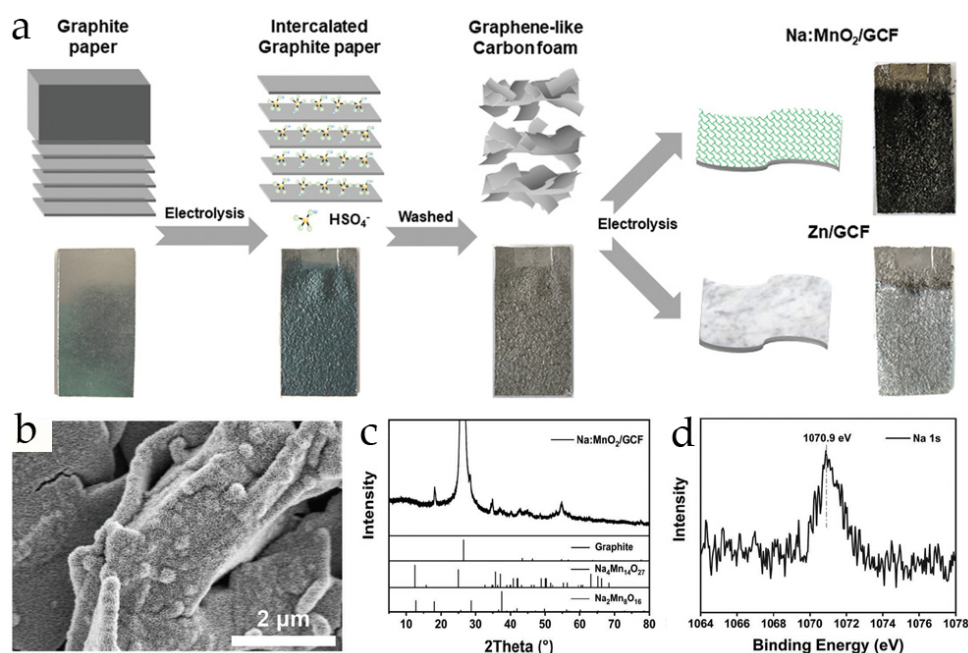


**Figure 3.** (a) The synthesis scheme of the GCF from the raw graphite paper and the photographs of the samples through the synthesis route. (b) The surface SEM of the Na:MnO<sub>2</sub>/GCF electrode. (c) XRD patterns of the Na:MnO<sub>2</sub>/GCF electrode. (d) Na 1s core-level XPS spectra of the Na:MnO<sub>2</sub>/GCF electrode [33].

K-doped MnO<sub>2</sub> (K<sub>0.15</sub>MnO<sub>2</sub> and K<sub>0.23</sub>MnO<sub>2</sub>) was grown via an in situ hydrothermal reaction on layered graphite paper (LGP) as a reaction template (Figure 4a). The conductive LGP substrate was preliminarily obtained by electrochemical treatment of the graphite paper. LGP@K<sub>0.15</sub>MnO<sub>2</sub> exhibited a nanoflower morphology consisting of interconnected nanosheets that were deposited in the interlayer spaces of LGP (Figure 4b,c). According to BET measurements, the LGP@K<sub>0.15</sub>MnO<sub>2</sub> had a higher specific surface area (20.881 m<sup>2</sup>/g) and pore volume (0.192 cm<sup>3</sup>/g) than K<sub>0.23</sub>MnO<sub>2</sub>. The resulting binder-free LGP@K<sub>x</sub>MnO<sub>2</sub> cathodes were tested in a 2 M ZnSO<sub>4</sub>/0.1 M MnSO<sub>4</sub> aqueous electrolyte. To investigate the effect of the conductive substrate on the electrochemical performance of the binder-free electrode, K<sub>x</sub>MnO<sub>2</sub> was also deposited on the carbon cloth to obtain CC@K<sub>x</sub>MnO<sub>2</sub>. The LGP@K<sub>0.15</sub>MnO<sub>2</sub> was shown to outperform K<sub>0.23</sub>MnO<sub>2</sub> and CC@K<sub>x</sub>MnO<sub>2</sub> in rate capability tests (Figure 4d). At a low current density of 0.05 A·g<sup>-1</sup>, the specific capacity value of LGP@K<sub>0.15</sub>MnO<sub>2</sub> was 403 mAh·g<sup>-1</sup>, and at I = 2.0 A·g<sup>-1</sup>, it was 116.1 mAh·g<sup>-1</sup>. The capacity retention over 100 cycles at I = 0.2 A·g<sup>-1</sup> was 92.5% (Figure 4e) [38]. Potassium-doped MnO<sub>2</sub> (KMO) nanowires grown on carbon nanotubes mixed with graphene substrate, when used as a binder-free electrode, delivered 360 mAh·g<sup>-1</sup> at 0.05 A·g<sup>-1</sup> due to the presence of highly conductive substrate and high concentration of Mn<sup>2+</sup> (0.4 M MnSO<sub>4</sub>) in the electrolyte [39].

Calcium-doped MnO<sub>2</sub> was prepared by hydrothermal method from mixed manganese solution (KMnO<sub>4</sub> + MnSO<sub>4</sub>) in the presence of calcium chloride [40]. The crystal structure of the obtained product (CaMnO) corresponded to layered-type δ-MnO<sub>2</sub> with increased interlayer space due to the presence of Ca<sup>2+</sup> ions. The Ca:Mn ratio calculated from the XPS data was 0.24:1, and 33% of the Mn was in the +3 valence state. The more accurate Ca:Mn ratio determined by ICP-OES was 0.28:1. According to the SEM-characterization, CaMnO was composed of nanorods and nanospheres that were formed by uniform interconnected nanoflakes. The initial specific capacity of CaMnO electrodes in 1 M ZnSO<sub>4</sub>/0.1 M MnSO<sub>4</sub> aqueous solution at a current density of 0.35 A·g<sup>-1</sup> was 277.7 mAh·g<sup>-1</sup>, and at 3.5 A·g<sup>-1</sup>, it

was  $124.5 \text{ mAh}\cdot\text{g}^{-1}$ . After 5000 cycles at  $3.5 \text{ A}\cdot\text{g}^{-1}$ , the retained capacity was  $100.9 \text{ mAh}\cdot\text{g}^{-1}$  (81%), which is quite good for AZIBs. The electrolyte pH was shown to significantly affect the electrochemical performance of  $\text{CaMnO}$ . In acetate solution ( $1 \text{ M ZnAc}_2/0.1 \text{ M MnAc}_2$ ) at  $I = 1.5 \text{ A}\cdot\text{g}^{-1}$ , the cycling stability was much lower than in sulfate-based solution (only 39.4% of capacity retention was observed over 500 cycles).

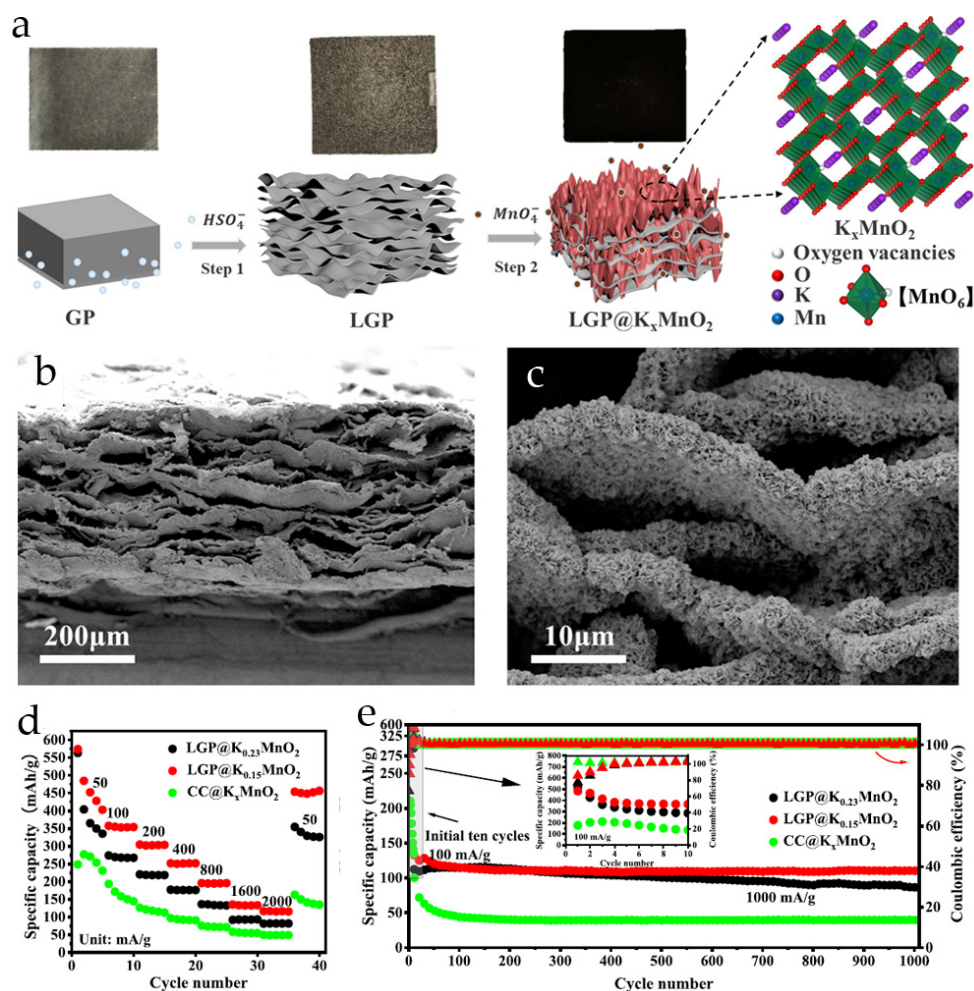


**Figure 4.** (a) Scheme of the preparation process of LGP and synthesis of  $\text{LGP}@K_x\text{MnO}_2$ . (b,c) The cross-sectional SEM images of  $\text{LGP}@K_{0.15}\text{MnO}_2$ . (d) Rate performance and (e) cycling stability and coulombic efficiency at 1000 mA/g of K-doped  $\text{MnO}_2$  grown on the layered graphite paper and carbon cloth [38].

Thus, alkali and alkaline earth metal ions are quite suitable dopants for  $\text{MnO}_2$ -based cathode materials due to their ability to increase the interlayer spacing in tunnel or layered crystal structures. As can be seen from the ionic radii,  $\text{Li}^+$  ions have an insufficient effect on the electrochemical performance of cathode materials due to their negligible effect on the crystal lattice spacing, while the use of sodium or potassium ions endowed the doped  $\text{MnO}_2$ -based cathodes with superior properties. The use of divalent  $\text{Ca}^{2+}$  ions with an ionic radius close to that of  $\text{K}^+$  as a dopant allows a significant improvement in cycling stability due to the stronger bonding of the dopant ion to the oxygen in the  $\text{MnO}_6$  octahedra. In this case, the increase in interlayer spacing due to doping resulted in superior capacity values, and the interaction of the dopant with the host lattice influenced the stability during long-term cycling.

## 2.2. Transition and Rare-Earth-Metal Ions

### 2.2.1. Light Transition Metal Ions

Among the different metal ions, the pre-intercalation of  $Zn^{2+}$  into the  $MnO_2$  crystal lattice is an attractive way to improve the electrochemical performance due to  $Zn^{2+}$  intended reversible insertion/extraction into the  $MnO_2$  host during the cycling process in Zn-containing electrolytes. In particular,  $Zn^{2+}$  ions were inserted into layered  $MnO_2$  to stabilize the host structure by a simple reaction between  $KMnO_4$  solution and Zn powder in acidic media [41]. The birnessite-type  $\delta$ - $MnO_2$  structure of the obtained product was confirmed by XRD, and a typical flower-like morphology of the sample consisting of ultrathin nanosheets was observed. The incorporation of  $Zn^{2+}$  ions into the tunnels between  $MnO_2$  layers was confirmed by the XPS data, and the Zn:Mn ratio was 0.16:1. The specific capacities of Zn-doped  $MnO_2$  in the conventional mixed 2 M  $ZnSO_4$ /0.1 M  $MnSO_4$  aqueous electrolyte were  $275 \text{ mAh}\cdot\text{g}^{-1}$  at the low current density of  $0.3 \text{ A}\cdot\text{g}^{-1}$ , and  $121 \text{ mAh}\cdot\text{g}^{-1}$  after a tenfold increase in current density. This excellent rate performance was attributed to the nanostructure of the material, with nanospheres having a high specific surface area ( $178 \text{ m}^2\cdot\text{g}^{-1}$ ) and providing more active sites and diffusion channels. The cyclic stability of the material was investigated at current densities of 0.3, 1.0, and  $3.0 \text{ A}\cdot\text{g}^{-1}$  during 100, 500, and 2000 cycles, respectively. In the absence of the  $Mn^{2+}$  additive in the solution, a rapid capacity fading (more than 50%) was observed at  $0.3 \text{ A}\cdot\text{g}^{-1}$  during 100 cycles. However, in the presence of  $MnSO_4$ , a gradual increase in capacity was observed under the same conditions, and this is associated with the reoxidation of  $Mn^{2+}$  from the electrolyte solution. Increasing the current allowed the stabilization of the cell, and the capacity retention was greater than 90% in both cases. Thus, the presence of pre-intercalated  $Zn^{2+}$  ions led to the stability of the host material with the formation of a mesoporous flower-like morphology that facilitated reversible  $Zn^{2+}/H^+$  insertion/extraction.

To improve the electronic conductivity of the Zn-doped  $MnO_2$  cathode, the oxide was deposited from  $KMnO_4$  solution with HCl and  $Zn(NO_3)_2$  in the presence of graphene quantum dots to obtain a  $GQDs@Zn_xMnO_2$  composite, as shown in Figure 5a [42]. According to the SEM image (Figure 5b), the composite material consisted of monodispersed and uniform nanoflowers, GQDs were formed on the Zn-doped  $MnO_2$  surface. The crystal structure of the ternary composite matched to the layered-type  $\delta$ - $MnO_2$ . During the insertion of  $Zn^{2+}$  into the  $MnO_2$  lattice, a partial decrease of the valence state from  $Mn^{4+}$  to  $Mn^{3+}$  was observed from the XPS data. The electrochemical performance of  $GQDs@Zn_xMnO_2$  in 1 M  $ZnSO_4$  aqueous solution was remarkable compared to other Mn-based cathodes:  $404 \text{ mAh}\cdot\text{g}^{-1}$  at  $0.3 \text{ A}\cdot\text{g}^{-1}$ ,  $211 \text{ mAh}\cdot\text{g}^{-1}$  at  $4.0 \text{ A}\cdot\text{g}^{-1}$ , and the capacity retention of 88% after 500 cycles at  $1.0 \text{ A}\cdot\text{g}^{-1}$  was observed (Figure 5c). The polarization value, defined as the difference between the cathodic and anodic peak potentials on the cyclic voltammograms, was lower in the case of the  $GQDs@Zn_xMnO_2$  composite compared to the pristine  $MnO_2$  (Figure 5d). Thus, the modification of  $MnO_2$  by GQDs and the Zn intercalation are responsible for providing active sites and conductive media for electron/ion transfer and for such high specific capacity values of the  $GQDs@Zn_xMnO_2$  composite.

The mixed  $Mn_3O_4$ - $MnO_2$  oxide was modified with  $Zn^{2+}$  ions to induce the electronic and ionic conductivity of the composite material [27]. This composite material was electrodeposited on the Ni foam coated with silver-nanoparticle-modified carbon nanotubes (AgCNT-Ni). The AgCNT coating was used to enhance the interactions between the substrate and the deposited manganese oxides; the structure of the resulting composite is shown in Figure 5e. Electrodeposition was performed in the mixed solution of  $MnSO_4$  and  $ZnSO_4$  at  $E = -1.8 \text{ V}$  (vs. Ag/AgCl). As a result, Zn-doped  $Mn_3O_4$ - $MnO_2$  vertical nanosheets were formed, as was observed in the SEM images. The analysis of the crystalline phase composition showed that the material consisted of  $Mn_3O_4$  and  $\gamma$ - $MnO_2$ , without any impurities. The valence states of manganese ( $Mn^{2+}$ ,  $Mn^{3+}$ , and  $Mn^{4+}$ ) and the presence of  $Zn^{2+}$  ions were confirmed by XPS data. The specific capacity of this binder-free composite cathode material, obtained in aqueous solution of 2 M  $ZnSO_4$ /0.1 M  $MnSO_4$  at a low current density ( $0.3 \text{ A}\cdot\text{g}^{-1}$ ), was  $562.1 \text{ mAh}\cdot\text{g}^{-1}$ . This value surpassed almost all results



obtained for MnO<sub>2</sub>-based cathodes, and even at  $I = 6.0 \text{ A}\cdot\text{g}^{-1}$ , the composite retained the specific capacity of  $272.7 \text{ mAh}\cdot\text{g}^{-1}$  (Figure 5f). Despite this brilliant rate performance, the cycling stability of the composite at  $3.0 \text{ A}\cdot\text{g}^{-1}$  was much lower than reported for other materials: only 69.4% of capacity retention after 200 cycles. However, it was much better than for the Zn<sup>2+</sup>-undoped material, where the capacity fading after 200 cycles was 39%. These remarkable properties of the Zn<sup>2+</sup>-doped Mn<sub>3</sub>O<sub>4</sub>-MnO<sub>2</sub> composite cathode were attributed to the complex 3D porous structure of the binder-free electrode, which facilitates Zn<sup>2+</sup> transport due to zinc doping and multiple valence states of manganese, favoring fast redox reactions and a high rate performance.

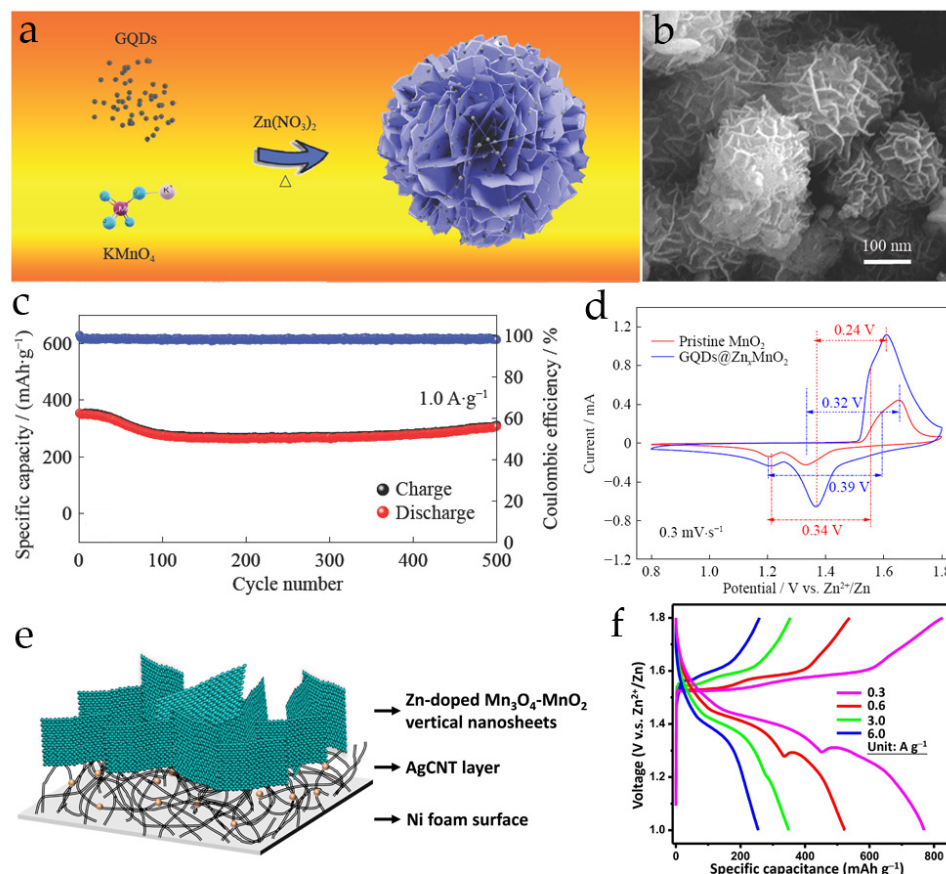


**Figure 5.** (a) Scheme of the synthesis route for GQDs@Zn<sub>x</sub>MnO<sub>2</sub> composite [42]. (b) SEM image of GQDs@Zn<sub>x</sub>MnO<sub>2</sub> [42]. (c) Long-term cycling of GQDs@Zn<sub>x</sub>MnO<sub>2</sub> electrode [42]. (d) Comparison of the cyclic voltammograms for pristine MnO<sub>2</sub> and GQDs@Zn<sub>x</sub>MnO<sub>2</sub> cathodes [42]. (e) Schematic illustration of the structure of fabricated Zn-doped mixed Mn<sub>3</sub>O<sub>4</sub>-MnO<sub>2</sub> nanosheets on the AgCNT-modified Ni foam [27]. (f) Galvanostatic charging/discharging profiles of Zn-doped Mn<sub>3</sub>O<sub>4</sub>-MnO<sub>2</sub> vertical nanosheets [27].

Vanadium ions can be easily inserted into the MnO<sub>2</sub> lattice due to the close ionic radii of V<sup>5+</sup> (0.53 Å) and Mn<sup>4+</sup> (0.54 Å), and V-doped MnO<sub>2</sub> was successfully synthesized via ambient redox reaction [25]. The solution of KMnO<sub>4</sub> was mixed with Mn(CH<sub>3</sub>COO)<sub>2</sub> containing a small amount of dissolved V<sub>2</sub>O<sub>5</sub> under continuous stirring. The crystal structure of the V-doped material was defined as tetragonal  $\alpha$ -MnO<sub>2</sub>, with a slight shift of the characteristic XRD peaks to lower angles. Based on ICP-AES measurements, the V:Mn ratio was calculated to be 0.05:1. The valence state of vanadium was defined as V<sup>5+</sup> according to the XPS results. The electrochemical tests performed in 1 M ZnSO<sub>4</sub> showed that the initial specific capacity value for V-doped MnO<sub>2</sub> was  $266 \text{ mAh}\cdot\text{g}^{-1}$  at  $I = 0.066 \text{ A}\cdot\text{g}^{-1}$ , while for undoped MnO<sub>2</sub>,  $213 \text{ mAh}\cdot\text{g}^{-1}$  was achieved at the same current density. Increasing the current to  $1.06 \text{ A}\cdot\text{g}^{-1}$  resulted in a significant decrease in the

capacity of V-doped  $\text{MnO}_2$  to  $67 \text{ mAh}\cdot\text{g}^{-1}$ . The capacity retention at the low current of  $0.066 \text{ A}\cdot\text{g}^{-1}$  after 100 cycles was close to 50%. The improved specific capacity and rate performance of V-doped  $\text{MnO}_2$  were explained by an increase in the conductivity of  $\text{MnO}_2$  after doping, and this was further evidenced by a decrease of the charge-transfer resistance in the impedance spectra.

V-doped  $\text{MnO}_2$  aerogel was obtained via the coprecipitation method from dissolved  $\text{V}_2\text{O}_5$  gel solution with  $\text{MnSO}_4$ , which was then oxidized with  $(\text{NH}_4)_2\text{S}_2\text{O}_8$ , under continuous stirring [43]. The resulting aerogel (A- $\text{MnO}_2$ ) had a crystalline structure of birnessite and was composed of ultrathin nanosheets with many wrinkles. According to the XPS survey spectrum, A- $\text{MnO}_2$  consisted of Mn, V, and O elements, and the molar ratio of V:Mn was 0.07:1. The valence state of vanadium was  $\text{V}^{5+}$ , and manganese had two valence states,  $\text{Mn}^{3+}$  and  $\text{Mn}^{4+}$ , that are typical of doped materials. The electrochemical performance was evaluated in 2 M  $\text{ZnSO}_4$  aqueous solution without manganese additive. The initial specific capacity of A- $\text{MnO}_2$  at  $0.2 \text{ A}\cdot\text{g}^{-1}$  was  $194 \text{ mAh}\cdot\text{g}^{-1}$ , and at  $I = 2.0 \text{ A}\cdot\text{g}^{-1}$ , the capacity was  $74 \text{ mAh}\cdot\text{g}^{-1}$ . The cyclic performance of A- $\text{MnO}_2$  evaluated at  $0.3 \text{ A}\cdot\text{g}^{-1}$  during 100 cycles showed the capacity retention of 71%, with a small capacity growth attributed to the activation of the cathode, including a better infiltration of the electrolyte into the porous material. The addition of 0.1 M  $\text{MnSO}_4$  to the electrolyte solution increased the battery lifetime by a factor of six, indicating that the  $\text{Mn}^{2+}$  additive has a crucial effect on the manganese dissolution during the cycling process. The improvement of the V-doped material was mainly explained by the oxygen defects, high conductivity, and porosity of A- $\text{MnO}_2$ .

Group VIII metals (Fe, Co, and Ni) can be used as dopants for  $\text{MnO}_2$  due to their ability to suppress the Jahn–Teller effect, which leads to a decrease in manganese disproportionation and consequent dissolution [44]. Fe-doped manganese oxide (FMO) was obtained hydrothermally from potassium permanganate solution in the presence of iron nitrate. According to X-ray diffraction data, the product had a birnessite-type  $\delta\text{-MnO}_2$  crystalline structure, and the characteristic peaks of FMO were broadened and lower in intensity compared to those of undoped  $\text{MnO}_2$  due to an increase in lattice disorder caused by Fe doping (Figure 6a). However, the nanoflower-like morphology, which is typical of birnessite-type structures, was still maintained after Fe-doping (Figure 6b). The EDX analysis showed a uniform distribution of Mn, O, and Fe elements in the FMO sample. The HRTEM images (Figure 6c) show the distinct lattice fringes with a spacing of 0.714 nm, which can be indexed to the (001) plane of  $\text{MnO}_2$ . The survey XPS spectra showed the presence of Mn and Fe peaks, confirming the intercalation of Fe into the  $\text{MnO}_2$  structure. The analysis of the valence states of manganese and iron had shown that only a small part of  $\text{Mn}^{4+}$  was reduced to  $\text{Mn}^{3+}$  after the insertion of  $\text{Fe}^{3+}$ . The electrochemical properties of FMO as a cathode material were investigated in the aqueous solution of 2 M  $\text{ZnSO}_4/0.1 \text{ M MnSO}_4$ . The initial specific capacity of FMO at a current density of  $0.1 \text{ A}\cdot\text{g}^{-1}$  was  $170 \text{ mAh}\cdot\text{g}^{-1}$ , and it increased twice by the third cycle due to the activation process. The maximum specific capacity delivered by FMO at  $I = 0.1 \text{ A}\cdot\text{g}^{-1}$  was  $390 \text{ mAh}\cdot\text{g}^{-1}$ , and after increasing the current to  $3.0 \text{ A}\cdot\text{g}^{-1}$ , this value was  $160 \text{ mAh}\cdot\text{g}^{-1}$ . This was explained by the inhibition of Jahn–Teller distortion due to the increase in the mean valence of manganese after Fe intercalation and the suppression of manganese dissolution. The influence of this effect on the cycling stability was demonstrated at the current density of  $1.0 \text{ A}\cdot\text{g}^{-1}$  during 200 cycles, when the capacity retention of 86.3% was observed. Thus, pre-intercalation of  $\text{MnO}_2$  with Fe ions stabilized its crystal structure and resulted in superior electrochemical performance.

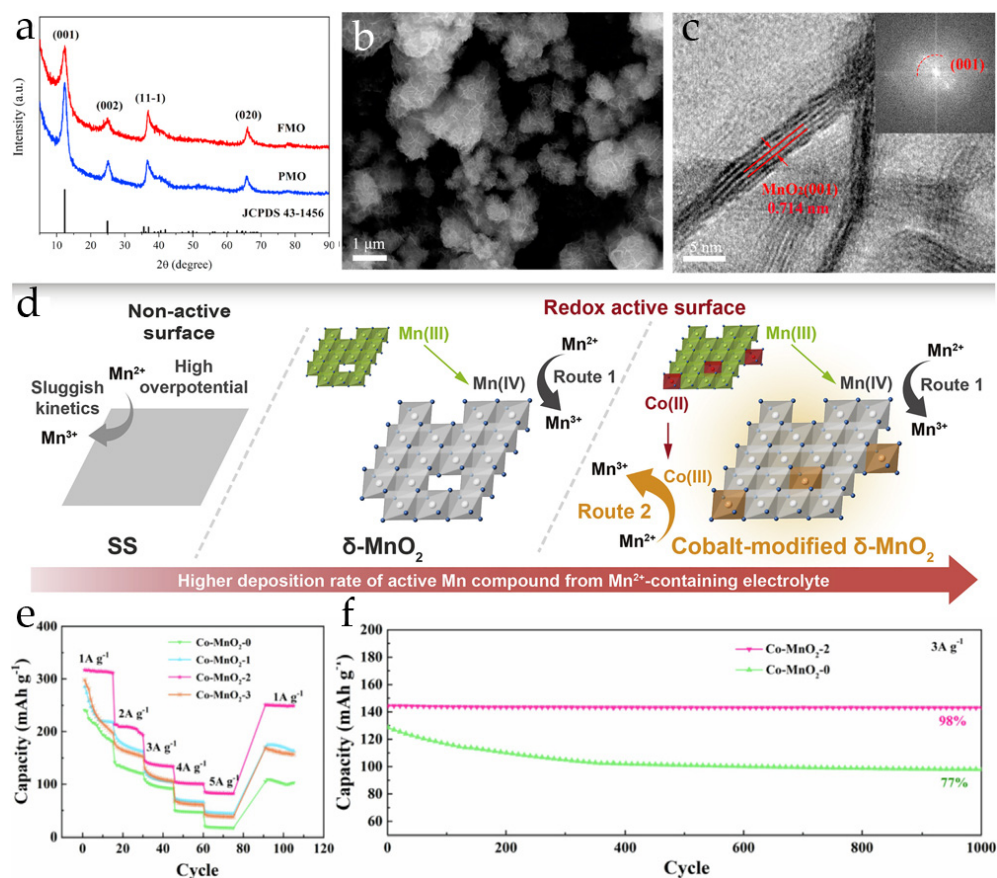


**Figure 6.** (a) XRD spectra of pristine MnO<sub>2</sub> and FMO [44]. (b) SEM image of FMO [44]; (c) HRTEM image of FMO [44]. (d) The mechanism of the catalysis effect in Co-modified  $\delta$ -MnO<sub>2</sub> [45]. (e) Rate performance of plasma-treated Co-MnO<sub>2</sub>-X (X = treatment time) at current densities 1–5 A·g<sup>-1</sup> [29]. (f) Cycling performance of Co-MnO<sub>2</sub>-0 and Co-MnO<sub>2</sub>-2 at 3 A·g<sup>-1</sup> [29].

Cobalt ions are the most widely used dopant for MnO<sub>2</sub> cathodes among other Group VIII metals [26,29,45,46]. For chemical modification, the as-synthesized MnO<sub>2</sub> powder was treated with aqueous CoCl<sub>2</sub> solution under continuous stirring [45]. The XRD pattern of the obtained Co-doped MnO<sub>2</sub> product was consistent with the  $\delta$ -MnO<sub>2</sub> crystal structure, and the product had a flower-like morphology and uniform distribution of the Mn, O, and Co elements according to the SEM and EDX results. The rate performance tests in mixed zinc–manganese aqueous electrolyte showed that Co-doped MnO<sub>2</sub> had the lowest initial capacity values in the potential range of 1.0–1.8 V compared to unmodified  $\delta$ -MnO<sub>2</sub> (196 and 252 mAh·g<sup>-1</sup> at 0.1 A·g<sup>-1</sup>, respectively), but the most intensive capacity growth was observed during continuous cycling at 0.3 A·g<sup>-1</sup>. It was shown that cobalt ions catalyzed the MnO<sub>2</sub> electrodeposition during cycling, resulting in a stabilization of the specific capacity over 5000 cycles at I = 2.0 A·g<sup>-1</sup> with a capacity retention of 80%. This catalytic mechanism was proposed based on the comproportionation between Mn<sup>2+</sup> and Mn<sup>4+</sup> and the reversible oxidation of Co<sup>2+</sup> to Co<sup>3+</sup> at E < 1.85 V (Figure 6d).

Another way to obtain Co-doped MnO<sub>2</sub> is a hydrothermal synthesis from KMnO<sub>4</sub> solution in the presence of Co(NO<sub>3</sub>)<sub>2</sub> on a carbon cloth in an acidic environment; the product was further treated by plasma to obtain vacancy-rich Co-MnO<sub>2</sub> [29]. The crystal structure of Co-MnO<sub>2</sub> was defined as  $\alpha$ -MnO<sub>2</sub> before and after plasma treatment. The Co-MnO<sub>2</sub> had a nanowire-like morphology and was uniformly distributed on the carbon cloth substrate. The valence states of manganese evaluated from the XPS data were Mn<sup>4+</sup> and Mn<sup>3+</sup>, and for Co, the mixed-valence state, consisting of Co<sup>2+</sup> and Co<sup>3+</sup>, was detected. The concentration of oxygen vacancies after the plasma treatment, calculated from O 1s spectra, was 19–29%, depending on the treatment time (1–3 min), with 2 min being the optimal time

(29%). The electrochemical performance of vacancy-rich binder-free Co-MnO<sub>2</sub> cathodes was tested in 2 M ZnSO<sub>4</sub>/0.1 M MnSO<sub>4</sub> aqueous solution. The initial specific capacity at a current density of 0.5 A·g<sup>-1</sup> was 511 mAh·g<sup>-1</sup>. At a high current density of 5.0 A·g<sup>-1</sup>, the delivered specific capacity of plasma-treated Co-MnO<sub>2</sub>-2 was 100 mAh·g<sup>-1</sup>, which is about 25% higher than that of Co-doped MnO<sub>2</sub> without additional oxygen defects (Co-MnO<sub>2</sub>-0) (Figure 6e). The capacity retention for plasma-treated Co-MnO<sub>2</sub>-2 over 1000 cycles at I = 3.0 A·g<sup>-1</sup> was 98% (Figure 6f). Therefore, Co-doping, together with the formation of oxygen vacancy-rich structures, had the synergistic effect of inhibiting the Jahn–Teller effect and increasing the conductivity and performance of the material.

Electrodeposition of Co-doped MnO<sub>2</sub> has also been used to develop binder-free cathodes for Zn//MnO<sub>2</sub> batteries [26,46]. To overcome the poor conductivity of MnO<sub>2</sub>, Co-doped oxide was grown on the carbon cloth from a solution of MnSO<sub>4</sub>, ZnSO<sub>4</sub>, and CoSO<sub>4</sub> at E = 1.0 V (vs. Ag/AgCl) [26]. Under these conditions, Zn<sup>2+</sup>-intercalated Co-doped δ-MnO<sub>2</sub> with a birnessite-type structure was obtained. The XPS analysis confirmed that Co and Zn atoms were incorporated into the material structure, the valence state of Co was Co<sup>3+</sup>, and these Co<sup>3+</sup> ions were inserted into the layers of MnO<sub>6</sub> octahedra, not between them. The intercalation of Co<sup>3+</sup> significantly improved the rate capability of the Co-MnO<sub>2</sub> film: 280 mAh·g<sup>-1</sup> at 1.2 A·g<sup>-1</sup> and 205 mAh·g<sup>-1</sup> at I = 3.0 A·g<sup>-1</sup> were achieved. During 200 cycles at 1.2 A·g<sup>-1</sup>, a rapid capacity increase from 60 to 290 mAh·g<sup>-1</sup> was observed, with a consequent capacity fading of 8% only in the last few cycles. The charge-transfer resistance of the Co-MnO<sub>2</sub> material, evaluated from the impedance spectra, was five times lower than that of the undoped material. The reason for these remarkable electrochemical properties of Co-doped MnO<sub>2</sub> is the increased electrical conductivity of the material after Co<sup>3+</sup> intercalation.

The electrochemical synthesis on the stainless-steel mesh from solution of MnSO<sub>4</sub> and Na<sub>2</sub>SO<sub>4</sub> in the presence of Co(CH<sub>3</sub>COO)<sub>2</sub> at E = −1.8 V (vs. SCE) allowed researchers to obtain layered-type Co-MnO<sub>2</sub> [46]. The valence states of Mn and Co were investigated by XPS, and, after doping, the manganese had a mixed valence of Mn<sup>3+</sup> and Mn<sup>4+</sup>, while for cobalt, only one valence state, Co<sup>3+</sup>, was observed. The electrochemical tests were carried out in a mixed zinc–manganese electrolyte, with and without the addition of 0.02 M Co(CH<sub>3</sub>COO)<sub>2</sub>, to check the possibility of additional electrochemical intercalation of Co. The presence of Co<sup>2+</sup> ions in the electrolyte solution had a positive effect on the specific capacity in the current range of 1.0–3.0 A·g<sup>-1</sup>: 310 mAh·g<sup>-1</sup> and 175 mAh·g<sup>-1</sup> at I = 1.0 and 3.0 A·g<sup>-1</sup>, respectively, while the same cathode in the solution without cobalt additive showed 260 and 145 mAh·g<sup>-1</sup> at the same current densities. The capacity retention in the ternary electrolyte solution over 1000 cycles at I = 1.0 A·g<sup>-1</sup> was 91.78%. Thus, a synergistic combination of a Co-doped MnO<sub>2</sub> cathode and a Co<sup>2+</sup> electrolyte additive allowed the rate and cycle performance of the electrodeposited material to be significantly increased.

Nickel has also been used to develop doped MnO<sub>2</sub>-based cathodes [44,47]. Ni-doped MnO<sub>2</sub> was prepared hydrothermally from a mixed solution of KMnO<sub>4</sub> and Ni(NO<sub>3</sub>)<sub>2</sub> in an acidic medium [47]. The XRD analysis showed that the product (NKMO) had a tetragonal crystal lattice corresponding to α-MnO<sub>2</sub>, in which 5% of the Mn was substituted by Ni. The Ni:Mn elemental ratio was defined as 0.055:1 from the ICP-OES results. The specific discharge capacity of the NKMO cathode at 0.05 C (where 1 C = 0.308 A·g<sup>-1</sup>) was 303 mAh·g<sup>-1</sup> in the mild mixed aqueous 2 M ZnSO<sub>4</sub>/0.2 M MnSO<sub>4</sub> electrolyte, which was 29% higher than that of the undoped MnO<sub>2</sub>-based cathode. Even at the high current density of 4 C, the specific capacity was 190 mAh·g<sup>-1</sup>, but the capacity retention over 2000 cycles was slightly lower (71%) than for MnO<sub>2</sub> (73%). Theoretical investigations by DFT calculations showed that the structural transformation from the tetragonal to the orthorhombic phase is more effective in the presence of Ni, leading to the enhancement of H<sup>+</sup> diffusion into the MnO<sub>2</sub> tunnels and, consequently, to a superior rate performance.

Copper, another rather popular dopant for various cathode materials, has also been used for MnO<sub>2</sub> modification [48,49]. To obtain Cu-doped MnO<sub>2</sub> (CuMO) materials, a hydrothermal synthesis from KMnO<sub>4</sub> and CuSO<sub>4</sub> solutions in the presence of citric acid was

used [49]. The crystal structure of the as-synthesized product was matched to the birnessite-type  $\delta$ - $\text{MnO}_2$ , and the morphology of this material was described as nanoflowers consisting of nanoflakes. The presence of Cu 2p peaks in the XPS spectra confirmed the intercalation of  $\text{Cu}^{2+}$  ions into the  $\text{MnO}_2$  lattice, and the valence state of the manganese was slightly reduced after the doping. The Cu:Mn ratio in the CuMO determined by the ICP-OES was 0.06:1. The specific capacity values of the CuMO obtained in 2 M  $\text{ZnSO}_4$ /0.1 M  $\text{MnSO}_4$  aqueous electrolyte at  $I = 0.1$  and  $2.0 \text{ A}\cdot\text{g}^{-1}$  were  $493.3$  and  $125.8 \text{ mAh}\cdot\text{g}^{-1}$ , respectively, which was much higher than those of unmodified  $\text{MnO}_2$ . This remarkable rate performance was related to the high conductivity of the Cu-doped material. The capacity retention for 150 cycles at  $I = 0.5 \text{ A}\cdot\text{g}^{-1}$  was close to 95%, with capacity growth during continuous cycling due to  $\text{MnO}_x$  electrodeposition from the electrolyte solution. Thus, CuMO undergoes a displacement mechanism in which  $\text{Cu}^{2+}$  is reduced to metallic form and extracted from the crystal lattice.

$\text{Cu}^{2+}$  pre-intercalated  $\delta$ - $\text{MnO}_2$  (CuMO) was also hydrothermally synthesized on the carbon cloth from the  $\text{KMnO}_4$  solution mixed with  $\text{CuCl}_2$  to fabricate a flexible binder-free electrode [48]. The morphology and microstructure of the as-prepared sample were described as nanowires which are homogeneously anchored on carbon fibers (Figure 7a). Based on the XRD patterns, the crystalline structure of CuMO was shown to be  $\delta$ - $\text{MnO}_2$ . XPS peaks of Cu 2p in the 935 eV binding energy region confirmed that Cu ions were intercalated into the  $\text{MnO}_2$  host structure. This led to an increase in the  $\text{Mn}^{3+}$  content in the CuMO material by creating active oxygen defects. The molar ratio of Cu:Mn was determined to be 0.1:1 by ICP-OES. The higher conductivity of the CuMO material was confirmed by DFT calculations of the bandgap, which was lower for the Cu-doped sample. The rate performance of the CuMO electrode was investigated in an aqueous solution of 2 M  $\text{ZnSO}_4$ /0.2 M  $\text{MnSO}_4$  in the current range of 0.1–5.0  $\text{A}\cdot\text{g}^{-1}$ . At a low current density of  $0.1 \text{ A}\cdot\text{g}^{-1}$ , the specific capacity value was  $398 \text{ mAh}\cdot\text{g}^{-1}$ , and at  $I = 5.0 \text{ A}\cdot\text{g}^{-1}$ , it was  $125 \text{ mAh}\cdot\text{g}^{-1}$ . As observed for another Cu-modified electrode [49], this remarkable rate performance was due to the high conductivity of the material. The cycling performance of the CuMO electrode was evaluated at current densities of 0.2 and  $5.0 \text{ A}\cdot\text{g}^{-1}$  over 90 and 700 cycles, respectively. At a low current density of  $0.2 \text{ A}\cdot\text{g}^{-1}$ , a slight increase in specific capacity up to  $280 \text{ mAh}\cdot\text{g}^{-1}$  was observed during 50 cycles, and then a decrease in capacity to  $240 \text{ mAh}\cdot\text{g}^{-1}$  occurred. As shown in the Figure 7b, at the high current density of  $5.0 \text{ A}\cdot\text{g}^{-1}$ , the capacity retention was 90.1% without significant capacity growth. Thus, rapid and reversible  $\text{Zn}^{2+}$  storage was achieved in a structurally modulated  $\delta$ - $\text{MnO}_2$  cathode with high conductivity of CuMO and stability of CuMO capacitive response during long-term cycling.

### 2.2.2. Heavy Transition Metal Ions

Silver ions were used as dopants for  $\text{MnO}_2$ -based cathodes to develop flexible quasi-solid-state AZIBs [50]. Ag-doped  $\text{MnO}_2$  was prepared hydrothermally from  $\text{MnSO}_4$  solution in the presence of  $(\text{NH}_4)_2\text{S}_2\text{O}_8$  and  $\text{AgNO}_3$  at different concentrations. The crystal structure of the as-synthesized product was determined to be  $\alpha$ - $\text{MnO}_2$  from the XRD patterns. After doping, increased lattice distortion was observed in the  $\text{MnO}_2$  cell. The valence state of manganese was slightly reduced after the incorporation of  $\text{Ag}^+$  ions, as was confirmed by XPS spectroscopy. The content of oxygen defects calculated from the O 1s XPS spectra was 23%, slightly higher than for pure  $\text{MnO}_2$  (19%). Electrochemical tests in an electrolyte solution of 2 M  $\text{ZnSO}_4$ /0.1 M  $\text{MnSO}_4$  showed that the Ag-doped material had a specific capacity value of  $315 \text{ mAh}\cdot\text{g}^{-1}$  at  $I = 0.05 \text{ A}\cdot\text{g}^{-1}$ , and at a high current density of  $2.0 \text{ A}\cdot\text{g}^{-1}$ , the retained capacity was only  $85 \text{ mAh}\cdot\text{g}^{-1}$ . The capacity retention during 500 cycles at  $I = 0.5 \text{ A}\cdot\text{g}^{-1}$  was 94%. During continuous cycling, a slight capacity increase was observed from the 50th to the 300th cycle, and then a gradual capacity decrease took place. According to the impedance spectroscopy data,  $\text{Ag}^+$  ions intercalated in the  $\text{MnO}_2$  host decreased the charge-transfer resistance and facilitated  $\text{Zn}^{2+}$  migration due to the expanded crystal lattice.

Molybdenum ions are high-valence particles that can form chemical bonds with oxygen atoms and stabilize the  $\text{Mn}^{3+}$  to improve the structural stability of  $\text{MnO}_2$  [51]. To prepare Mo-doped  $\text{MnO}_2$ ,  $\text{KMnO}_4$  solution was mixed with  $\text{Na}_2\text{MoO}_4$  solution, and then the resulting mixture was acidified and hydrothermally treated. As a result, a tunnel-type  $\alpha$ - $\text{MnO}_2$  lattice structure was obtained, and the morphology of the Mo- $\text{MnO}_2$  was described as nanorods with a diameter of 44 nm. The XPS data confirmed that manganese had two valence states,  $\text{Mn}^{3+}$  and  $\text{Mn}^{4+}$ , while for molybdenum,  $\text{Mo}^{5+}$  and  $\text{Mo}^{6+}$  valence states were observed. Electrochemical tests in a conventional zinc–manganese electrolyte in the potential range of 0.5–1.8 V showed that the initial capacity at  $I = 0.1 \text{ A}\cdot\text{g}^{-1}$  for the Mo- $\text{MnO}_2$  cathode was  $200 \text{ mAh}\cdot\text{g}^{-1}$ , while for  $\text{MnO}_2$ , it was  $250 \text{ mAh}\cdot\text{g}^{-1}$ , but at a high current density ( $5 \text{ A}\cdot\text{g}^{-1}$ ) and during 100 cycles, the specific capacity of Mo- $\text{MnO}_2$  was higher than that of the unmodified  $\text{MnO}_2$  cathode. The better rate capability of Mo- $\text{MnO}_2$  was clearly observed at current densities higher than  $0.5 \text{ A}\cdot\text{g}^{-1}$  (Figure 7c). The capacity retention of Mo- $\text{MnO}_2$  at  $I = 2.0 \text{ A}\cdot\text{g}^{-1}$  was 82.6%, while for  $\text{MnO}_2$ , only 22% of the capacity was retained. It was also observed that the valence state of Mo changes during cycling, and the partial substitution of  $\text{Mn}^{3+}$  by  $\text{Mo}^{5+}$  decreased the rate of the disproportionation process, resulting in the improved cycling stability of the Mo-doped material.

The hydrothermal method was also used to obtain Mo-doped  $\text{MnO}_2$  with a birnessite-type structure by the reaction between  $\text{KMnO}_4$  and  $\text{MnSO}_4$  in the presence of  $(\text{NH}_4)_6\text{Mo}_7\text{O}_{24}$  [52]. The morphology of the as-obtained product was typical of layered manganese oxide and was described as irregular microparticles consisting of interconnected nanosheets. The crystal structure of  $\delta$ - $\text{MnO}_2$  was confirmed by XRD, and the expansion of the interlayer spacing from 0.631 to 0.674 nm due to Mo intercalation was observed by XRD and TEM analyses. The valence states of  $\text{Mo}^{4+}$  and  $\text{Mn}^{3+}/\text{Mn}^{4+}$  and the higher concentration of oxygen defects were determined by XPS. The Mo-doped  $\text{MnO}_2$  cathode in a conventional 2 M  $\text{ZnSO}_4/0.1 \text{ M MnSO}_4$  electrolyte showed capacity growth at a current density of  $0.1 \text{ A}\cdot\text{g}^{-1}$  up to  $327 \text{ mAh}\cdot\text{g}^{-1}$ , while at the high current density of  $3.0 \text{ A}\cdot\text{g}^{-1}$ , the specific capacities of  $\text{MnO}_2$  and Mo- $\text{MnO}_2$  were almost equal ( $107 \text{ mAh}\cdot\text{g}^{-1}$ ). Moreover, the stability of the Mo-doped material was the same as that of the undoped material (Figure 7d), while the specific capacity of the Mo- $\text{MnO}_2$  cathode after 1000 cycles at  $1.0 \text{ A}\cdot\text{g}^{-1}$  was 57% higher. Mo ions serve as “pillars” for layered structures which stabilize the crystal lattice by forming Mo–O bonds. In addition, oxygen defects provide more sites for  $\text{Zn}^{2+}/\text{H}^+$  intercalation, which explains the superior performance of Mo- $\text{MnO}_2$  in the current range of  $0.2$ – $2.0 \text{ A}\cdot\text{g}^{-1}$ .

Thus, the transition metal ions could facilitate the diffusion of  $\text{Zn}^{2+}$  ions due to their large size or interactions between the metal ion and  $\text{MnO}_2$  host; however, not all metal ions, such as Ni, Mo, and some others, could be effective dopants for  $\text{MnO}_2$ , while Zn, Fe, Co, and Cu ions are rather good for improving the electrochemical properties of cathode materials, especially for binder-free cathodes.

### 2.2.3. Rare-Earth-Metal Ions

Rare earth metals have also been successfully intercalated into the  $\text{MnO}_2$ -based cathodes. Lanthanum-doped  $\text{MnO}_2$  was obtained by a simple precipitation method from mixed solutions of  $\text{MnSO}_4$  and  $\text{KMnO}_4$  with the addition of  $\text{La}(\text{NO}_3)_3$  [53]. XRD and SEM analyses of La-doped  $\text{MnO}_2$  (LMO) showed that the oxide had a flower-like morphology that is typical of layered-type materials, and the XRD patterns confirmed that birnessite-type  $\delta$ - $\text{MnO}_2$  was obtained. The interlayer distance in LMO observed from the TEM and XRD data was 0.76 nm, while for undoped  $\text{MnO}_2$ , it was 0.68 nm, indicating the expansion of the interlayer space due to La intercalation. The Mn:O element ratio determined from the XPS data was 0.97:2, so the main valence state of manganese was  $\text{Mn}^{4+}$ . The LMO cathode in 1 M  $\text{ZnSO}_4/0.4 \text{ M MnSO}_4$  electrolyte reached a high specific capacity of  $275 \text{ mAh}\cdot\text{g}^{-1}$  at  $I = 0.1 \text{ A}\cdot\text{g}^{-1}$ , and after increasing the current to  $1.6 \text{ A}\cdot\text{g}^{-1}$ , the specific capacity was  $121.8 \text{ mAh}\cdot\text{g}^{-1}$ , which is much better than the almost-zero capacity of the unmodified  $\text{MnO}_2$  cathode. The probable explanation for this remarkable rate performance is that the

pre-intercalated pillars of  $\text{La}^{3+}$  promoted  $\text{Zn}^{2+}$  diffusion due to the expanded interplanar spaces. The capacity retention of the LMO cathode after 200 cycles at  $0.2 \text{ A}\cdot\text{g}^{-1}$  was 71%, which is associated with the high reversibility of the cathodic reaction in the presence of  $\text{La}^{3+}$  ions.

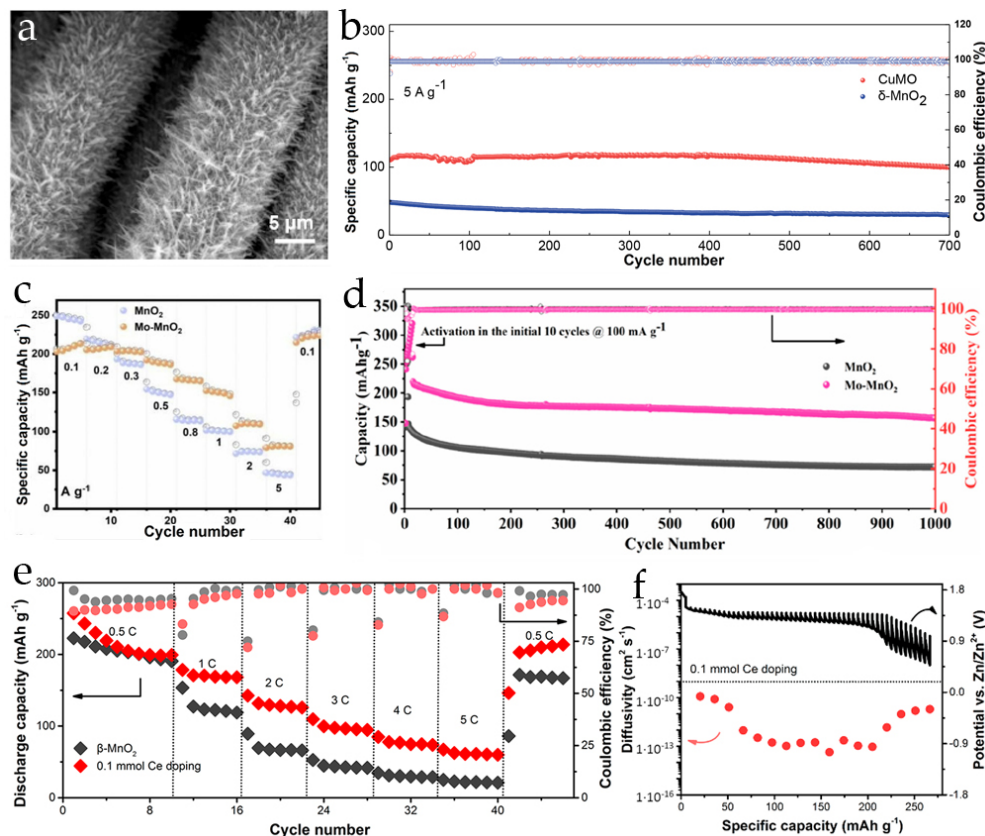


**Figure 7.** (a) SEM image of CuMO [48]. (b) Cycling performance of  $\text{MnO}_2$  and CuMO electrodes at  $5 \text{ A}\cdot\text{g}^{-1}$  [48]. (c) Rate performance of  $\text{MnO}_2$  and Mo- $\text{MnO}_2$  cathodes [51]. (d) Cycling performance of  $\text{MnO}_2$  and Mo- $\text{MnO}_2$  cathodes [52]. (e) Rate capability of Ce-doped  $\text{MnO}_2$  [54]. (f) GITT curve and diffusivity vs. state of discharge for Ce-doped  $\text{MnO}_2$  [54].

As lanthanum, cerium ions have been used to modify  $\text{MnO}_2$ -based cathode materials [54,55]. Chemically synthesized Ce-doped  $\text{MnO}_2$  was obtained hydrothermally from  $\text{MnSO}_4$  solution in the presence of cerium (III) nitrate additive, and  $(\text{NH}_4)_2\text{S}_2\text{O}_8$  was used as the oxidant [54]. The diffraction peaks on the XRD patterns of the Ce-doped product corresponded to tunnel-type  $\alpha\text{-MnO}_2$ , while  $\text{MnO}_2$  obtained in the same conditions without Ce additive corresponded to  $\beta\text{-MnO}_2$ . Thus, cerium ions enlarged  $1 \times 1$  tunnels of  $\beta\text{-MnO}_2$  to  $2 \times 2$  tunnels, corresponding to  $\alpha\text{-MnO}_2$ . The valence states of manganese and cerium evaluated by XPS were +3.75 and +3, respectively. The morphology of Ce-doped  $\text{MnO}_2$  was uniform nanorods, the length of which decreased with increasing amount of cerium. The specific capacity of Ce-doped  $\text{MnO}_2$  in aqueous  $2 \text{ M ZnSO}_4/0.1 \text{ M MnSO}_4$  electrolyte was higher than that of undoped  $\beta\text{-MnO}_2$  in the current range of 1–5 C ( $1 \text{ C} = 0.308 \text{ A}\cdot\text{g}^{-1}$ ) (Figure 7e). At  $I = 1 \text{ C}$ , the specific capacity of Ce-doped  $\text{MnO}_2$  was  $160 \text{ mAh}\cdot\text{g}^{-1}$ , and at  $5 \text{ C}$ , the capacity was  $134 \text{ mAh}\cdot\text{g}^{-1}$ . The cyclic stability over 100 cycles at  $2 \text{ C}$  was higher for Ce-doped  $\text{MnO}_2$  than for  $\beta\text{-MnO}_2$ : the capacity retention was 80% and 50%, respectively. The galvanostatic intermittent titration technique (GITT) test showed that the chemical diffusion coefficient of  $\text{Zn}^{2+}$  in Ce-doped  $\text{MnO}_2$  is significantly increased; it was determined to be  $10^{-10}\text{--}10^{-13} \text{ cm}^2 \text{ s}^{-1}$  during the entire Zn intercalation process (Figure 7f), which is 10–100 times higher than that of the pristine  $\beta\text{-MnO}_2$  cathode. The result clearly

showed that the  $2 \times 2$  tunnel structure of Ce-doped  $\text{MnO}_2$  facilitated fast and reversible  $\text{Zn}^{2+}$  migration, resulting in better rate capability.

Ce-doped  $\text{MnO}_2$  was potentiostatically deposited at  $E = 1.2\text{--}1.7$  V (vs.  $\text{Ag}/\text{AgCl}$ ) on the carbon cloth from the  $\text{MnSO}_4$  solution in the presence of surfactants and cerium nitrate to obtain a binder-free cathode [55]. The resulting Ce- $\text{MnO}_2$ @CC composite showed a uniform coating with a porous lamellar structure on the substrate surface. The XRD patterns showed that the resulting Ce- $\text{MnO}_2$  material was amorphous, which was confirmed by field-emission SEM. XPS spectroscopy was used to confirm the Ce doping of the  $\text{MnO}_2$  structure and to determine the  $\text{Mn}^{4+}$  valence state. The specific capacity of the Ce- $\text{MnO}_2$ @CC electrode in the mixed zinc–manganese sulfate electrolyte was  $292 \text{ mAh}\cdot\text{g}^{-1}$  at  $0.1 \text{ A}\cdot\text{g}^{-1}$ , while only  $179 \text{ mAh}\cdot\text{g}^{-1}$  was achieved for the undoped material. Even at a high current density of  $2 \text{ A}\cdot\text{g}^{-1}$ , the Ce-doped cathode material still maintained a considerable capacity of  $106 \text{ mAh}\cdot\text{g}^{-1}$ . During 450 cycles at  $I = 0.1 \text{ A}\cdot\text{g}^{-1}$ , a sharp capacity decay was observed during the first 40 cycles, and then almost-stable capacities were observed with an insignificant increase from 190 to  $200 \text{ mAh}\cdot\text{g}^{-1}$ . It was found that cerium ions, together with a highly conductive carbon substrate, accelerate the ionic transport through the cathode material, resulting in a superior rate performance.

Thus, rare-earth-metal ions can be used as dopants for  $\text{MnO}_2$ -based cathodes. However, large ionic radii of  $\text{La}^{3+}$ ,  $\text{Ce}^{3+}$ , and their analogues resulted in insufficient cycling stability (more than 20% of capacity decay after 100–200 cycles), which is lower than the values for  $\text{MnO}_2$ -based cathodes doped with transition metal cations with smaller ionic radii.

### 2.3. Post-Transition Metal Ions

Aluminum is one of the most attractive non-alkali and non-transition metals because  $\text{Al}^{3+}$  ions can combine with the O atom to form a stable Al–O chemical bond. Al-doped  $\text{MnO}_2$  has been successfully used as a cathode material for AZIBs [24,56,57]. Al-doped  $\text{MnO}_2$  with different crystal phases and morphologies was obtained hydrothermally from the solutions of  $\text{KMnO}_4$  in the presence of  $\text{Al}(\text{NO}_3)_3$  [24,57] or  $\text{Al}_2(\text{SO}_4)_3$  [56].

Al-doped  $\text{MnO}_2$  (AMO) with an urchin-like morphology consisting of numerous nanorods was obtained by self-reduction of  $\text{KMnO}_4$  in the presence of aluminum nitrate [24]. The XRD analysis showed that tetragonal  $\alpha$ - $\text{MnO}_2$  was synthesized, and the observed shift of the most intensive peak to lower  $2\theta$  angles (Figure 8a) suggested the change of the space parameter of the crystal lattice due to heteroatom intercalation. Based on a high-resolution TEM analysis, the interplanar distance was close to 0.29 nm, compared to 0.24 nm for undoped material. A decrease in the valence state of manganese to  $\text{Mn}^{3+}$  was also observed, resulting in a change of the length of the Mn–O bond. The initial specific capacity of the AMO cathode material in 2 M  $\text{ZnSO}_4$  without the  $\text{Mn}^{2+}$  additive was  $401 \text{ mAh}\cdot\text{g}^{-1}$  at a current density of  $0.1 \text{ A}\cdot\text{g}^{-1}$ , and at high  $I = 4.0 \text{ A}\cdot\text{g}^{-1}$ , the capacity was  $229 \text{ mAh}\cdot\text{g}^{-1}$ , much higher than that of pristine  $\text{MnO}_2$  (Figure 8b). This remarkable capacity performance at high currents may be due to the decrease of polarization in the AMO which was observed from the cyclic voltammetry data (Figure 8c). During continuous cycling (over 2000 cycles at a current density of  $2.0 \text{ A}\cdot\text{g}^{-1}$ ) in the absence of  $\text{MnSO}_4$  additive in the electrolyte solution, the capacity retention was 94.5%. The concentrations of dissolved manganese at different stages of cell life, as determined by the ICP analysis of AMO electrodes, were extremely low ( $<0.3 \text{ mg}\cdot\text{L}^{-1}$ ), and the  $\text{Al}^{3+}$  concentration was also low ( $\approx 0.6 \text{ mg}\cdot\text{L}^{-1}$ ). Thus, highly stable Al–O chemical bonds not only increase the interplanar distances but also stabilize the interactions within the crystal lattice, preventing  $\text{MnO}_2$  dissolution.

To stabilize the metal ions in the  $\text{MnO}_2$  structure, coatings that interact with the intercalated metal ions can be used. In the case of  $\text{Al}^{3+}$ , lignin was used as such a coating to obtain lignin-coated Al-doped  $\text{MnO}_2$  (L+Al@ $\text{MnO}_2$ ) [56]. During the synthesis, one-dimensional nanorods with the crystal structure of  $\alpha$ - $\text{MnO}_2$  were obtained. According to the EDX mapping of the main elements (Mn, O, Al, and C), the lignin coating was uniformly distributed on the Al@ $\text{MnO}_2$  surface. The Al:Mn atomic ratio was close to 1:22 according



to ICP-OES. A partial reduction of  $\text{Mn}^{4+}$  during the doping process was observed from the XPS spectra of manganese, suggesting that some of the  $\text{Mn}^{4+}$  ions were exchanged with  $\text{Al}^{3+}$  ions without significant changes in valence state with the introduction of the oxygen defects. Electrochemical tests in 2 M  $\text{ZnSO}_4/0.2$  M  $\text{MnSO}_4$  showed that the doping of  $\text{MnO}_2$  with  $\text{Al}^{3+}$  ions improved the diffusion of  $\text{H}^+$ , increasing the specific capacities up to  $188 \text{ mAh}\cdot\text{g}^{-1}$ , and the lignin coating stabilized the material structure during cycling and prevented the dissolution of manganese, leading to an increase in the cycling stability (66.7% of capacity retention after 3000 cycles at a current density of  $1.5 \text{ A}\cdot\text{g}^{-1}$ ).

$\text{Al}^{3+}$  ions have also been used as dopants for birnessite-type  $\text{MnO}_2$  with pre-intercalated  $\text{K}^+$  ions in the interlayer spaces (KMO) [57]. Hydrothermally obtained Al-doped  $\text{MnO}_2$  with  $\text{K}^+$  ions (Al-KMO) with a layered structure had a smaller grain size (6.7 nm instead of 8.4 nm), and the pre-intercalation of  $\text{Al}^{3+}$  improved the nucleation rate of the grains, resulting in a large specific surface area ( $44.1 \text{ m}^2\cdot\text{g}^{-1}$ ). Al-KMO had a microflower morphology composed of nanosheets. Compared with the KMO material, the particles of the Al-doped material were more spherical due to the prevention of the agglomeration by stabilizing the internal structure. The XPS analysis showed that  $\text{Al}^{3+}$  and  $\text{K}^+$  were both intercalated in the  $\text{MnO}_2$  structure, and  $\text{Al}^{3+}$  ions exchanged both  $\text{K}^+$  and  $\text{Mn}^{4+}$  ions. This reduced the electrostatic repulsions between intercalated  $\text{Zn}^{2+}$  ions and the  $\text{MnO}_2$  host lattice. The specific capacity of Al-KMO in a zinc–manganese mixed aqueous electrolyte at a low current density of  $0.1 \text{ A}\cdot\text{g}^{-1}$  was  $327 \text{ mAh}\cdot\text{g}^{-1}$ , and at  $I = 2.0 \text{ A}\cdot\text{g}^{-1}$ , it was  $85 \text{ mAh}\cdot\text{g}^{-1}$ , higher than the capacities of as-prepared KMO and the samples calcined at  $300^\circ\text{C}$  (KMO-300 and Al-KMO-300) (Figure 8d). After 300 cycles at  $I = 0.5 \text{ A}\cdot\text{g}^{-1}$ , the retained capacity of Al-KMO was  $205 \text{ mAh}\cdot\text{g}^{-1}$ , corresponding to 90% of the capacity retention. However, the Al-KMO had the longest activation process (Figure 8e). In conclusion, the intercalation of  $\text{Al}^{3+}$  and co-intercalation of water molecules stabilized the interlayer spaces, thus enhancing the diffusion of  $\text{Zn}^{2+}$  and  $\text{H}^+$  ions and reducing the dissolution of manganese. It was also shown that calcined samples without intercalated water molecules had a lower electrochemical performance than Al-KMO before calcination.

The one-step pre-intercalation of  $\text{K}^+$ ,  $\text{Co}^{2+}$ , and  $\text{Al}^{3+}$  ions was used to enhance the diffusion  $\text{Zn}^{2+}$  ions and the conductivity of  $\text{MnO}_2$ -based electrode materials [58]. This tri-ion-doped electrode material ( $\alpha\text{-MnO}_2@\text{KCoAl}$ ) was synthesized by a one-step precipitation method, without heating. The crystal structure of the as-synthesized product determined by XRD corresponded to tetragonal  $\alpha\text{-MnO}_2$ . The morphology of the doped sample was described as irregular lumpy small particles with high dispersity and a specific surface area of  $\approx 6 \text{ m}^2\cdot\text{g}^{-1}$ . After doping, the valence state of  $\text{Mn}^{4+}$  was partially decreased, confirming the intercalation of all heterovalent atoms. The specific capacity of  $\alpha\text{-MnO}_2@\text{KCoAl}$  in the 2 M  $\text{ZnSO}_4/0.05$  M  $\text{MnSO}_4$  electrolyte at a current density of  $0.5 \text{ A}\cdot\text{g}^{-1}$  was  $524 \text{ mAh}\cdot\text{g}^{-1}$ , which is an extremely high value. Even at the high current density of  $5.0 \text{ A}\cdot\text{g}^{-1}$ , the specific capacity delivered was  $221 \text{ mAh}\cdot\text{g}^{-1}$ . This outstanding rate performance of  $\alpha\text{-MnO}_2@\text{KCoAl}$  can be explained by the significant decrease of the internal resistance in the ternary-doped composite. Nevertheless, the capacity retention of  $\alpha\text{-MnO}_2@\text{KCoAl}$  at  $0.5 \text{ A}\cdot\text{g}^{-1}$  was 66% over 100 cycles, and at  $I = 5.0 \text{ A}\cdot\text{g}^{-1}$ , it was only 34% over 800 cycles, which is comparable to the unmodified  $\text{MnO}_2$  cathode. Despite the high conductivity achieved, the problem of manganese dissolution was not solved by tri-ion doping.

Another trivalent ion with a high ionic radius that has been successfully used for  $\text{MnO}_2$  modification is the bismuth ion  $\text{Bi}^{3+}$  [49,59]. A hydrothermal synthesis of Bi-doped  $\text{MnO}_2$  (BiMO) was carried out from  $\text{KMnO}_4$  and  $\text{Bi}(\text{NO}_3)_3$  solutions in the presence of citric acid [49]. The layered  $\text{MnO}_2$  structure was confirmed by XRD, and the patterns of the BiMO were of lower intensity compared to the pristine  $\text{MnO}_2$ . The morphology of the BiMO particles was nanoflowers consisting of interconnected nanoflakes, with uniform distribution of Mn, O, and Bi, as was shown by the EDX analysis. The pre-intercalation of  $\text{Bi}^{3+}$  was confirmed by the appearance of Bi 4f peaks in the XPS spectra. The Bi:Mn ratio determined by ICP-OES was 0.09:1. Despite the presence of a dopant, the specific capacity

of the BiMO cathode in the 2 M ZnSO<sub>4</sub>/0.1 M MnSO<sub>4</sub> electrolyte at low current densities (0.1–0.4 A·g<sup>-1</sup>) was lower than that of unmodified MnO<sub>2</sub> (175.5 and 273.4 mAh·g<sup>-1</sup> at I = 0.1 A·g<sup>-1</sup>, respectively). Nevertheless, the cyclic stability of the BiMO material at I = 0.5 and 1.0 A·g<sup>-1</sup> was high. The capacity retention over 500 cycles at 0.5 A·g<sup>-1</sup> was 72.3%, and at I = 1.0 A·g<sup>-1</sup>, it was 98.6% over 1100 cycles. In addition, at the high current density of 2.0 A·g<sup>-1</sup>, the specific capacity of BiMO was 66 mAh·g<sup>-1</sup>. Thus, doping with bismuth ions affected the structural stability of the MnO<sub>2</sub> crystal lattice and prevented the dissolution of manganese, but the conductivity of this composite was relatively low.

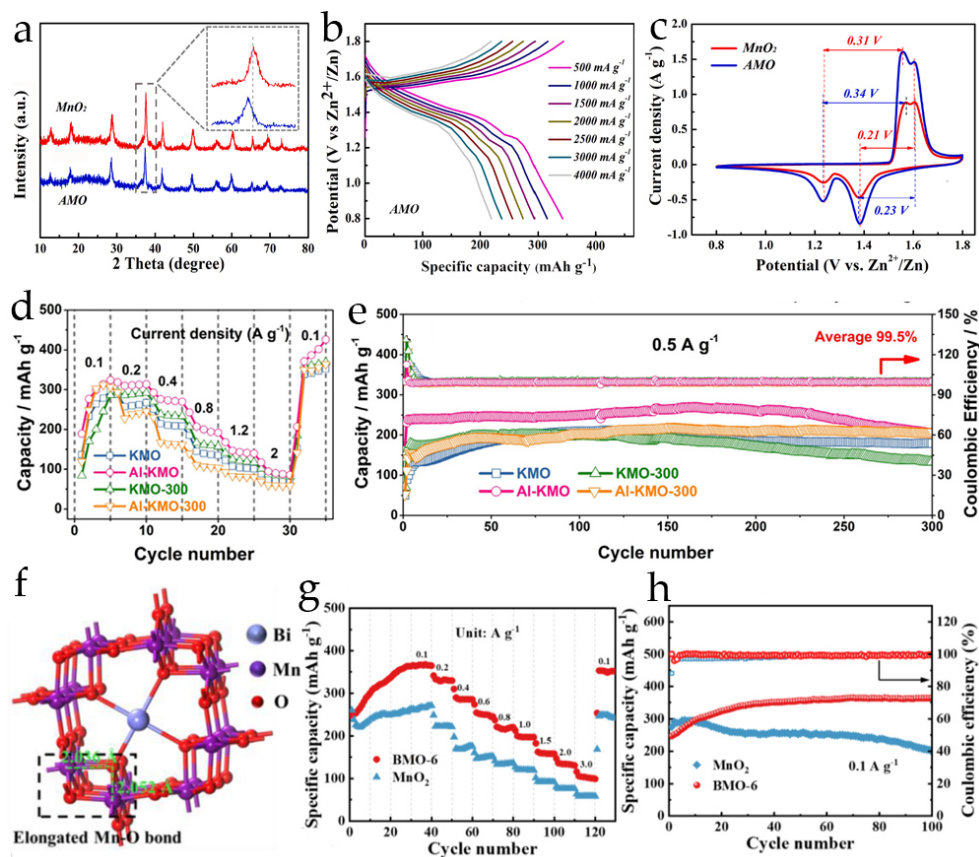


**Figure 8.** (a) XRD patterns of MnO<sub>2</sub> and AMO [24]; (b) GCD profiles of AMO cathode under different current densities [24]. (c) Cyclic voltammograms of MnO<sub>2</sub> and AMO cathodes at scan rate 0.2 mV·s<sup>-1</sup> [24]. (d) Rate performance of KMO, Al-KMO, KMO-300 and Al-KMO-300 [57]. (e) Cycling performance of KMO and Al-KMO materials [57]. (f) Schematic relaxed structure of Bi-doped MnO<sub>2</sub> [59]. (g) C-rate capability and (h) long-term cycle performance of pristine and Bi-doped MnO<sub>2</sub> cathodes [59].

Bi-doped MnO<sub>2</sub> (BMO) was also prepared via precipitation from KMnO<sub>4</sub> and Bi(NO<sub>3</sub>)<sub>3</sub> solutions with further annealing [59]. After synthesis, nanoparticles with an average size of 50 nm and uniform distribution of Mn, Bi, and O elements were obtained. The crystal lattice of BMO corresponded to  $\alpha$ -MnO<sub>2</sub>. The valence state of manganese defined from the XPS spectra was Mn<sup>4+</sup> with small amounts of Mn<sup>3+</sup>, so the intercalation of Bi affected the electronic structure of MnO<sub>2</sub>. First-principles calculations were also used to determine the changes in the crystal lattice after doping. It was shown (Figure 8f) that the presence of Bi<sup>3+</sup> ions increased the Mn–O bond, causing the expansion of the inner spaces. The electrochemical tests in 2 M ZnSO<sub>4</sub>/0.2 M MnSO<sub>4</sub> aqueous electrolyte showed that BMO had a higher rate capability than undoped MnO<sub>2</sub> (Figure 8g), and the specific capacity of BMO at low current density (0.1 A·g<sup>-1</sup>) increased continuously due to MnO<sub>x</sub> deposition and reached 365 mAh·g<sup>-1</sup>, while the specific capacity of pristine MnO<sub>2</sub> gradually decreased to 200 mAh·g<sup>-1</sup> (Figure 8h). After increasing the current to 3.0 A·g<sup>-1</sup>, the delivered capacity

was 103 mAh·g<sup>-1</sup>, which is a relatively high value. The capacity retention of the BMO electrodes over 10,000 cycles at I = 1.0 A·g<sup>-1</sup> was 93%, indicating that the bismuth ions, which were incorporated into the MnO<sub>2</sub> crystal lattice, had a greater effect on the structural stability than on the conductivity of the material.

As shown by the example of Sn doping, MnO<sub>2</sub> can also be doped with the tetravalent ions [30]. Manganese dioxide was synthesized by the hydrothermal method from a mixed solution of KMnO<sub>4</sub> and MnSO<sub>4</sub> in the presence of an acidic SnCl<sub>2</sub> solution, and then the product was calcined. The crystal lattice of the obtained product ( $\alpha$ -SM) was defined as the tunnel-type  $\alpha$ -MnO<sub>2</sub> without the presence of tin oxide. The material had a rod-like morphology with a tendency to agglomerate. Tin doping was additionally confirmed by the presence of Sn 3d<sub>3/2</sub> and 3d<sub>5/2</sub> peaks in the XPS spectra. The valence states of manganese and tin determined by XPS were +4, +3, and +2 for Mn and +4 for Sn. Thus, during the synthesis, Sn<sup>2+</sup> was oxidized by potassium permanganate with intercalation of the resulting Sn<sup>+4</sup> into the lattice of MnO<sub>2</sub>, with the formation of oxygen defects. The cyclic performance of  $\alpha$ -SM was studied in the current range of 0.1–2.0 A·g<sup>-1</sup>. The specific capacities obtained were 240 mAh·g<sup>-1</sup> (0.1 A·g<sup>-1</sup>) and 45 mAh·g<sup>-1</sup> (2.0 A·g<sup>-1</sup>), with the initial capacity growth during 20 cycles at 0.1 A·g<sup>-1</sup> and subsequent sharp capacity fading. During continuous cycling at I = 0.1 A·g<sup>-1</sup>, the specific capacity increased from 250 to 339 mAh·g<sup>-1</sup> in 34 cycles, and then it decreased to 160 mAh·g<sup>-1</sup> over 70 cycles. Increasing the current density to 1.0 A·g<sup>-1</sup> resulted in a decrease in capacity, but the increase in stability at the high current density (the capacity retention over 500 cycles was 80%) was explained by the rapid dissolution of manganese at low current densities and the inhibition of this process at the high discharge rates.

Trivalent and tetravalent ions intercalated into the MnO<sub>2</sub> crystal lattice have a crucial effect on the stability of the crystal lattice and oxygen defects. Large Sn<sup>+4</sup> ions significantly improved the conductivity, but they also destabilized the lattice of MnO<sub>2</sub> and promoted the Mn<sup>2+</sup> dissolution. On the other hand, trivalent ions have strong chemical bonding with oxygen atoms, and this stabilizes the structure and, in the case of Al<sup>3+</sup>, improves the conductivity, so Al-doped MnO<sub>2</sub> materials are the most attractive for further development.

The above reviewed results on the electrochemical properties of the metal-doped MnO<sub>2</sub>-based cathode materials are summarized in Table 1. The observed effects are related to the improved stability of the materials and the enhanced reversibility of the intercalation processes due to the increased interlayer/channel spacing, which favors ionic diffusion. The stabilizing effect of the introduction of metal ions (probably combined with H<sub>2</sub>O molecules) into the host structure of MnO<sub>2</sub> adjusts the crystal spacing for easier insertion/extraction of H<sup>+</sup> and Zn<sup>2+</sup> ions.

**Table 1.** Electrochemical performance of selected MnO<sub>2</sub>-based materials doped with metal ions as cathodes in AZIBs.

Material	Synthesis Method	Morphology	Electrolyte	Specific Capacity, mAh g <sup>-1</sup> (Current Density, A·g <sup>-1</sup> )	Capacity Retention, (Number of Cycles and Current, A·g <sup>-1</sup> )	Ref.
K- $\delta$ -MnO <sub>2</sub>	precipitation	two-dimensional nanosheets	2 M ZnSO <sub>4</sub> + 0.1 M MnSO <sub>4</sub>	270.5 (0.1); 220.1 (1); 95.1 (3)	104.6% (100, 0.3)	[23]
Li <sub>0.023</sub> Mn <sub>0.87</sub> O <sub>2</sub>	two-stage hydrothermal method (140/110 °C)	nanorods	2 M ZnSO <sub>4</sub> + 0.1 M MnSO <sub>4</sub>	184 (0.1); 0.54 (2)	89% (1000, 1) 100% (100, 0.1)	[32]
Na- $\delta$ -MnO <sub>2</sub>	redox reaction	nanoplates	2 M ZnSO <sub>4</sub> + 0.2 M MnSO <sub>4</sub>	278 (0.308) 161 (1.85) 103 (6.16)	~100% (2000, 2.46/3.08)	[60]
Na:MnO <sub>2</sub> /GCF	electrochemical deposition on graphene-like carbon foam	nanosheets	2 M ZnSO <sub>4</sub> + 0.1 M MnSO <sub>4</sub>	381.8 (0.1) 258.5 (1) 94.8 (3)	~80% (100, 0.1) ~75% (1000, 1)	[33]

Table 1. Cont.

Material	Synthesis Method	Morphology	Electrolyte	Specific Capacity, mAh g <sup>-1</sup> (Current Density, A·g <sup>-1</sup> )	Capacity Retention, (Number of Cycles and Current, A·g <sup>-1</sup> )	Ref.
K <sub>0.19</sub> MnO <sub>2</sub> ·0.56H <sub>2</sub> O	one-pot hydrothermal method (180 °C)	nanosheets	3 M Zn(CF <sub>3</sub> SO <sub>3</sub> ) <sub>2</sub>	107 (1)	87.5% (2000, 10)	[28]
K-δ-MnO <sub>2</sub> -V	one-pot hydrothermal method (160 °C)	layered structure	2 M ZnSO <sub>4</sub> + 0.1 M MnSO <sub>4</sub> + 0.1 M K <sub>2</sub> SO <sub>4</sub>	288.8 (0.1) 85.7 (1)	91.9% (1500, 1) 89.4% (500, 0.6)	[35]
K <sub>0.29</sub> MnO <sub>2</sub> ·0.67H <sub>2</sub> O	one-pot hydrothermal method (180 °C)	nanosheets	2.5 M ZnSO <sub>4</sub> + 0.2 M MnSO <sub>4</sub>	300 (0.2) 219 (1) 136 (3)	92% (500, 0.2)	[36]
α-K <sub>0.19</sub> MnO <sub>2</sub>	self-sacrificial template method	nanotubes	3 M Zn(CF <sub>3</sub> SO <sub>3</sub> ) <sub>2</sub> + 0.2 M Mn(CF <sub>3</sub> SO <sub>3</sub> ) <sub>2</sub> + 3 M K(CF <sub>3</sub> SO <sub>3</sub> )	270 (0.308) 222.8 (0.616) 200 (1.54)	98.5% (50, 0.308) 92% (200, 0.616) 90% (400, 1.54)	[37]
LGP@K <sub>0.15</sub> MnO <sub>2</sub>	in-situ hydrothermal synthesis (150 °C)	nanosheets	2 M ZnSO <sub>4</sub> + 0.1 M MnSO <sub>4</sub>	402.6 (0.05) 196.1 (0.8) 116.1 (2)	92.5% (100, 0.2) 83.3% (1000, 1)	[38]
KMO-CNT/graphene	polyol reduction method	nanowires	2 M ZnSO <sub>4</sub> + 0.4 M MnSO <sub>4</sub>	373.1 (0.1) 213.6 (1) 108.8 (3)	82.5% (350, 0.5) 77% (1000, 3)	[39]
Ca <sub>0.28</sub> MnO <sub>2</sub> ·0.5H <sub>2</sub> O	one-step hydrothermal method	interconnected nanoflakes	1 M ZnSO <sub>4</sub> + 0.1 M MnSO <sub>4</sub>	298 (0.175) 277.7 (0.35) 124.5 (3.5)	85% (1000, 4) 92% (5000, 3.5)	[40]
Zn-δ-MnO <sub>2</sub>	redox reaction	flower-like nanospheres	2 M ZnSO <sub>4</sub> + 0.1 M MnSO <sub>4</sub>	275 (0.3) 121 (3)	100% (100, 0.3/0.6) 100% (500, 1)	[41]
GQDs·Zn <sub>x</sub> MnO <sub>2</sub>	redox reaction	nanoflowers	1 M ZnSO <sub>4</sub>	403.6 (0.3) 211.5 (4)	88.1% (500, 1)	[42]
Zn-doped Mn <sub>3</sub> O <sub>4</sub> -MnO <sub>2</sub> -NSs	electrochemical deposition	vertical nanosheets	2 M ZnSO <sub>4</sub> + 0.1 M MnSO <sub>4</sub>	562.1 (0.3) 272.7 (6)	69.4% (200, 3)	[27]
V-doped δ-MnO <sub>2</sub>	redox reaction	nanoparticles	1 M ZnSO <sub>4</sub>	266 (0.066) 150 (0.266) 67 (1.064)	52.4% (100, 0.066)	[25]
V-doped δ-MnO <sub>2</sub>	modified coprecipitation	nanosheets with aerogel-like morphology	2 M ZnSO <sub>4</sub>	194 (0.2) 74 (2)	71% (100, 0.3) 52% (600, 3)	[43]
Fe-doped δ-MnO <sub>2</sub>	one-step hydrothermal process (120 °C)	nanoflowers	2 M ZnSO <sub>4</sub> + 0.1 M MnSO <sub>4</sub>	390 (0.1) 320 (1) 160 (3)	86.3% (200, 1)	[44]
Co/Zn-doped δ-MnO <sub>2</sub> on N-doped CC	electrochemical deposition	film on the carbon nanowires	2 M ZnSO <sub>4</sub> + 0.07 M MnSO <sub>4</sub>	280 (1.2) 30 (10.5)	~100% (600, 1.2)	[26]
Co-doped δ-MnO <sub>2</sub>	molten-salt synthesis process	nanosheets	2 M ZnSO <sub>4</sub> + 0.2 M MnSO <sub>4</sub>	500 (0.1) 125 (5)	63% (5000, 2) 100% (0.3, 100)	[45]
Co-doped α-MnO <sub>2</sub> on CC	one-step hydrothermal process (120 °C) + plasma treatment	nanowires	2 M ZnSO <sub>4</sub> + 0.1 M MnSO <sub>4</sub>	511 (0.5) 337 (1) 100 (5)	98% (1000, 3)	[29]
Co-doped σ-MnO <sub>2</sub>	one-step electrodeposition	nanosheets	2 M ZnSO <sub>4</sub> + 0.2 M MnSO <sub>4</sub> + 0.02 CoAc	313.8 (0.5)	91.8% (1000, 1)	[46]
Ni-doped α-MnO <sub>2</sub> (Ni <sub>0.052</sub> K <sub>0.119</sub> Mn <sub>0.948</sub> O <sub>2</sub> ·0.208H <sub>2</sub> O)	one-step hydrothermal process (120 °C)	nanorods	3 M ZnSO <sub>4</sub> + 0.2 M MnSO <sub>4</sub>	303 (0.015)	71.4% (2000, 1.232)	[47]
Cu-doped δ-MnO <sub>2</sub> on CC	one-step hydrothermal process (160 °C)	nanowires	2 M ZnSO <sub>4</sub> + 0.2 M MnSO <sub>4</sub>	398.2 (0.1) 224.9 (1) 124.9 (5)	90.1% (700, 5)	[48]

Table 1. Cont.

Material	Synthesis Method	Morphology	Electrolyte	Specific Capacity, mAh g <sup>-1</sup> (Current Density, A·g <sup>-1</sup> )	Capacity Retention, (Number of Cycles and Current, A·g <sup>-1</sup> )	Ref.
Cu <sub>0.06</sub> MnO <sub>2</sub> ·1.7H <sub>2</sub> O (δ-MnO <sub>2</sub> )	one-step hydrothermal process (180 °C)	nanoflowers	2 M ZnSO <sub>4</sub> + 0.1 M MnSO <sub>4</sub>	493.3 (0.1) 350 (0.5) 125.8 (5)	80% (150, 0.5)	[49]
Bi <sub>0.09</sub> MnO <sub>2</sub> ·1.5H <sub>2</sub> O (δ-MnO <sub>2</sub> )	one-step hydrothermal process (180 °C)	nanoflowers	2 M ZnSO <sub>4</sub> + 0.1 M MnSO <sub>4</sub>	175.5 (0.1) 65 (2)	96% (1100, 1) 72.3 % (500, 0.5)	[49]
Ag-doped α-MnO <sub>2</sub>	one-step hydrothermal process (120 °C)	nanowires	2 M ZnSO <sub>4</sub> + 0.1 M MnSO <sub>4</sub>	315 (0.05) 177 (0.5) 85 (2)	94.4% (500, 0.5)	[50]
Mo-doped α-MnO <sub>2</sub>	one-step hydrothermal process (120 °C)	nanorods	2 M ZnSO <sub>4</sub> + 0.2 M MnSO <sub>4</sub>	222.8 (0.1); 65.8 (5)	82.6% (1000, 2)	[51]
Mo-doped δ-MnO <sub>2</sub>	one-step hydrothermal method (120 °C)	flower-like nanospheres	2 M ZnSO <sub>4</sub> + 0.1 M MnSO <sub>4</sub>	327 (0.2) 207 (1) 107 (3)	76.8% (1000, 1)	[52]
La <sup>3+</sup> -inserted δ-MnO <sub>2</sub>	redox reaction	nanoflorets	1 M ZnSO <sub>4</sub> + 0.4 M MnSO <sub>4</sub>	278.5 (0.1)	71% (200, 0.2)	[53]
Ce-doped α-MnO <sub>2</sub>	one-step hydrothermal method (140 °C)	nanorod-like structure	2 M ZnSO <sub>4</sub> + 0.1 M MnSO <sub>4</sub>	134 (1.54)	74% (100, 1.54)	[54]
Ce-MnO <sub>2</sub> @CC	one-step electrodeposition	porous lamellar structures	PAM/2 M ZnSO <sub>4</sub> + 0.1 M MnSO <sub>4</sub>	292 (0.1) 212 (0.5) 106 (2)	64% (450, 0.1)	[55]
Al-intercalated α-MnO <sub>2</sub>	one-step hydrothermal method (140 °C)	nanorods	PVA: 1 M ZnSO <sub>4</sub> (1:4)	333.6 (1) 198.6 (4)	94.5% (2000, 2)	[24]
Al-Doped α-MnO <sub>2</sub> coated by Lignin	one-step hydrothermal process (200 °C)	1D nanorod structures	2 M ZnSO <sub>4</sub> + 0.2 M MnSO <sub>4</sub>	~420 (0.1) 180 (1.5)	66.7% (3000, 1.5)	[56]
Al <sup>3+</sup> pre-intercalated K <sub>0.27</sub> MnO <sub>2</sub> ·0.54H <sub>2</sub> O (δ-MnO <sub>2</sub> )	modified hydrothermal method (160 °C)	spherical microflowers	2 M ZnSO <sub>4</sub> + 0.1 M MnSO <sub>4</sub>	323.7 (0.1) 250 (0.5) 191.7 (2)	99% (300, 0.5)	[57]
α-MnO <sub>2</sub> @KCoAl	co-precipitation method	irregular lumpy particles with agglomeration	2 M ZnSO <sub>4</sub> + 0.05 M MnSO <sub>4</sub>	524 (0.5) 431 (1) 221 (5)	~66.4% (100, 0.5)	[58]
Bi-doped α-MnO <sub>2</sub>	redox process followed by annealing	nanoparticles	2 M ZnSO <sub>4</sub> + 0.2 M MnSO <sub>4</sub>	363 (0.1) 286 (0.6) 197 (1)	93% (10,000, 1)	[59]
Sn-doped α-MnO <sub>2</sub>	hydrothermal process (180 °C) with further calcination	nanorods	2 M ZnSO <sub>4</sub> + 0.1 M MnSO <sub>4</sub>	210 (0.1) 106 (1)	80 % (500, 1)	[30]

### 3. Manganese-Oxide-Conducting Polymer Composite Cathodes for AZIBs

Intrinsically conducting polymers are promising materials for improving the electrochemical performance of cathodes due to their high electronic and ionic conductivity, chemical inertness, and low solubility in aqueous media [61,62]. The most commonly used conducting polymers are polyaniline, polypyrrole, and poly(3,4-ethylenedioxythiophene) due to the many possible polymerization routes that can be easily controlled. It should also be noted that conducting polymers could be used to coat the electroactive grains or to intercalate polymer fragments into the manganese dioxide lattice. On the other hand, it has been reported that coating the zinc anode with conducting polymers also stabilizes the Zn//MnO<sub>2</sub> cell [63].

#### 3.1. Polyaniline-Modified MnO<sub>2</sub> Cathodes

Polyaniline (PANI) is a frequently investigated conducting polymer in the field of energy storage materials due to several advantages, such as ease of synthesis, environmental friendliness, low cost, and high conductivity [64]. Generally, composites of MnO<sub>2</sub> with PANI have been prepared by chemical polymerization reaction between aniline and

potassium permanganate or by self-polymerization of aniline in the presence of  $\text{MnO}_2$  in acidic environment. Such syntheses allow researchers to obtain polymer coatings on the surface of electroactive grains, interfacial 3D networks, and PANI-intercalated materials.

One of the ways to obtain PANI–manganese-oxide composites is the reaction between  $\text{KMnO}_4$  and aniline without the addition of an acid. In the case of an interfacial gas/liquid reaction of evaporated aniline and the solution of potassium permanganate, layered  $\text{MnO}_2$ @PANI nanohybrids were obtained by layer-by-layer formation [65]. During the reaction, black powder was formed on the surface of the  $\text{KMnO}_4$  solution. The XRD pattern of the sample exhibited several peaks that are consistent with a 2H birnessite structure. From the XPS spectra of the manganese, it was confirmed that the valence state of Mn is close to +4, and the nitrogen XPS spectra correspond to a PANI structure. The weight percentage of PANI in the composite was  $\approx 4.5\%$  according to the TGA analysis. The morphology of the  $\text{MnO}_2$ @PANI composites, as observed from the large-scale SEM images, was a 3D mesoporous framework with a high surface area ( $255 \text{ m}^2 \cdot \text{g}^{-1}$  from the BET measurements). High-resolution TEM characterization revealed two phases: the ordered core associated with  $\text{MnO}_2$  and the amorphous shell consisting of PANI. The lattice spacing in the  $\text{MnO}_2$  was close to 0.37 nm, which correlated well with the XRD patterns. The electrochemical properties of the composite cathodes were evaluated in an aqueous solution of 2 M  $\text{ZnSO}_4$  with an additive of 0.2 M  $\text{MnSO}_4$ . At the low current density of  $0.1 \text{ A} \cdot \text{g}^{-1}$ ,  $\text{MnO}_2$ @PANI nanohybrids delivered a specific capacity as high as  $310 \text{ mAh} \cdot \text{g}^{-1}$ , and  $109 \text{ mAh} \cdot \text{g}^{-1}$  at  $2.0 \text{ A} \cdot \text{g}^{-1}$ . The cycling stability of the  $\text{MnO}_2$ @PANI nanohybrids was evaluated at  $0.5 \text{ A} \cdot \text{g}^{-1}$  for 500 cycles. For the first 20 charge/discharge cycles, a gradual increase in capacity was observed; then, after 100 cycles, the capacity fading was 30%; and then the capacity stabilized. After 500 cycles, the electrode material exhibited a specific capacity of  $188 \text{ mAh} \cdot \text{g}^{-1}$ . Such a good electrochemical performance of  $\text{MnO}_2$ @PANI can be explained by the polyaniline surface coating, which prevents the dissolution and phase transformation of  $\text{MnO}_2$  during cycling. The increase in capacity during the first cycles can be related to the presence of  $\text{Mn}^{2+}$  ions in the electrolyte solution and the electrodeposition of a  $\text{MnO}_x$  electroactive layer on the electrode surface.

Another method to carry out the chemical polymerization reaction is the interfacial process between reagents in aqueous and organic media (aniline solution in  $\text{CCl}_4$  and aqueous solution of  $\text{KMnO}_4$ ) (Figure 9a). This process allowed researchers to obtain PANI-intercalated manganese dioxide [66]. The mechanism of this process involves the oxidation of the aniline monomer, reduction of the permanganate anion, and diffusion of PANI into the crystal lattice of  $\text{MnO}_2$ , resulting in a layer-by-layer formation of a composite material with a mesoporous structure. The composite material obtained had a porous structure with polycrystalline fragments, as observed from the TEM data. The HR-TEM study after heat treating showed that the interlayer distance in the  $\text{MnO}_2$  structure was expanded to nearly 1.0 nm. From the XRD patterns, it was concluded that the material was highly amorphous, with many large crystalline fragments. This was related to the expansion of the  $\text{MnO}_2$  structure by PANI. At the same time, small diffraction peaks at  $2\theta$  12.04, 36, and  $65^\circ$  were associated with the birnessite structure (or  $\delta$ - $\text{MnO}_2$ ). The specific surface area of the composite was  $277 \text{ m}^2 \cdot \text{g}^{-1}$ . Thus, the reaction between aniline and potassium permanganate allows researchers to obtain composites with a mesoporous morphology and high specific surface area. The electrochemical properties of this composite material were tested in aqueous 2 M  $\text{ZnSO}_4$  / 0.1 M  $\text{MnSO}_4$  solution. In the first discharge cycle at  $0.05 \text{ A} \cdot \text{g}^{-1}$ , two main regions were observed: a sloping discharge profile from 1.55 to 1.33 V with a capacity of  $50 \text{ mAh} \cdot \text{g}^{-1}$  and the voltage plateau at  $E = 1.36 \text{ V}$  with a capacity of  $210 \text{ mAh} \cdot \text{g}^{-1}$  (Figure 9b). In the second cycle, the capacity of PANI-intercalated  $\text{MnO}_2$  was  $298 \text{ mAh} \cdot \text{g}^{-1}$ , which is close to the theoretical value ( $308 \text{ mAh} \cdot \text{g}^{-1}$ ). Even at the high current density ( $3.0 \text{ A} \cdot \text{g}^{-1}$ ), this material still delivered the specific capacity as high as  $110 \text{ mAh} \cdot \text{g}^{-1}$ . Over 200 cycles at a current density of  $0.2 \text{ A} \cdot \text{g}^{-1}$ , the capacity retention was close to 90%, with excellent coulombic efficiency. It has been suggested [66] that the reinforced structure of manganese oxide, achieved via intercalation of polyaniline

oligomers between  $\text{MnO}_2$  layers, is more stable to  $\text{H}^+/\text{Zn}^{2+}$  co-insertion, and no collapse of the structure occurred during repeated insertion/extraction of hydrated cations. It was also demonstrated that PANI-intercalated  $\text{MnO}_2$  can be successfully cycled in solution without the manganese sulfate additive. Capacity decay was observed during several initial cycles due to manganese dissolution; however, from the 5th to the 200th cycle, the capacity decay was very slow. Thus, PANI fragments between  $\text{MnO}_2$  layers allow researchers to stabilize the crystal lattice and increase the cycle life of the composite materials.

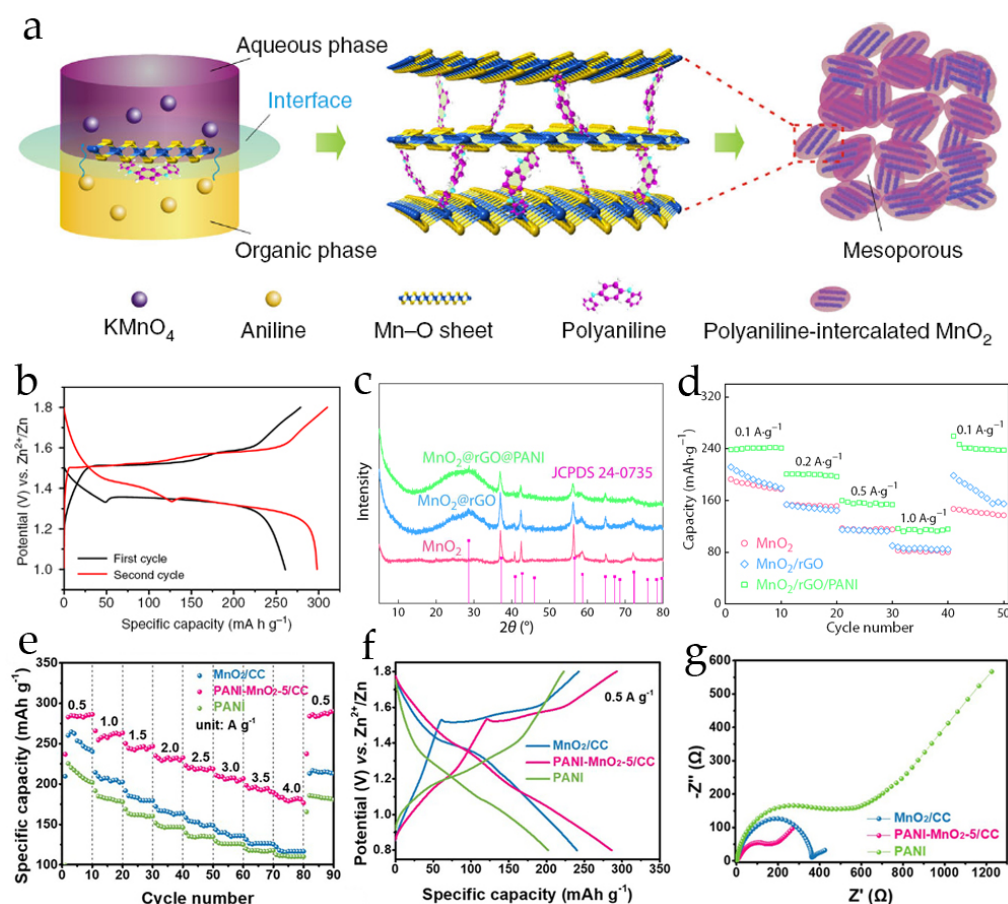


**Figure 9.** (a) Scheme of the reaction between aniline and potassium permanganate and the expanded structure of PANI-intercalated  $\text{MnO}_2$  nanolayers [66]. (b) Typical galvanostatic charge/discharge curves of PANI-intercalated  $\text{MnO}_2$  cathode at  $0.05 \text{ A}\cdot\text{g}^{-1}$  [66]. (c) XRD patterns and (d) C-rate capabilities of  $\text{MnO}_2$ ,  $\text{MnO}_2/\text{rGO}$ , and  $\text{MnO}_2/\text{rGO}/\text{PANI}$  composites [67]. (e) Rate performance and (f) Galvanostatic discharge/charge curves of  $\text{MnO}_2/\text{CC}$ , PANI- $\text{MnO}_2/\text{CC}$  and PANI [68]. (g) Nyquist plots for  $\text{MnO}_2/\text{CC}$ , PANI- $\text{MnO}_2/\text{CC}$ , and PANI [68].

The development of composite materials with conducting polymers and carbon additives is aimed at improving the overall electronic and ionic conductivity of  $\text{MnO}_2$  and its mechanical stability. A polyaniline-coated aerogel of  $\text{MnO}_2$  and reduced graphene oxide (rGO),  $\text{MnO}_2/\text{rGO}/\text{PANI}$ , was prepared by a two-step process of mechanical mixing of  $\text{MnO}_2$  and rGO and hydrothermal treatment, followed by in situ polymerization of aniline at a low temperature in the presence of ammonium persulfate as oxidant in hydrochloric acid [67]. The resulting  $\text{MnO}_2/\text{rGO}/\text{PANI}$  aerogel had a dense and compact structure, and the uniform distribution of Mn, O, C, and N elements demonstrated by the EDX analysis confirmed the complete coating of the aerogel by PANI. The specific surface area of the composite was  $142 \text{ m}^2\cdot\text{g}^{-1}$ . The XRD patterns of the  $\text{MnO}_2/\text{rGO}/\text{PANI}$  composite material clearly showed that  $\beta\text{-MnO}_2$  retained its crystal structure throughout the synthetic operations (Figure 9c). An additional broad peak at  $26^\circ$  on the XRD patterns of  $\text{MnO}_2/\text{rGO}$

and MnO<sub>2</sub>/rGO/PANI composites was attributed to the presence of graphene oxide, and the resulting composite was more amorphous due to the presence of PANI. The XPS characterization confirmed the structure and composition of the aerogel. The electrochemical properties of the composite were evaluated in the aqueous 2 M ZnSO<sub>4</sub> electrolyte without Mn<sup>2+</sup> additive, and at the current density of 0.1 A·g<sup>-1</sup>, the MnO<sub>2</sub>/rGO/PANI delivered the specific capacity of 241 mAh·g<sup>-1</sup>, while at 1.0 A·g<sup>-1</sup>, the reversible capacity value of 111.7 mAh·g<sup>-1</sup> was achieved (Figure 9d). Both values were 45% higher than those of a pristine MnO<sub>2</sub> or MnO<sub>2</sub>/rGO composite. Furthermore, the capacity decay of the ternary composite was the lowest (13.3% per 600 cycles). The suppression of the manganese dissolution during the charge/discharge by the polyaniline layer is the main reason for the high electrochemical performance. An evaluation of the diffusion rate by GITT showed high diffusion coefficients in the range of 10<sup>-9</sup>–10<sup>-11</sup> cm<sup>2</sup>·s<sup>-1</sup>, which is two orders higher than that of binary composite or pristine MnO<sub>2</sub>. Such high values were achieved due to the high electronic and ionic conductivity of rGO and PANI, which accelerate the diffusion of Zn<sup>2+</sup> ions.

MnO<sub>2</sub> that was obtained hydrothermally on carbon cloth substrate was dispersed in acidic aniline solution for several hours to obtain PANI-MnO<sub>2</sub>/CC three-dimensional networks [68]. During the synthesis, MnO<sub>2</sub> nanosheets were formed on the carbon cloth's surface. Initially, MnO<sub>2</sub>/CC 3D structures were formed by growing MnO<sub>2</sub> nanosheets on the carbon cloth's surface, and the addition of PANI led to an increase in the roughness of the surface. According to the EDX mapping of Mn, O, C, and N, the inorganic components and PANI coating were homogeneously dispersed in the composite. From the HR-TEM and XRD measurements, it was found that layered δ-MnO<sub>2</sub> was formed during the synthesis. The valence state of manganese (Mn<sup>+4</sup>) and the polymer structure were also confirmed by XPS and Raman spectroscopy. Charge/discharge tests of the PANI-MnO<sub>2</sub>/CC binder-free electrode in the mixed 2 M ZnSO<sub>4</sub>/0.1 M MnSO<sub>4</sub> electrolyte showed an excellent specific capacity of 286 mAh·g<sup>-1</sup> at a current density of 0.5 A·g<sup>-1</sup>, and at the high current density of 4.0 A·g<sup>-1</sup>, the delivered capacity was 177 mAh·g<sup>-1</sup> (Figure 9e). Such large capacity values can be attributed to the high electrical and ionic conductivity of PANI, the high porosity of the 3D networks with a greater number of adsorption sites, and the pseudocapacitive charge storage in the PANI itself, as seen in the charge/discharge profiles (Figure 9f). The capacity retention of the PANI-MnO<sub>2</sub>/CC composite was 90.2% after 1800 cycles at a current density of 2.0 A·g<sup>-1</sup>, and 96.9% after 9000 cycles at I = 4.0 A·g<sup>-1</sup>, based on the initial specific capacity value. The changes in capacity during continuous cycling were non-linear: first, a decrease in capacity was observed, and then the capacity increased and decreased back to near the initial values. Such changes are associated with the presence of Mn<sup>2+</sup> ions in the electrolyte solutions. This high stability allowed the authors [68] to conclude that the PANI coating prevents the dissolution of manganese during cycling, while the artificial increase in the specific capacity occurs due to the Mn<sup>2+</sup>-Mn<sup>+4</sup> redox reaction and the formation of MnO<sub>x</sub>. PANI-MnO<sub>2</sub>/CC also exhibited the lowest charge-transfer resistance, as compared to MnO<sub>2</sub>/CC and pristine PANI (Figure 9g). The slope in the low frequency region of the EIS spectra of PANI-MnO<sub>2</sub>/CC was higher than that of MnO<sub>2</sub>/CC and PANI, indicating that the PANI effectively enhances the zinc-ion diffusion rate in the composite. The Zn<sup>2+</sup> diffusion coefficient of the PANI-MnO<sub>2</sub>/CC (2.33·10<sup>-11</sup> cm<sup>2</sup>·s<sup>-1</sup>), as determined by GITT, was higher than that of MnO<sub>2</sub>/CC (5.06·10<sup>-12</sup> cm<sup>2</sup>·s<sup>-1</sup>), indicating a faster Zn<sup>2+</sup> transport rate in PANI-MnO<sub>2</sub>/CC.

The in situ polymerization of PANI on the MnO<sub>2</sub> ultralong nanowires was proposed in [69] to obtain a core-shell MnO<sub>2</sub>@PANI composite material, which was used as a binder-free cathode for AZIBs. As a result of the redox process between aniline monomer and MnO<sub>2</sub>, ultralong nanowires interconnected in a highly porous architecture were obtained. No significant changes in the morphology of the material were observed after polymerization, so the PANI coating was considered homogeneous. Based on HR-TEM and XRD patterns, tetragonal α-MnO<sub>2</sub> was obtained during the hydrothermal synthesis and was retained after aniline polymerization. The structure of PANI was confirmed by FTIR and



Raman spectroscopy, and the amount of polymer coating was  $\approx 10.5\%$  according to TGA analysis. XPS measurements also confirmed the structure of PANI due to the presence of nitrogen peaks in the survey spectra and the +4 valence of manganese. The electrochemical measurements were carried out in an aqueous solution of 2 M  $\text{ZnSO}_4/0.1$  M  $\text{MnSO}_4$ . The polarization value for the  $\text{MnO}_2@$ PANI composite electrode was lower than that of the electrode prepared from unmodified  $\text{MnO}_2$  nanowires. At the low current of  $0.2 \text{ A}\cdot\text{g}^{-1}$ , the capacity at the 50th cycle was  $343 \text{ mAh}\cdot\text{g}^{-1}$  due to  $\text{MnO}_x$  electrodeposition during the cycling process. At the high current density of  $3.0 \text{ A}\cdot\text{g}^{-1}$ , the delivered capacity was  $100 \text{ mAh}\cdot\text{g}^{-1}$ . The long-term stability of the  $\text{MnO}_2@$ PANI hybrid cathodes was investigated at  $I = 0.5$  and  $I = 2.0 \text{ A}\cdot\text{g}^{-1}$  over 300 and 2000 cycles, and the capacity retention was close to 80% regardless of the applied current. It was suggested that the main role of the PANI coating is to improve the mechanical integrity and conductivity of the composite material.

Thus, PANI-coated  $\text{MnO}_2$  cathodes for AZIBs have better stability because PANI prevents the dissolution of  $\text{Mn}^{2+}$  from the electrode surface and provides higher conductivity within the electrode material. It is interesting to note that PANI can be intercalated into the layered  $\text{MnO}_2$ , as has been described for vanadium-based materials [70–72]. The intercalation of PANI between the crystal lattice layers also improves the mechanical stability.

### 3.2. Polypyrrole-Modified $\text{MnO}_2$ Cathodes

Polypyrrole (PPy) is a conducting polymer that is widely used in composite materials due to its low solubility in various solvents, large surface area, high conductivity, non-toxicity, and chemical and electrochemical stability [73]. In particular, PPy can be used in energy storage materials [74,75], and it is more stable compared to PANI [76]. Like any other conducting polymer, the properties of PPy depend on the polymerization reaction conditions and methods [77]. PPy is typically used as a coating on the  $\text{MnO}_2$  surface, which is obtained by different methods, including self-polymerization and chemical or electrochemical oxidation of pyrrole monomer.

The chemical polymerization of pyrrole in solution with dispersed  $\text{MnO}_2$  was performed at low temperatures by adding aqueous  $\text{FeCl}_3$  solution to obtain a  $\text{MnO}_2$ /PPy composite (Figure 10a) [78]. The composite maintained the morphology of the initial  $\text{MnO}_2$  nanorods (Figure 10b). Based on density functional theory calculations and HR-TEM images, it was concluded that the crystal lattice of the  $\text{MnO}_2$ /PPy composite is more disordered than that of pristine  $\text{MnO}_2$ . An amorphous coating of PPy was detected on the tetragonal  $\alpha$ - $\text{MnO}_2$  nanorods by the XRD and TEM. Strong interactions between the  $\text{MnO}_2$  lattice and the pyrrole rings were confirmed by the presence of the Mn-N bond in the XPS spectra of N 1s at 399.2 eV (Figure 10c) and additionally confirmed by DFT calculations. The electrochemical performance of the  $\text{MnO}_2$ /PPy cathode material was evaluated in 2 M  $\text{ZnSO}_4$  aqueous solution in the presence and absence of 0.1 M  $\text{MnSO}_4$ . The remarkable specific capacity of  $256 \text{ mAh}\cdot\text{g}^{-1}$  was observed after 100 cycles at  $I = 0.1 \text{ A}\cdot\text{g}^{-1}$ , with a gradual increase of the capacity, while for bare  $\text{MnO}_2$  nanorods, the capacity fading under the same conditions was 45%. The  $\text{MnO}_2$ /PPy composite showed a high rate performance ( $90 \text{ mAh}\cdot\text{g}^{-1}$  at  $1.5 \text{ A}\cdot\text{g}^{-1}$ ). Moreover, in the absence of the  $\text{MnSO}_4$  additive, 66% capacity retention was observed for the composite material (Figure 10d). One of the explanations for the increase in capacity is the additional pseudocapacitive charge storage in the PPy coating. The study of manganese dissolution by ICP analysis had shown that it was mitigated by the presence of a protective PPy shell on the surface of  $\text{MnO}_2$  grains that was chemically bound to the  $\text{MnO}_2$  core. The kinetic parameters (activation energy and diffusion coefficients) obtained by impedance spectroscopy and cyclic voltammetry showed that the diffusion of  $\text{Zn}^{2+}$  ions was more effective for the  $\text{MnO}_2$ /PPy composite.

Pre-synthesized PPy nanowires were added to  $\text{MnSO}_4$  solution in the presence of ammonium persulfate to obtain a  $\beta$ - $\text{MnO}_2$ /PPy composite [79]. The diffraction peaks of the as-synthesized product corresponded well to tunnel-type  $\beta$ - $\text{MnO}_2$ . The morphology of the  $\beta$ - $\text{MnO}_2$ /PPy composite was described as microspheres formed by PPy nanowires and  $\text{MnO}_2$  nanorods. However, the specific surface area of the composite calculated from BET

measurements was only  $47.3 \text{ m}^2 \cdot \text{g}^{-1}$ , which is much lower than for other composites with PANI [65]. The valence state of manganese (+4) was calculated from XPS spectra, and the interactions between N and Mn elements were also observed. The rate performance studied in conventional electrolyte (2 M  $\text{ZnSO}_4$ /0.1 M  $\text{MnSO}_4$ ) showed that the specific capacity of  $\text{MnO}_2/\text{PPy}$  was  $215 \text{ mAh} \cdot \text{g}^{-1}$  at  $0.1 \text{ A} \cdot \text{g}^{-1}$  and  $105 \text{ mAh} \cdot \text{g}^{-1}$  at  $1.0 \text{ A} \cdot \text{g}^{-1}$ , which is 30–40% higher than that of unmodified  $\text{MnO}_2$ . The specific capacity during long-term cycling at  $0.2 \text{ A} \cdot \text{g}^{-1}$  (160 cycles) gradually increased due to the  $\text{MnO}_x$  electrodeposition during cycling, while the capacity degradation for unmodified manganese oxide was about 50%. Such advantages of the  $\text{MnO}_2/\text{PPy}$  composite may be related to the randomly oriented morphology of the material, which consists of PPy nanowires and  $\text{MnO}_2$  nanorods. Such porous architecture of the composite material, which improves its ionic conductivity, facilitates  $\text{Zn}^{2+}$  and  $\text{H}^+$  diffusion into the material. In addition, highly conductive PPy nanowires located between  $\text{MnO}_2$  nanorods provide better electronic contact within the composite material.

Composite materials with polypyrrole and carbon additives have also been used for  $\text{MnO}_2$ -based cathodes to improve their electrical conductivity. Ternary composites based on  $\text{MnO}_2$  with carbon nanotubes (CNTs) coated with PPy have been successfully applied in AZIBs [80,81] with superior properties. PPy was obtained by in situ oxidation of pyrrole by  $\text{MnO}_2$  nanowires in the presence of CNTs (CNT/ $\text{MnO}_2$ -PPy). As a result,  $\alpha$ - $\text{MnO}_2$  was obtained, and its structure was preserved after the polymerization of pyrrole. The X-ray diffraction data with a peak at  $25.84^\circ$  indicated the presence of PPy in the composite, and the lower intensity of the XRD peaks suggested that the  $\text{MnO}_2$  in the composite material was more amorphous than the initial oxide. A three-dimensional interconnected network, in which all components are uniformly distributed, was formed during the reaction. The morphology of the CNT/ $\text{MnO}_2$ -PPy composite was porous, with macropores of several micrometers in size. Highly dispersed  $\text{MnO}_2/\text{PPy}$  nanowires were surrounded by CNT networks. The cycling stability and rate performance of the CNT/ $\text{MnO}_2/\text{PPy}$  cathode material were investigated in the conventional electrolyte with a  $\text{Mn}^{2+}$  additive. At the low current density ( $0.1 \text{ A} \cdot \text{g}^{-1}$ ) the specific capacity value was  $\approx 250 \text{ mAh} \cdot \text{g}^{-1}$ , and at  $I = 2.0 \text{ A} \cdot \text{g}^{-1}$ , it was  $84.2 \text{ mAh} \cdot \text{g}^{-1}$ . The cycling stability was investigated at the current densities of  $0.3 \text{ A} \cdot \text{g}^{-1}$  (200 cycles) and  $1.0 \text{ A} \cdot \text{g}^{-1}$  (1000 cycles). In both cases, the capacity decay was less than 15% [81]. At  $I = 0.3 \text{ A} \cdot \text{g}^{-1}$ , the initial gradual increase in capacity was observed. The kinetic investigations showed that the charge-transfer resistance of the ternary composite is lower, and the diffusion coefficient is twice as high for both  $\text{H}^+$  and  $\text{Zn}^{2+}$  cations. These improved properties can be explained by the high porosity of the network, the conductivity of the CNTs and PPy, and the formation of a protective layer that prevents manganese dissolution. Such a unique architecture provides abundant sites for  $\text{Zn}^{2+}$  and  $\text{H}^+$  adsorption, resulting in additional pseudocapacitive charge storage.

Another carbon additive, graphene oxide, has also been used to develop ternary composites with  $\text{MnO}_2$  and PPy [82]. For this purpose, an  $\alpha$ - $\text{MnO}_2/\text{rGO}$  composite was prepared hydrothermally from  $\text{MnSO}_4$ ,  $\text{KMnO}_4$ , and graphene oxide. Then the chemical polymerization of PPy was carried out in a solution of as-prepared  $\alpha$ - $\text{MnO}_2/\text{rGO}$  material in an acidic environment, with ammonium persulfate as the oxidizing agent. No significant structural changes occurred after the polymerization: the position of the main peaks in the XRD patterns of pristine  $\alpha$ - $\text{MnO}_2$  and  $\alpha$ - $\text{MnO}_2/\text{rGO}$ -PPy did not change. The composites had the morphology of nanowires coated with conducting polymer, forming continuous conductive networks. As seen from the XPS spectra, the valence state of manganese is dual:  $\text{Mn}^{3+}$  and  $\text{Mn}^{4+}$ , which can be related to the oxidation of pyrrole not only by  $(\text{NH}_4)_2\text{S}_2\text{O}_8$  but also by  $\text{MnO}_2$  itself (Figure 10e). The cathode material based on the ternary  $\alpha$ - $\text{MnO}_2/\text{rGO}/\text{PPy}$  composite delivered  $438 \text{ mAh} \cdot \text{g}^{-1}$  at  $I = 0.1 \text{ A} \cdot \text{g}^{-1}$  and  $190.2 \text{ mAh} \cdot \text{g}^{-1}$  at  $1.0 \text{ A} \cdot \text{g}^{-1}$ . Such a high capacity can be explained by the conductive network formed by rGO and PPy and also by the pseudocapacitive properties of both components. The capacity decay for the ternary composite was the lowest (14.1%), while for the binary  $\alpha$ - $\text{MnO}_2/\text{rGO}$  composite, it was 36.5%. Thus, the main contributor to the electrochemical

performance improvement is the carbon additive, while the conducting polymer enhances its benefits.

The combination of two different manganese oxides with the PPy layer has also been discussed as a way to improve the electrochemical performance of Zn//MnO<sub>2</sub> batteries. The molten salt synthesis of MnO<sub>2</sub>/Mn<sub>2</sub>O<sub>3</sub> (Mn-O-3) nanocomposite and the self-polymerization of PPy were performed in [83]. During the synthesis, nanobelts and nanoparticles of Mn-O-3 coated with a dense shell of amorphous polypyrrole were obtained. According to the XRD patterns, the nanocomposite consisted of two oxides ( $\alpha$ -MnO<sub>2</sub> and Mn<sub>2</sub>O<sub>3</sub>), and more diffraction peaks of  $\alpha$ -MnO<sub>2</sub> could be indexed. Based on the ICP analysis, the content of Mn<sub>2</sub>O<sub>3</sub> in the composite was about 34.1%. Depending on the synthesis time, the weight content of the PPy shell in the composite varied from 0.64% to 1.96%, as was shown by TGA. At the low current density of 0.2 A·g<sup>-1</sup>, the specific capacity of cathodes with a Mn-O-3 composite with thin PPy coating was 289.8 mAh·g<sup>-1</sup>, while at I = 3.0 A·g<sup>-1</sup>, the capacity was 199.8 mAh·g<sup>-1</sup>. Increasing the thickness of the PPy coating resulted in an insignificant decrease in capacity over the entire current range. These excellent values were explained by the high conductivity of the PPy film (21.4 S·cm<sup>-1</sup>), which is much higher than that of MnO<sub>2</sub>. The cycling stability was evaluated in 2 M ZnSO<sub>4</sub> electrolytes with/without manganese sulfate additive. At I = 3.0 A·g<sup>-1</sup> in a 2 M ZnSO<sub>4</sub>/0.2 M MnSO<sub>4</sub> electrolyte, the capacity retention during 1000 cycles was over 100% due to the capacity increase caused by the formation of electroactive MnO<sub>x</sub> layer. In pure 2 M ZnSO<sub>4</sub> solution at I = 1.0 A·g<sup>-1</sup>, the capacity retention over 1000 cycles was 80.5%, which is a remarkable value. It is related to the protective PPy layer on the Mn-O-3 composite surface, which prevents manganese dissolution during the cycling process. Kinetic studies showed that the polarization of the cells and the charge-transfer resistance decreased for PPy-coated Mn-O-3, while the diffusion of Zn<sup>2+</sup> and H<sup>+</sup> was faster than for the uncoated Mn-O-3 composite.

Conducting polymer coatings can also be applied to modified oxides, e.g., for oxides doped with heterovalent atoms. Iron-doped MnO<sub>2</sub> coated with PPy was proposed as a cathode in [84]. First, Fe<sup>3+</sup>-doped MnO<sub>2</sub> was prepared from Mn(CH<sub>3</sub>COO)<sub>2</sub>, KMnO<sub>4</sub>, and a small amount of Fe(NO<sub>3</sub>)<sub>3</sub> via the chemical precipitation method. Then the self-polymerization of PPy was performed at 0 °C for 5 h. The samples had a highly porous morphology consisting of microspheres. Based on the EDX analysis, uniform distribution of Mn, O, C, N, and Fe elements was observed, so it was concluded that the uniform polymer coating was formed on the whole surface. The specific surface area of the material was 56 m<sup>2</sup>·g<sup>-1</sup>. A tetragonal  $\alpha$ -MnO<sub>2</sub> crystal structure was found from the XRD patterns, and for Fe<sup>3+</sup>-doped  $\alpha$ -MnO<sub>2</sub> samples, the shift of the diffraction peak at  $2\theta = 37.52^\circ$  to lower  $2\theta$  angles was probably due to the partial substitution of Mn<sup>4+</sup> by Fe<sup>3+</sup>. The PPy-coated sample was more amorphous, but the  $\alpha$ -MnO<sub>2</sub> crystal structure was maintained. As shown by XPS, the valence state of manganese and iron was +4 and +3, respectively, so Fe<sup>3+</sup> ions did not react with pyrrole monomer or manganese precursors. The initial capacity of the Fe-doped MnO<sub>2</sub>@PPy composite at a current density of 0.1 A·g<sup>-1</sup> was 270 mAh·g<sup>-1</sup>. However, at the high current density of 1.0 A·g<sup>-1</sup>, it was only 73 mAh·g<sup>-1</sup>. The capacity fading over 100 cycles at I = 0.1 A·g<sup>-1</sup> was  $\approx 75\%$ . This electrochemical performance is mainly attributed to the increased interlayer spacing of manganese oxide and oxygen defects due to the substitution of Mn<sup>4+</sup> to Fe<sup>3+</sup>. At the same time, the PPy coating improves the conductivity of the composite. Thus, the iron doping and PPy conductive network can not only facilitate zinc ion migration and electron transport but also reduce manganese dissolution from the material.

Finally, the MnO<sub>2</sub>/PPy composite was used for the development of flexible zinc-ion batteries [85]. For this purpose, the cathode was electrodeposited on stainless-steel yarns from manganese acetate solution in the presence of sodium sulfate. According to the XRD patterns,  $\alpha$ -MnO<sub>2</sub> was the main crystalline phase of the electrodeposited cathode material. After the deposition of MnO<sub>2</sub>, the surface of individual stainless-steel yarn fibers became rougher, and after the coating of MnO<sub>2</sub>@SS with PPy, the morphology was

further changed, and the higher surface area of the resulting material was favorable for the charging/discharging process. The presence of PPy in the composite was confirmed by Raman spectroscopy. To assemble the cell, the cathode yarn was wound around a Zn@Nitinol wire, which served as the anode. Gelatin–borax flexible gel electrolyte containing 1 M  $\text{ZnSO}_4$ /0.1 M  $\text{MnSO}_4$  encapsulated the electrodes and served as a separator (Figure 10f). The rate performance tests showed that the specific capacity of this battery was  $174.2 \text{ mAh}\cdot\text{g}^{-1}$  at 0.5 C and  $60 \text{ mAh}\cdot\text{g}^{-1}$  at 4 C, and the capacity retention at 2 C over 1000 cycles was  $>60\%$ . In addition, this battery was stable to mechanical deformation, such as bending, without significant capacity degradation. This was probably achieved due to the PPy coating on the surface of the  $\text{MnO}_2$ -electrode, which provided not only electrical but also mechanical support for the active material and improved the conductivity and flexibility of the cell.

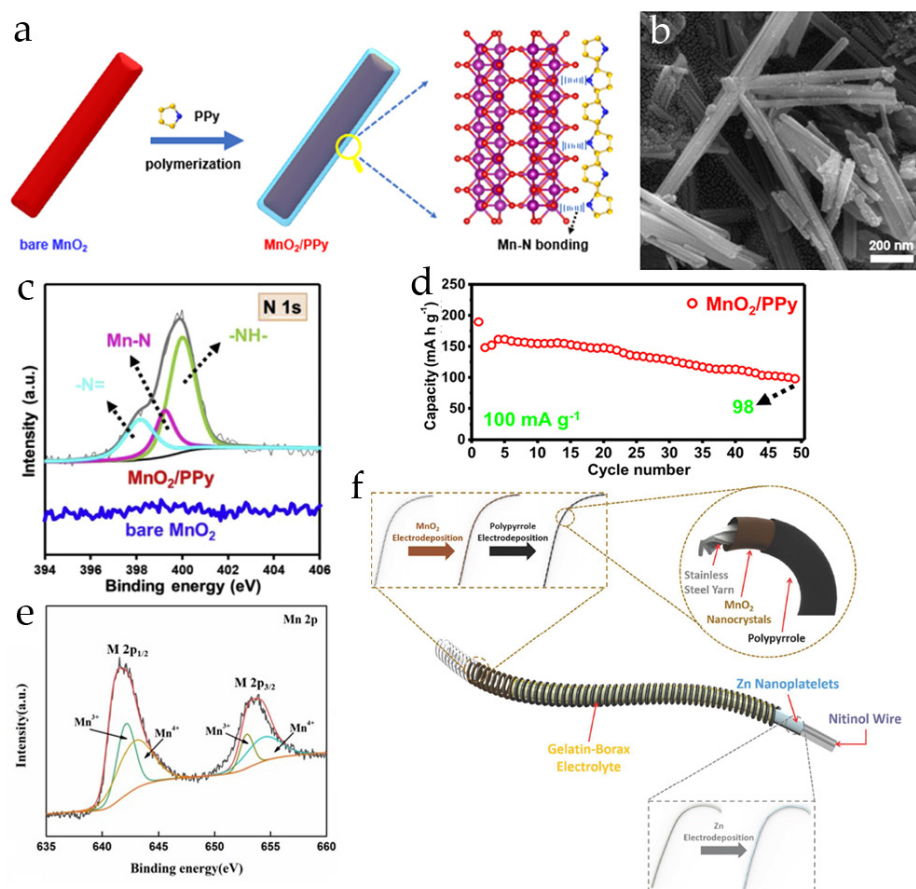


**Figure 10.** (a) Schematic diagram of synthesis of  $\text{MnO}_2/\text{PPy}$  composite [78]. (b) SEM image of  $\text{MnO}_2/\text{PPy}$  nanorod [78]. (c) High-resolution N 1s XPS spectrum of  $\text{MnO}_2/\text{PPy}$  composite [78]. (d) Continuous cycling performance of  $\text{MnO}_2/\text{PPy}$  electrode in 2 M  $\text{ZnSO}_4$  aqueous electrolyte [78]. (e) High-resolution Mn 2p and N 1s XPS spectra of  $\alpha\text{-MnO}_2/\text{rGO-PPy}$  composite [82]. (f) The construction of the flexible Zn// $\text{MnO}_2$  device with shape memory function [85].

Thus, polypyrrole-modified  $\text{MnO}_2$ -cathodes have advantageous properties due to the chemical bonding of the  $\text{MnO}_2$  core and the PPy shell, the high conductivity of the polymer, and the simplicity of the synthesis. However, the porosity and surface area of these composites are lower than those of PANI-modified cathodes, and PPy-intercalated  $\text{MnO}_2$  materials have not yet been obtained.

### 3.3. Poly(3,4-Ethylenedioxythiophene)-Modified MnO<sub>2</sub> Cathodes

Poly(3,4-ethylenedioxythiophene) (PEDOT) is one of the most stable derivatives of polythiophene due to the presence of two alkoxy substituents attached to the 3- and 4- positions of the thiophene ring. PEDOT itself and the aqueous dispersion of PEDOT with polystyrene sulfonate (PEDOT:PSS) are widely used for various applications, such as electrode materials for secondary power sources, solar cells, electrochromic devices, etc. [86,87]. PEDOT exhibits high stability in the doped state and excellent conductivity [88,89]; thermal, chemical, and electrochemical stability; and insolubility in aqueous and organic media. Typically, PEDOT-modified materials are obtained by electrodeposition or chemical oxidation of the monomer. PEDOT:PSS can be applied as received.

For manganese-based cathodes for AZIBs, the chemical or electrochemical deposition of manganese compounds, followed by deposition of the polymer, is a popular method to prepare MnO<sub>2</sub>/PEDOT composites [90–92], which can be further used as binder-free electrodes. In several cases, MnO<sub>2</sub>-based materials have also been electrodeposited on the substrate. A flexible quasi-solid battery with electrodeposited MnO<sub>2</sub>@PEDOT cathode, zinc anode, and 2 M ZnCl<sub>2</sub>/0.4 M MnSO<sub>4</sub> gel polymer electrolyte based on polyvinyl alcohol was developed in [90]. During the synthesis, polycrystalline  $\alpha$ -MnO<sub>2</sub> coated by the amorphous polymer layer was obtained. The EDX analysis showed the uniform distribution of Mn, O, C, and S elements, thus indicating that the composite coating was homogeneous. The predominant valence state of manganese was determined as Mn<sup>4+</sup> from the XPS spectra. The electrochemical performance of the composite was evaluated in liquid aqueous and gel polymer electrolytes. In the liquid aqueous electrolyte, the specific capacity was 366.6 mAh·g<sup>-1</sup> at a current density of 0.74 A·g<sup>-1</sup> and 143 mAh·g<sup>-1</sup> at I = 7.43 A·g<sup>-1</sup>. This excellent performance can be explained by the thin MnO<sub>2</sub> layer, the significant effect of the additional MnO<sub>x</sub> deposition, and the protective properties of the PEDOT layer on the composite surface. The cycling stability of the composite at a current density of 1.11 A·g<sup>-1</sup> was better in the presence of PEDOT due to the alleviation of manganese dissolution. The capacity retention of the composite electrode after 300 cycles was 83.7% compared to 47% for pristine MnO<sub>2</sub>. It was also found that PEDOT was not involved in the electrochemical reaction, and the full capacity of the electrode was provided by MnO<sub>2</sub>. The functional properties of the flexible quasi-solid cell with gel electrolyte were also remarkable: the specific capacities of 284 mAh·g<sup>-1</sup> at I = 0.37 A·g<sup>-1</sup> and 76 mAh·g<sup>-1</sup> at I = 5.58 A·g<sup>-1</sup> and capacity retention of 77% over 300 cycles at I = 1.86 A·g<sup>-1</sup>. The capacity decrease at high current densities was explained by the increase in charge-transfer resistance in the gel polymer electrolyte. The capacity degradation was associated with the slow dissolution and destruction of the composite material.

The above work [90] was further developed by synthesizing MnO<sub>2</sub>/PEDOT on carbon cloth modified with carbon nanotubes (CMOP) [91], which were chosen for their high electrical conductivity. CNTs were deposited on the carbon cloth surface via the chemical vapor deposition method, followed by electrodeposition of MnO<sub>2</sub> and PEDOT. The morphology of the composite was described as a coaxial-cable structure based on interconnected CNTs, with MnO<sub>2</sub> and a rough, thick layer of PEDOT deposited on each CNT array (Figure 11a). The crystal structure of the CMOP composite was  $\alpha$ -MnO<sub>2</sub>, as previously observed in [90]. The addition of CNTs to the composite allowed the researchers to achieve the specific capacity of 306.1 mAh·g<sup>-1</sup> at I = 1.1 A·g<sup>-1</sup>, and at the high current density of 10.8 A·g<sup>-1</sup>, the capacity was 176.8 mAh·g<sup>-1</sup>. In addition, it was shown that the capacity retention of the Zn//MnO<sub>2</sub> cell is not only determined by the cathode material, but also by the zinc anode: with the same cathode, replacing the zinc anode with the fresh one led to an increase in capacity and stability after 1000 cycles (Figure 11b) [91]. After the electrochemical tests, cracking and pulverization were observed on the SEM images of the MnO<sub>2</sub>/CNT electrode, while only negligible tiny cracks were observed for PEDOT-coated material. The capacity retention of the PEDOT-modified electrode was 71% before and 81% after replacement of the zinc anode. A flexible quasi-solid-state battery was assembled by sandwiching an aqueous poly(vinyl alcohol) (PVA) hydrogel electrolyte between the CMOP cathode and

Zn anode. The device demonstrated high-capacity retention (77.0%) after 500 cycles at a high current density of  $5.4 \text{ A g}^{-1}$  and close to 100% Coulombic efficiency (Figure 11c).

Another way to obtain  $\text{MnO}_2/\text{PEDOT}$  composites is the chemical deposition of  $\text{MnO}_2$  on a conductive substrate, followed by electrodeposition of the conducting polymer, which has been used for  $\text{Co}^{2+}$ -doped  $\text{MnO}_2$  grown on nickel foam [92]. In this work, a  $\text{Co-MnO}_2$  composite was prepared by precipitation from an acidic manganese acetate solution with a cobalt acetate additive, which was treated with sodium hydroxide and potassium persulfate with further annealing. The PEDOT layer was deposited potentiostatically from the solution containing EDOT, SDS, and  $\text{LiClO}_4$  as an electrolyte. The  $\text{Co-MnO}_2$  product consisted of uniform nanoflakes that were horizontally interconnected to form a highly open and porous structure. The presence of  $\text{Co}^{2+}$  ions increased the dimensions of the flakes, resulting in more effective electronic and ionic contact between the particles. The resulting  $\text{PEDOT@Co-MnO}_2$  material had a rough surface with irregular bulges. The main elements (Mn, O, Co, and S) were uniformly distributed in the composite material. No clear diffraction peaks were detected in the XRD patterns, indicating that the material was highly amorphous. The electrochemical properties of  $\text{PEDOT@Co-MnO}_2$  were investigated in 2 M  $\text{ZnSO}_4$  aqueous solution without manganese additive. Nevertheless, the specific capacity of  $\text{PEDOT@Co-MnO}_2$  was  $298.9 \text{ mAh}\cdot\text{g}^{-1}$  at  $I = 1 \text{ A}\cdot\text{g}^{-1}$ , while at  $I = 10 \text{ A}\cdot\text{g}^{-1}$ , it was  $150 \text{ mAh}\cdot\text{g}^{-1}$ . The absence of the  $\text{Mn}^{2+}$  additive explained the abrupt capacity drop for  $\text{MnO}_2$  and  $\text{Co-MnO}_2$  materials during continuous cycling, while for the PEDOT-coated composite, the capacity fading over 1000 cycles was only 7.7%. Thus, in the case of the  $\text{PEDOT@Co-MnO}_2$  material, the enlarged crystal lattice due to Co doping and conducting and protective PEDOT layer mitigate the structural deformations and facilitate  $\text{Zn}^{2+}$  and  $\text{H}^+$  transfer in the material.

An interesting approach to obtain a PEDOT-modified  $\text{MnO}_2$ -based cathode by electrodeposition of polymer on the electrode prepared by mechanical mixing of conventional components was proposed in [93]. For this purpose,  $\alpha\text{-MnO}_2$  and  $\delta\text{-MnO}_2$  were synthesized separately and then mixed in a 1:2 weight ratio to further prepare the electrode material by mixing manganese oxides with Super P carbon and polyvinylidene fluoride in a 7:2:1 weight ratio. Then the PEDOT layer was coated on the electrode surface by electrodeposition to prepare the PEDOT-coated electrode (DMOP). In the composite electrode, the particles of  $\delta\text{-MnO}_2$  were homogeneously distributed and interconnected by  $\alpha\text{-MnO}_2$  nanowires under the dense and smooth PEDOT layer. The EDX analysis showed a uniform distribution of Mn, O, C, and S elements. Structural analysis showed that no changes were detected after the electrode material preparation. The electrochemical study of the electrodes in 2 M  $\text{ZnSO}_4/0.1 \text{ M MnSO}_4$  aqueous electrolyte showed that pristine  $\delta\text{-MnO}_2$  electrodes were unstable due to manganese dissolution and structural collapse, and the addition of a tunnel-type  $\alpha\text{-MnO}_2$  stabilized the electrode. The addition of PEDOT further improved the electrochemical performance of the cathode material ( $360.5 \text{ mAh}\cdot\text{g}^{-1}$  at 0.1 C and  $94 \text{ mAh}\cdot\text{g}^{-1}$  at 5 C). The capacity fading of the DMOP electrode over 900 cycles at 1 C was  $\approx 10\%$ . Based on the XPS spectra and DFT calculations, the stronger binding effect of  $\text{Zn}^{2+}$  was demonstrated for the composite with PEDOT.

The electrodeposition technique has been applied not only to  $\text{MnO}_2$  cathodes but also to oxygen-deficient  $\text{ZnMn}_2\text{O}_4$  (ZMO) to fabricate flexible zinc-ion batteries [94]. It was suggested that the introduction of oxygen vacancies could increase the electrostatic repulsion of  $\text{Zn}^{2+}$  within the lattice and thus should facilitate the diffusion of  $\text{Zn}^{2+}$  ions from ZMO. PEDOT was deposited on the surface of the grains as a protective layer. The cathode material was prepared by a three-step process: electrodeposition of  $\text{ZnMn}_2\text{O}_4$  on the carbon cloth, annealing in the reducing  $\text{H}_2$  atmosphere to extract oxygen anions, and electrodeposition of PEDOT on the composite surface. The structure and morphology of the resulting composite material were investigated by transmission and scanning electron microscopy. The dense material layer was observed after ZMO deposition, and it was maintained after the second deposition process. Based on the XPS results, the enrichment of oxygen vacancies after the reduction by hydrogen was identified. The ratio of manganese

valence states  $\text{Mn}^{2+}:\text{Mn}^{3+}$  was 1:3, so the ratio of oxygen vacancies was 8.6%. Electrochemical tests were performed in 1 M  $\text{ZnSO}_4$  aqueous solution and in gel electrolyte based on polyvinyl alcohol. The oxygen-deficient ZMO@PEDOT composite delivered the specific capacity of  $221 \text{ mAh}\cdot\text{g}^{-1}$  at the low current density ( $0.5 \text{ mA}\cdot\text{cm}^{-2}$ ), while for ZMO without the polymer layer, it was only  $174 \text{ mAh}\cdot\text{g}^{-1}$ , and at the high current density ( $10 \text{ mA}\cdot\text{cm}^{-2}$ ), the capacity of ZMO@PEDOT composite was  $62.5 \text{ mAh}\cdot\text{g}^{-1}$ . It was shown that the main effect on the electrochemical performance was due to the structural disorder caused by oxygen vacancies, while PEDOT had no electroactivity in this composite. The capacity decay for the ZMO@PEDOT electrode material over 300 cycles at  $I = 8 \text{ mA}\cdot\text{cm}^{-2}$  was only 6.2%. The anion-deficient structure was also studied by DFT calculations, and it was found that oxygen-deficient  $\text{ZnMn}_2\text{O}_4$  has lower energy values, leading to facilitated  $\text{Zn}^{2+}$  diffusion kinetics, lower Zn vacancy formation energy, and lower energy barrier of Zn mobility. With the presence of conducting protective PEDOT layer, the remarkable performance is observed, even for flexible battery with lower capacitive properties:  $207 \text{ mAh}\cdot\text{g}^{-1}$  at  $0.5 \text{ mA}\cdot\text{cm}^{-2}$  and 20% of capacity decay over 300 cycles at  $8 \text{ mA}\cdot\text{cm}^{-2}$ .

Chemical oxidation of EDOT monomer in the presence of  $\text{KMnO}_4$  is an alternative route to prepare  $\text{MnO}_2/\text{PEDOT}$  composites, which was applied in [95], where the layered-type  $\text{MnO}_2/\text{PEDOT}$  composite was prepared by the precipitation method at a low temperature. The  $\text{MnO}_2$  nanowires were coated by PEDOT, with some voids between the nanowires. The XRD diffraction patterns confirmed the layered structure of  $\text{MnO}_2$ , and the structure of PEDOT was evaluated by FTIR and Raman spectra. XPS and EDX analyses confirmed the material composition and the uniform distribution of elements in the composite material. The electrochemical properties were investigated in a 2 M  $\text{ZnSO}_4/0.2 \text{ M MnSO}_4$  solution, and it was shown that the PEDOT layer on the  $\text{MnO}_2$  surface prevents manganese dissolution, resulting in superior performance. At the low current density of  $0.2 \text{ A}\cdot\text{g}^{-1}$ , the specific capacity was  $242 \text{ mAh}\cdot\text{g}^{-1}$ , and at  $I = 3.0 \text{ A}\cdot\text{g}^{-1}$ , it was  $121 \text{ mAh}\cdot\text{g}^{-1}$ . The cycling performance of the  $\text{MnO}_2@\text{PEDOT}$  composite at current densities of 1.0 and  $2.0 \text{ A}\cdot\text{g}^{-1}$  was more stable due to the reduced manganese dissolution/deposition process, and the capacity retention over 1000 cycles at  $2.0 \text{ A}\cdot\text{g}^{-1}$  was 85%. It was also observed that the charge-transfer resistance of the  $\text{MnO}_2@\text{PEDOT}$  electrode was much lower than that of the undoped material, which may be related to the enhanced conductivity of the  $\text{MnO}_2/\text{PEDOT}$  composite.

PEDOT-intercalated  $\text{MnO}_2$  (or PEDOT- $\text{MnO}_2$ ) was obtained in [96] by the reaction of  $\text{KMnO}_4$  and  $\text{MnSO}_4$  in the presence of 3,4-ethylenedioxythiophene monomer. In this case,  $\text{KMnO}_4$  oxidized both  $\text{MnSO}_4$  and EDOT monomer. The morphology of the  $\text{MnO}_2$  samples was hydrangea-like, with a tendency to form separated layers. The XRD diffraction peaks of the samples were indexed to a layered-type  $\text{MnO}_2$  without the crystal lattice changes after PEDOT intercalation. However, HR-TEM measurements showed that the interlayer distance increased from 0.68 nm (for pristine  $\text{MnO}_2$ ) to 0.73 nm (for PEDOT- $\text{MnO}_2$ ), indicating that PEDOT was inserted into the lattice. The specific surface area of the composite grains was relatively low ( $72.5 \text{ m}^2\cdot\text{g}^{-1}$ ) due to the introduction of PEDOT, which reduced the grain size. The rate capability and cycling stability were evaluated in an aqueous solution of 2 M  $\text{ZnSO}_4/0.2 \text{ M MnSO}_4$ . The specific capacity of this composite material decreased from  $300 \text{ mAh}\cdot\text{g}^{-1}$  at  $0.2 \text{ A}\cdot\text{g}^{-1}$  to  $122 \text{ mAh}\cdot\text{g}^{-1}$  at  $2.0 \text{ A}\cdot\text{g}^{-1}$ , but it was fully recovered when low currents were applied after high currents. During continuous cycling at  $2 \text{ A}\cdot\text{g}^{-1}$ , no capacity decay was observed for the first 20 cycles, then insignificant capacity decay and gradual increase were observed for 1200 cycles, and then negligible capacity decay was observed for the last 300 cycles, with excellent coulombic efficiency. The intercalation of PEDOT expands the interlayer spacing of  $\text{MnO}_2$ , which improves the diffusion kinetics of the material, resulting in a more stable and enhanced electrochemical performance.

The simplest way to modify electrodes with PEDOT is to drop-cast PEDOT:PSS onto the material surface or to add PEDOT:PSS or as-synthesized PEDOT to the electrode slurry [97–99]. The first method was applied in [98] to develop binder-free  $\text{MnO}_2$ -PEDOT:PSS electrode material on the vertical graphene. Vertical graphene was obtained on

the carbon fiber surface by plasma-enhanced chemical vapor deposition, then  $\text{MnO}_2$  was obtained hydrothermally on the graphene substrate, and finally PEDOT:PSS dispersion was cast on the material surface, followed by vacuum drying. As observed from HR-TEM images and XRD patterns, the initial graphene substrate had a highly porous structure, and after  $\text{MnO}_2$  synthesis, the pores were occupied by  $\alpha\text{-MnO}_2$  particles, resulting in a 3D conducting structure coated with PEDOT:PSS. The specific capacities of the composite in a 1 M  $\text{ZnSO}_4/0.1$  M  $\text{MnSO}_4$  aqueous electrolyte were  $367 \text{ mAh}\cdot\text{g}^{-1}$  at  $0.5 \text{ A}\cdot\text{g}^{-1}$  and  $148 \text{ mAh}\cdot\text{g}^{-1}$  at  $6.0 \text{ A}\cdot\text{g}^{-1}$ . The cycling performance of the electrode was good, with a capacity retention of 68% over 1000 cycles at  $I = 5.0 \text{ A}\cdot\text{g}^{-1}$ . These functional properties were related to the electrode composition: the carbon fiber current collector acted as an efficient conductor, the vertical graphene enhanced the charge transfer kinetics of  $\text{MnO}_2$ , and the PEDOT:PSS coating suppressed the dissolution and damage of  $\text{MnO}_2$  during repeated electrical and mechanical cycling.

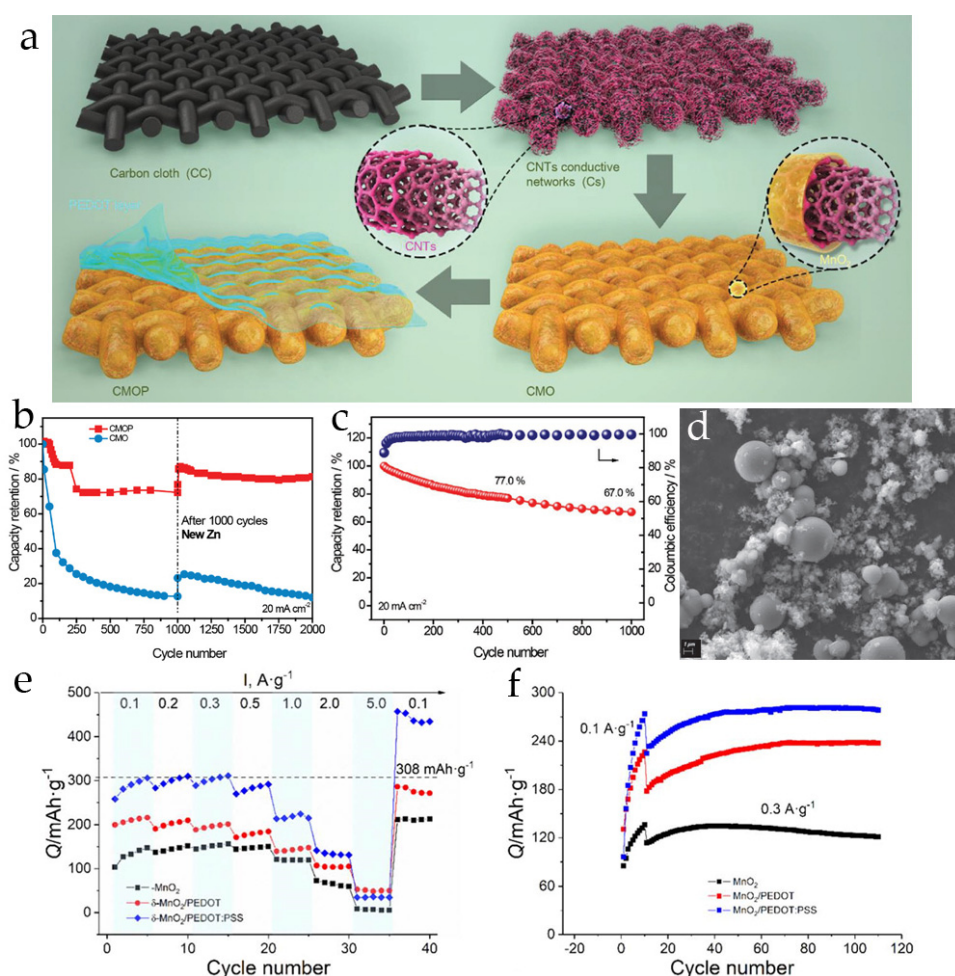


**Figure 11.** (a) Scheme of the CMOP composite cathode synthesis [91]. (b) Cycling stability of CMO and CMOP cathodes (Zn anodes were replaced by fresh ones at the 1001st cycle) [91]. (c) Cycling performance and Coulombic efficiency of the quasi-solid-state Zn-CMOP battery [91]. (d) SEM of PEDOT powder [97]. (e) C-rate capabilities of  $\delta\text{-MnO}_2$ -based electrodes. (f) Cycling stability of  $\delta\text{-MnO}_2$ -based electrodes at  $0.3 \text{ A}\cdot\text{g}^{-1}$  [97].

The preparation of electrode slurry with the addition of chemically polymerized PEDOT or PEDOT:PSS aqueous dispersion was performed by our research group [97]. PEDOT powder (Figure 11d) was obtained via the polymerization of EDOT in the presence of  $\text{FeCl}_3$ , and PEDOT:PSS was used as the coating for hydrothermally synthesized  $\text{MnO}_2$  powder. Both PEDOT-containing electrode materials had a smoother and denser surface than the



pristine MnO<sub>2</sub>-based cathode. The crystalline phase determined from XRD patterns corresponded to the layered-type δ-MnO<sub>2</sub>. The electrochemical tests of δ-MnO<sub>2</sub>/PEDOT and δ-MnO<sub>2</sub>/PEDOT:PSS in a 2 M ZnSO<sub>4</sub>/0.1 M MnSO<sub>4</sub> aqueous electrolyte are shown in Figure 11e,f. It is clearly seen that MnO<sub>2</sub>/PEDOT:PSS electrodes had the best electrochemical performance (298 mAh·g<sup>-1</sup> at I = 0.1 A·g<sup>-1</sup>), with a gradual capacity increase at low current densities, due to MnO<sub>x</sub> electrodeposition on the cathode surface. The cycling stability evaluated at 0.3 A·g<sup>-1</sup> was excellent, with a capacity retention of 99% per maximum value (278 mAh·g<sup>-1</sup>). The improvement of the electrochemical properties of MnO<sub>2</sub> cathodes with conducting polymers can be explained by the increase of both electronic and ionic conductivity of the electrode material due to more conductive media between electroactive grains. In addition, the PEDOT:PSS layer on the electrode surface supports the mechanical integrity and prevents the manganese dissolution during charge/discharge processes.

In conclusion, the introduction of a conducting polymer has a great impact on improving the electrochemical performance of MnO<sub>2</sub>-based cathodes for AZIBs. The above results on the electrochemical properties of the polymer-modified materials are shown in Table 2. The conducting polymer coating improves the mechanical integrity of the composite electrodes, and they are able to further enhance conductivity and buffer shrinkage/expansion during charge/discharge. Protecting the MnO<sub>2</sub> grains from direct contact with the aqueous electrolyte also plays a role in suppressing interfacial side reactions and preventing cathode dissolution.

**Table 2.** Electrochemical performance of selected MnO<sub>2</sub>-based composites with conducting polymers as cathodes in AZIBs.

Material	Synthesis Method	Morphology	Electrolyte	Specific Capacity, mAh g <sup>-1</sup> (Current Density, A·g <sup>-1</sup> )	Capacity Retention, (Number of Cycles and Current, A·g <sup>-1</sup> )	Ref.
δ-MnO <sub>2</sub> @polyaniline	gas/liquid interface reaction	mesoporous nanohybrids	2 M ZnSO <sub>4</sub> + 0.2 M MnSO <sub>4</sub>	313 (0.1) 145 (1) 88 (3)	~100% (500, 0.5)	[65]
Polyaniline-intercalated δ-MnO <sub>2</sub>	one-step inorganic/organic interface reaction	nanolayers with spongiform structure	2 M ZnSO <sub>4</sub> + 0.1 M MnSO <sub>4</sub>	298 (0.05) 280 (0.2) 110 (3)	90% (200, 0.2) 40% (5000, 2)	[66]
Polyaniline-coated β-MnO <sub>2</sub> /rGO	MnO <sub>2</sub> ball-milling + hydrothermal process with rGO (160 °C) + in situ polymerization	aerogel-supported	2 M ZnSO <sub>4</sub>	241.1 (0.1) 111.7 (1)	82.7% (600, 1)	[67]
PANI-δ-MnO <sub>2</sub> /CC	hydrothermal method (150 °C) + in situ polymerization	nanosheets	2 M ZnSO <sub>4</sub> + 0.1 M MnSO <sub>4</sub>	286 (0.5) 233 (2) 177 (4)	96.9% (9000, 4)	[68]
α-MnO <sub>2</sub> @PANI	hydrothermal process (160 °C) + in situ interfacial polymerization	core-shell	2 M ZnSO <sub>4</sub> + 0.1 M MnSO <sub>4</sub>	342 (0.2) 100 (3)	82% (2000, 2)	[69]
α-MnO <sub>2</sub> /PPy	hydrothermal process (160 °C) + in situ polymerization	nanorods	2 M ZnSO <sub>4</sub> + 0.1 M MnSO <sub>4</sub>	256 (0.1) 104 (1)	100% (500, 1) 100% (50, 0.1)	[78]
β-MnO <sub>2</sub> /PPy	one-step hydrothermal process (120 °C)	micro-spherical structure of nanowires and clusters of nanorods	2 M ZnSO <sub>4</sub> + 0.1 M MnSO <sub>4</sub>	215.4 (0.1) 214.1 (0.2) 171.5 (0.5) 69.9 (1.5)	100% (160, 0.2)	[79]
CNT/α-MnO <sub>2</sub> -PPy	in situ reactive self-assembly and following vacuum filtration	core-shell structure and rod-shaped morphology	2 M ZnSO <sub>4</sub> + 0.1 M MnSO <sub>4</sub>	253.9 (0.3) 83.3 (2)	87.4% (1000, 1) 75.5% (200, 0.3)	[81]
α-MnO <sub>2</sub> /rGO-PPy	hydrothermal process (140 °C) + in situ polymerization	nanowires wrapped by PPy	3 M Zn(CF <sub>3</sub> SO <sub>3</sub> ) <sub>2</sub>	438.3 (0.1) 248.8 (0.5)	~85.9% (100, 0.5)	[82]

Table 2. Cont.

Material	Synthesis Method	Morphology	Electrolyte	Specific Capacity, mAh g <sup>-1</sup> (Current Density, A·g <sup>-1</sup> )	Capacity Retention, (Number of Cycles and Current, A·g <sup>-1</sup> )	Ref.
Mn <sub>2</sub> O <sub>3</sub> /α-MnO <sub>2</sub> @PPy	molten salt method + self-initiated polymerization	nanobelts and nanoparticles	2 M ZnSO <sub>4</sub> + 0.2 M MnSO <sub>4</sub>	289.9 (0.2) 252.6 (1) 199.8 (3)	~100% (1000, 3) 96.7% (1000, 1)	[83]
Fe-doped α-MnO <sub>2</sub> coated by PPy	chemical precipitation method + in situ polymerization	nanoparticles	2 M ZnSO <sub>4</sub> + 0.1 M MnSO <sub>4</sub>	270 (0.1) 164 (0.4) 73 (1)	99.6% (100, 0.1)	[84]
α-MnO <sub>2</sub> /PPy@SS	electrodeposition	nanocrystallites	1 M ZnSO <sub>4</sub> + 0.1 M MnSO <sub>4</sub>	143.2 (0.308) 102.2 (0.924) 86.8 (1.54)	74.2% (850, 1.54)	[85]
MnO <sub>2</sub> @PEDOT	electrodeposition	nanosheets	2 M ZnCl <sub>2</sub> + 0.4 M MnSO <sub>4</sub>	366.6 (0.74) 143 (7.43)	83.7% (300, 1.11)	[90]
PEDOT@Co-MnO <sub>2</sub>	low-temperature hydrothermal process + electrochemical polymerization	nanoflakes	2 M ZnSO <sub>4</sub>	298.9 (1)	92.3% (1000, 5.0)	[92]
δ-MnO <sub>2</sub> /α-MnO <sub>2</sub> /PEDOT	decomposition (δ-MnO <sub>2</sub> ) + hydrothermal process (150 °C, α-MnO <sub>2</sub> ) + electrodeposition (PEDOT)	nanowires of δ-MnO <sub>2</sub> and nanoflakes of α-MnO <sub>2</sub>	2 M ZnSO <sub>4</sub> + 0.1 M MnSO <sub>4</sub>	360.5 (0.031) 174.5 (0.308) 94 (1.54)	78% (860, 0.308)	[93]
δ-MnO <sub>2</sub> @PEDOT	redox reaction	nanowires	2 M ZnSO <sub>4</sub> + 0.2 M MnSO <sub>4</sub>	242 (0.2) 133 (1) 120.7 (2)	85.1% (1000, 2)	[95]
VG-α-MnO <sub>2</sub> coated with PEDOT:PSS	hydrothermal process (150 °C)	MnO <sub>2</sub> nanoparticles on VG nanosheets with 3D porous structure	1 M ZnSO <sub>4</sub> + 0.1 M MnSO <sub>4</sub>	367.4 (0.5) 280.5 (1) 148.2 (6)	73.7% (1000, 5)	[98]
K <sub>0.46</sub> Mn <sub>2</sub> O <sub>4</sub> ·1.55H <sub>2</sub> O (δ-MnO <sub>2</sub> )/PEDOT:PSS	hydrothermal method (160 °C) + mechanical mixing with PEDOT:PSS	nanoflowers	2 M ZnSO <sub>4</sub> + 0.1 M MnSO <sub>4</sub>	380 (0.3) 243 (1) 40 (5)	100% (120, 0.3)	[97]

#### 4. On the Charge–Discharge Mechanism in Rechargeable Zn//MnO<sub>2</sub> Batteries

Since the first appearance of rechargeable Zn/MnO<sub>2</sub> batteries [8,100], one of the most important issues of these cells has been the mechanism of electrochemical reaction in mildly acidic aqueous electrolyte. The presence of water molecules and Mn<sup>2+</sup> ions, along with the presence of Zn<sup>2+</sup>, in the electrolyte solutions complicates a better understanding of the reactions that occurs.

The basic charge–discharge mechanism of the MnO<sub>2</sub> and the transfer (such as intercalation) of Zn<sup>2+</sup> ions into the manganese oxide structure are still controversial. So far, four energy storage mechanisms have been proposed (Figure 12) [101,102]:

- (i) Reversible (de)intercalation of Zn<sup>2+</sup> ions,
- (ii) Reversible (de)intercalation of H<sup>+</sup>,
- (iii) Co-(de)intercalation of Zn<sup>2+</sup> and H<sup>+</sup>,
- (iv) Electrolytic deposition/dissolution of MnO<sub>2</sub>.

In addition, it is worth mentioning that the zinc hydroxide sulfate Zn<sub>4</sub>(OH)<sub>6</sub>SO<sub>4</sub>·nH<sub>2</sub>O (ZHS) phase has been found in many works as a by-product formed on the cathode surface during discharge. This chemical precipitation of ZHS occurs due to the local increase in pH near the electrode surface upon the insertion of H<sup>+</sup> into MnO<sub>2</sub>. The ZHS plays a dual role, (a) serving as a passivation layer to inhibit deep dissolution of MnO<sub>2</sub> during discharge and (b) promoting the electrochemical deposition kinetics of active MnO<sub>2</sub> during charging.

In this section, recent observations on the mechanisms of the charge–discharge processes in pure MnO<sub>2</sub> and metal-ion-doped and polymer-modified MnO<sub>2</sub> cathode materials are discussed.

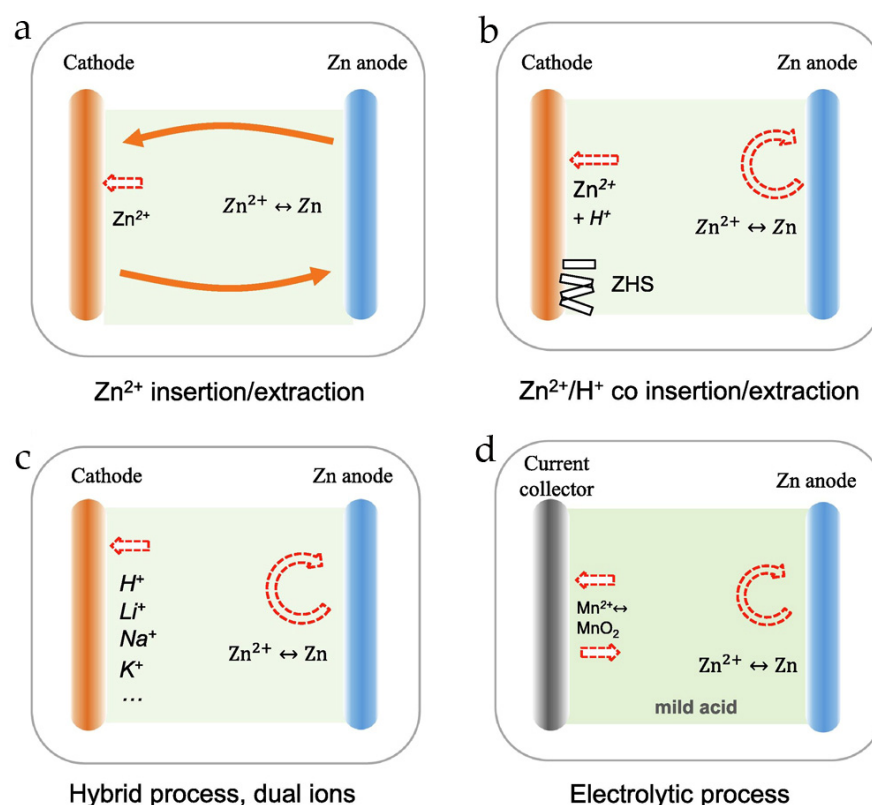


**Figure 12.** A general classification of working mechanisms of MnO<sub>2</sub>-based AZIBs: (a) Zn<sup>2+</sup> insertion/extraction, (b) Zn<sup>2+</sup>/H<sup>+</sup> (co)insertion/extraction, (c) hybrid process, and (d) electrolytic deposition/dissolution of MnO<sub>2</sub> [101].

Reversible insertion/extraction of Zn<sup>2+</sup> ions has been proposed for zinc-ion batteries, as well as for conventional metal-ion batteries, such as lithium-ion or sodium-ion batteries, where reversible intercalation and deintercalation of Li<sup>+</sup> or Na<sup>+</sup> is the only way to store charge. For example, it was shown by ex situ XRD for K-pre-intercalated MnO<sub>2</sub> that the main diffraction peak of the (0,0,3) plane formed reversibly during charging and disappeared during discharging, while the peak corresponding to the (0,0,6) plane shifted to the low-angle region during discharging, which can be associated with reversible Zn<sup>2+</sup> intercalation into the  $\delta$ -MnO<sub>2</sub> lattice [28]. Similar results were obtained by EDX method and ex situ XRD and XPS measurements for a ternary Fe/ $\alpha$ -MnO<sub>2</sub>@PPy composite, where the new phase of ZnMn<sub>2</sub>O<sub>4</sub> was formed or disappeared during the electrochemical process [84]. For Al-doped MnO<sub>2</sub> cathode material, this mechanism was also observed and confirmed by in situ Raman spectroscopy (the phase transition is shown in Figure 13a) [24]. Nevertheless, the mechanism involving only Zn<sup>2+</sup> insertion [16,24,25,28,84] is now considered not plausible due to many novel experimental results, as shown below.

The only insertion/extraction mechanism of H<sup>+</sup> has also been established in a number of works [20,103–106]. Due to the intercalation of H<sup>+</sup> ions during the electrochemical reaction, the pH value of the electrolyte solution has a decisive influence on the mechanism of the processes and the resulting electrochemical properties. In different cycles, the reduction and oxidation peaks shifted to more positive potentials with the decreasing of the pH. The pH value influenced the formation of ZHS, Mn<sup>2+</sup> oxidation, and Mn<sup>3+</sup> disproportionation processes. A detailed study of the pH changes during the cycling process [20,103] showed that the local pH changed from 4.3 to 5.2 because increasing the pH up to 5.6 led to an oxygen evolution reaction (OER), which may be a competitive process at high voltage values. Several strategies could be used to prevent OER, such as abruptly cutting the potential at E = 1.7 V, increasing the acidity of the electrolyte, or using the electrodes with high mass loading. In operando pH measurements in different

electrolytes (0.9 mM H<sub>2</sub>SO<sub>4</sub>, 0.5 M MnSO<sub>4</sub>, 2 M ZnSO<sub>4</sub>, and mixed Zn-Mn electrolytes) showed a strong dependence of the pH on the electrolyte composition. In 0.9 mM H<sub>2</sub>SO<sub>4</sub>, the pH increased sharply up to 8.0, driven by MnO<sub>2</sub> dissolution during the discharge process, and then returned to the initial value. For 2 M ZnSO<sub>4</sub>, insignificant pH changes were observed after the first discharge, while for MnSO<sub>4</sub> and mixed electrolyte, the pH value fluctuated. In the absence of ZnSO<sub>4</sub> in the electrolyte solution, the shape of the CV curve changed dramatically, and only one reduction peak was observed at E = 1.10 V (in 0.9 mM H<sub>2</sub>SO<sub>4</sub>) or E = 1.17 V (in 0.5 M MnSO<sub>4</sub>) vs. Zn/Zn<sup>2+</sup> [103]. In summary, the following reaction mechanisms could be proposed by studying the pH behavior: H<sup>+</sup> (de)intercalation with a minor influence on the overall charge/discharge capacity, Mn<sup>2+</sup> deposition/MnO<sub>2</sub> dissolution at the positive electrode surface as the main source of the capacity, ZHS precipitation/dissolution as a consequence of local pH decreases/increases, and OER/HER processes (Figure 13b). Zn<sup>2+</sup> intercalation was not discussed in this version of the mechanism [20].

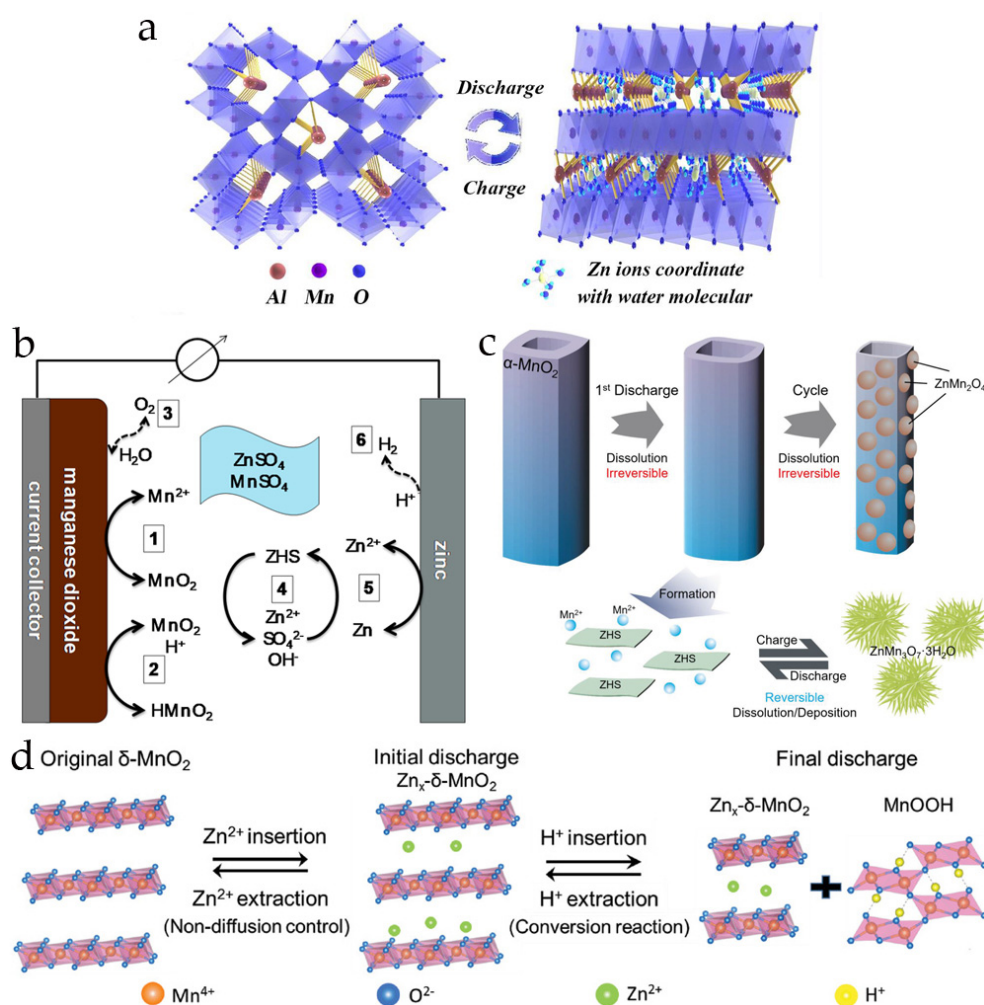


**Figure 13.** (a) Scheme of phase transitions in Al-doped MnO<sub>2</sub> material with Zn<sup>2+</sup> ions reversible intercalation [24]. (b) Summary of the chemical processes in the AZIB with a Zn/ZnSO<sub>4</sub>+MnSO<sub>4</sub>/MnO<sub>2</sub> cell: (1) Mn<sup>2+</sup> deposition/MnO<sub>2</sub> dissolution, (2) H<sup>+</sup> (de-)intercalation, (3) OER/ORR, (4) ZHS precipitation/dissolution, (5) zinc plating/stripping, and (6) HER [103]. (c) Schematic illustration of the reaction mechanism of α-MnO<sub>2</sub> in AZIBs with the dissolution/deposition mechanism [107]. (d) Joint non-diffusion controlled Zn<sup>2+</sup> intercalation and H<sup>+</sup> conversion reaction mechanism in δ-MnO<sub>2</sub> [108].

Another mechanism (iii) of electrochemical reaction discussed in the literature is the co-insertion of Zn<sup>2+</sup> and H<sup>+</sup> due to the small size of H<sup>+</sup> ions. A typical scheme of this mech-

anism is shown in Figure 13d. As was shown by ex situ XRD, two main products formed at the end of the discharge were zinc hydroxide sulfate  $Zn_4(OH)_6SO_4 \cdot nH_2O$  (ZHS), which dissolves during the subsequent charging process, and  $MnOOH$  [25,29,43,48,96,108–110]. These discharge products could be associated with the co-insertion of protons and zinc ions into the lattice with partial reduction of the  $MnO_2$  host and local increase of the pH near the electrode surface. It has been shown by ex situ XPS that the valence state of manganese in the fully discharged state is close to  $Mn^{3+}$ , and the presence of  $Zn^{2+}$  ions extracted during charging with  $Mn^{3+}$ - $Mn^{4+}$  redox transition has also been confirmed [48]. Reversible deposition of ZHS with significant lattice expansion due to  $Zn^{2+}$  insertion has been described for layered  $MnO_2$  doped with alkali metal ions [23,36].

Thus, for the first discharge process in pure  $ZnSO_4$  solution, only one peak pair is observed from the cyclic voltammograms, while in mixed 2 M  $ZnSO_4$ /0.5 M  $MnSO_4$ , two peak pairs were detected. In addition, the reversibility of the electrochemical reaction was better in the mixed electrolyte [111]. Ex situ XRD measurements of the electrodes during the discharge process up to 1.4 V showed no significant changes compared to the initial patterns, while after decreasing the voltage to 1.2 and 1.0 V, new phases were observed and attributed to  $Zn_4(OH)_6SO_4 \cdot 5H_2O$ ,  $\alpha$ - $MnOOH$ , and  $Mn_2O_3$  with the presence of zinc in the Mn-containing phase, so that the insertion of  $Zn^{2+}$  and  $H^+$  was detected, and  $H^+$  was intercalated at lower voltages than that of  $Zn^{2+}$ , which contradicts the other reports [66,79,112–114], where the first voltage plateau/peak corresponded to  $H^+$  insertion and the second to  $Zn^{2+}$  intercalation.  $H^+$  intercalation is accompanied by the conversion of  $MnO_2$  to  $MnOOH$  or  $Mn_2O_3$  due to the reduction of Mn to  $MnO_2$ . During the charging process,  $Zn_4(OH)_6SO_4 \cdot 5H_2O$  is dissolved, and  $ZnMn_3O_7 \cdot 3H_2O$  is formed. A detailed analysis showed that  $Zn_4(OH)_6SO_4 \cdot 5H_2O$  reacted with  $Mn^{2+}$  ions to form the  $ZnMn_3O_7 \cdot 3H_2O$  phase, while  $MnOOH$  transformed into  $MnO_2$  during the charging process. Thus, it was shown that three ions ( $H^+$ ,  $Zn^{2+}$ , and  $Mn^{2+}$ ) participate in the electrochemical reaction, and after continuous cycling, many forms of Zn-containing manganese oxides and  $Zn_4(OH)_6SO_4 \cdot 5H_2O$  coexist in the discharged state, and the formation of these phases, except for  $Zn_4(OH)_6SO_4 \cdot 5H_2O$ , is irreversible [111]. Thus, a complete electrochemical mechanism could be presented as a two-step intercalation and conversion mechanism of transformation of  $MnO_2$  to  $MnOOH$  with a further transition to  $Mn_3O_4$  and deposition of ZHS [108,109]. Furthermore, from the analysis of cyclic voltammograms obtained in the scan rate range 0.1–1.0  $mV s^{-1}$ , it was found that  $Zn^{2+}$  intercalation is a non-diffusion controlled process, while intercalation of  $H^+$  led to structural transformations (detected on the ex situ XRD patterns), which is the reason for the conversion process of  $MnO_2$  [108].

The initial  $MnO_2$  crystal lattice affects the electrochemical performance of the electrode materials in mildly acidic mixed electrolyte. In particular,  $\beta$ - $MnO_2$  and  $\delta$ - $MnO_2$  showed longer capacity growth during cycling at 0.1  $A \cdot g^{-1}$  than other used polymorphs ( $\alpha$ -,  $\gamma$ -,  $\epsilon$ -,  $\lambda$ -, and R- $MnO_2$ ) [115]. The structural evolution of  $\beta$ - $MnO_2$  at different current densities (0.1, 0.3, 0.5, and 1.0  $A \cdot g^{-1}$ ) was studied by ex situ XRD. It was shown that the initial crystal phase changed gradually during 50–100 cycles depending on the applied current: the fastest evolution was observed at 0.1  $A \cdot g^{-1}$  and the slowest at 1.0  $A \cdot g^{-1}$ . According to the appearance of the nanosheets (which could also be associated with layered-type ZHS), the initial product of these phase transitions was birnessite. The final product at the end of the long-term cycling was mixed  $ZnMn_2O_4 \cdot Mn_3O_4$  oxide, or  $(Zn,Mn)Mn_2O_4$ , which is an electrochemically inactive phase. These observations were verified for other  $MnO_2$  polymorphs by using acetic acid to buffer the electrolyte acidity, and all results confirmed the formation of inactive spinel [116]. In this process, dual  $Zn^{2+}/H^+$  co-insertion occurs with accompanying distortion of  $Mn^{3+}$ , followed by its dissolution. The main cause of cathode degradation is  $MnO_2$  dissolution. An XRD analysis of ramsdellite-type  $MnO_2$  showed no metastable phase as the birnessite was formed, and 95% of the initial capacity was retained. Ex situ XRD patterns of R- $MnO_2$  showed the same diffraction peaks after the 1st, 100th, and 300th cycles, indicating that  $Mn^{2+}$  dissolution/deposition had no effect on this type of material [115]. In addition, an extremely low degree of dissolution of

ramsdellite was observed. As for other  $\text{MnO}_2$  polymorphs, the new phase of ZHS was observed by ex situ XRD during the discharge process of R- $\text{MnO}_2$ .

In several reports, no or weak reversible intercalation of  $\text{Zn}^{2+}$  occurred, while irreversible insertion of  $\text{Zn}^{2+}$  with structural transformations of  $\text{MnO}_2$  cathodes was observed [104,105]. Such works are classified as a (iv) type of mechanism, electrolytic deposition/dissolution of  $\text{MnO}_2$  (Figure 13c). The initial  $\beta$ - $\text{MnO}_2$  phase was destroyed during the discharge in 2 M  $\text{ZnSO}_4$  solution, and ZHS layers (with different amounts of crystallization water) formed on the electrode surface. During the first charge, no peaks of  $\beta$ - $\text{MnO}_2$  were observed in the diffraction patterns. After five charge/discharge cycles, three valence states ( $\text{Mn}^{2+}$ ,  $\text{Mn}^{3+}$ , and  $\text{Mn}^{4+}$ ) were observed in the XPS spectra of manganese in the ratio of 41.7%, 36.5%, and 21.8%, respectively. In addition, the  $\text{Zn}^{2+}$  signals disappeared after acid treatment, indicating that the  $\text{Zn}^{2+}$  intercalation mechanism was not implemented [104]. The presence of  $\text{Mn}^{3+}$  in the resulting compound allowed the authors [104] to conclude that  $\text{HMnO}_2$  was formed during  $\text{H}^+$  insertion without any changes in the crystalline structure. The formation of ZHS at  $E = 1.35$  V was demonstrated by the chelation of Zn by a sodium trimetaphosphate additive and the absence of the corresponding peak on the CV curve. Thus, at low number of cycles, no zinc was inserted into the  $\text{MnO}_2$  lattice. After 100 cycles, 0.26% of Zn was present after acidic treatment of the sample, and the Zn–O–Mn bond was observed in the O 1s spectra. A detailed ex situ XRD analysis showed that the highly crystalline material became amorphous, and several peaks consistent with the  $\text{ZnMn}_2\text{O}_4$  phase appeared, but they formed during the charging of the cell rather than during discharging due to alkalization of the electrolyte solution after five cycles. It should be noted that  $\text{ZnMn}_2\text{O}_4$  is not an electroactive compound here, and its presence hinders the electroactivity of the initial cathode materials. The TEM characterization of the cathode after the first discharge cycle showed that ZHS formed on the cathode surface, and after the first charge,  $\text{MnO}_2$  with an excess of Zn and the valence state of Mn close to +3.3 (denoted as  $\text{Zn}_{0.33}\text{MnO}_2$ ) were formed [105]. The formation of this Zn-containing phase is not due to the intercalation of the  $\text{Zn}^{2+}$  ions into  $\text{MnO}_2$  but the consequence of several oxidation processes with the trapping of  $\text{Zn}^{2+}$  ions, as was also observed from XRD patterns [97]. The formation of ZHS occurred even in the absence of the cathode material on the substrate, but in the presence of  $\text{Mn}^{2+}$ , the  $\text{Mn}^{2+}$  oxidation potential decreased from +1.9 V to +1.55 V. The studies by ex situ XRD in operando Raman spectroscopy and SEM showed two parallel reactions: a slow decrease of the intensity of the peaks in the Raman spectra of  $\text{MnO}_2$ ; and, at  $E < 1.3$  V, a decrease of the peak intensity and the appearance of ZHS. During charging, almost the complete dissolution of ZHS and formation of the Zn-containing phase were observed. Thus, ZHS is an agent that hinders the overall electrochemical reaction. ZHS can also contain a significant amount of the phase of Mn-doped ZHS [117], while this compound is not formed by intercalation, but by conversion, since there is no phase change to the layered one (detected in the XRD data), and the manganese dissolves at low potentials. In addition, the pH has a crucial effect on the mechanism, as pH changes occur simultaneously with the dissolution and precipitation of  $\text{MnO}_2$  [118]. In addition, the constant pH value throughout the volume of the electrolyte affects the concentration of  $\text{Zn}^{2+}$  complexes, which are an intermediate in the formation of ZHS, as evidenced by the significant increase in the molar mass of transferred particles calculated from EQCM measurements at low potentials (1.3–1.0 V) [105,119].

The same observations can be applied to the dissolution/deposition mechanism of  $\text{MnO}_2$  transformations [106,107,120]. In this case, the deposition of ZHS is associated with almost complete dissolution of the initial cathode material due to intercalation of  $\text{H}^+$  and subsequent conversion reaction with  $\text{MnO}_2$ . A nanoscale TEM analysis of a Zn// $\alpha$ - $\text{MnO}_2$  battery showed that the dissolution of  $\text{Mn}^{2+}$  releases 4  $\text{OH}^-$ , leading to the formation of the ZHS coating on the initial cathode material. During the charging process, the deposition of  $\text{MnO}_2$  and the trapping of  $\text{Zn}^{2+}$  ions from the electrolyte solution occurred, resulting in the formation of inactive Zn-containing manganese oxide, as described in [120]. The dissolution of manganese was also observed by the gradual disappearance of  $\text{MnOOH}$

during the continuous cycling of the electrode with the single crystalline phase, which was indexed as ZHS [48].

For comparison, in the absence of water in the composition of the electrolyte for a non-aqueous rechargeable Zn metal battery in organic electrolytes, the mechanism changes dramatically. Moreover,  $\delta$ -MnO<sub>2</sub> tested in Zn(TFSI)<sub>2</sub>-acetonitrile electrolyte solution showed a different shape of charge/discharge profiles with an average cell potential of  $\approx 1.37$  V [121]. It was shown that the highest specific capacity at low current ( $123 \text{ mAh}\cdot\text{g}^{-1}$  at 0.04 C) corresponds to approximately 0.2 mol of Zn<sup>2+</sup> ions inserted per mole of MnO<sub>2</sub>. During continuous cycling, the capacity first increased with the increasing electrode/electrolyte interface due to cathode wetting, and then the dissolution of Mn<sup>2+</sup> and K<sup>+</sup> led to a sharp capacity fade. The reversible insertion and extraction of Zn<sup>2+</sup> ions during cycling were demonstrated by ex situ XRD measurements of the electrodes: an additional peak of ZnO and the shift of the (111) peak were observed. The valence state of manganese in pristine MnO<sub>2</sub> from XANES data was +3.6, and during cycling, it changed to +3.2 for the discharged and +3.8 for the charged states. Thus, in nonaqueous cells, the mechanism of the electrochemical reaction was described as reversible structural transformations between layered-type  $\delta$ -MnO<sub>2</sub> and spinel-type Zn-containing phase ZnMn<sub>2</sub>O<sub>4</sub>, without the influence of protons on the properties and mechanism of cathode operation.

In summary, we can conclude that the insertion of H<sup>+</sup> with small amounts of Zn<sup>2+</sup> (iii) and the electrolytic dissolution/deposition mechanism of MnO<sub>2</sub> cathode (iv) are not contradictory but complementary ways of electrochemical reaction in aqueous media. Many reports confirmed that the trapping of Zn<sup>2+</sup> and the formation of electrochemically inactive Zn-containing manganese oxide led to capacity fading, while the formation of complex Zn<sub>4</sub>(OH)<sub>6</sub>SO<sub>4</sub>·nH<sub>2</sub>O salt during discharge is the pH-controlled process caused by Mn<sup>3+</sup> distortion and H<sup>+</sup> intercalation during the discharge process.

The structural and interfacial design of MnO<sub>2</sub> cathodes, metal ion doping, and introduction of conducting polymers lead to the implementation of mechanism (iii), the co-(de)intercalation of Zn<sup>2+</sup> and H<sup>+</sup>. It should be noted that the structural transformations and the formation of Zn<sub>x</sub>MnO<sub>2</sub> after the first discharge are confirmed by ex situ XRD studies. Ex situ XRD studies of PEDOT-coated MnO<sub>2</sub> showed highly reversible formation of MnOOH and ZnMn<sub>2</sub>O<sub>4</sub> during discharge, consistent with the dual insertion mechanism [95]. At the same time, there is often no clear evidence for the co-intercalation of H<sup>+</sup> ions, but only indirect evidence, namely the formation of ZHS and a pH change of the electrolyte.

## 5. Summary and Outlook

The recent studies have shown that the doping of MnO<sub>2</sub> with metal ions and the synthesis of MnO<sub>2</sub>-conducting polymer composites are the effective ways to improve the electrochemical performance of Zn//MnO<sub>2</sub> rechargeable batteries.

In the case of doped MnO<sub>2</sub> materials, the stabilization of the host lattice and the expansion of the interlayer spaces facilitate the diffusion of intercalated particles, thus significantly improving the rate performance. The presence of novel chemical bonds (such as Al-O) reduces the structural transformations of MnO<sub>2</sub> during cycling and increases cycling stability. Conducting polymers significantly improve the ionic and electronic conductivity of the composite materials, which also results in superior cell performance. The use of conducting polymers is more advantageous due to the absence of toxic or heavy metals and the high number of synthetic routes. On the other hand, doping makes it possible to manipulate the crystal lattice and create materials with defects that significantly improve their own conductivity. Excellent and comparable effects in electrochemical performance have been achieved by using both strategies.

These two strategies can be combined to fabricate the composites of metal-ion-doped MnO<sub>2</sub> with the conducting polymer, as shown by the example of Fe/ $\alpha$ -MnO<sub>2</sub>@PPy and PEDOT@Co-MnO<sub>2</sub> composites, demonstrating the improved performance [84,92]. In both cases, the synergistic effect of the application of conducting polymer coating and dopants

increased the rate and cycling performance due to the improved conductivity of the ternary composites due to the increased interlayer spacing, while the conducting polymer stabilized the surface and suppressed manganese dissolution. Thus, the combination of these two approaches to improve the properties of MnO<sub>2</sub>-based cathodes is interesting for further investigation in the field of aqueous zinc batteries.

As a detailed analysis of the cited works shows, the conclusions on the mechanism of charge–discharge processes in manganese oxide-based materials are still contradictory and require further in-depth mechanistic analysis.

We believe that this review will shed more light on the novel strategies toward the practical application of Zn//MnO<sub>2</sub> batteries, which could replace lead-acid and lithium-ion batteries in stationary energy storage. In addition, the understanding of the electrochemical reaction mechanism could be useful to develop other ways to improve the stability and cycle life of Zn//MnO<sub>2</sub> batteries.

**Author Contributions:** Conceptualization, M.A.K. and V.V.K.; writing—original draft preparation, M.A.K. and F.S.V.; writing—review and editing, E.G.T., V.V.K., and S.N.E.; visualization, E.G.T. and M.A.K. All authors have read and agreed to the published version of the manuscript.

**Funding:** This research received no external funding.

**Data Availability Statement:** Data sharing not applicable.

**Conflicts of Interest:** The authors declare no conflict of interest.

## References

1. Bai, Y.; Muralidharan, N.; Sun, Y.-K.; Passerini, S.; Stanley Whittingham, M.; Belharouak, I. Energy and Environmental Aspects in Recycling Lithium-Ion Batteries: Concept of Battery Identity Global Passport. *Mater. Today* **2020**, *41*, 304–315. [\[CrossRef\]](#)
2. Baum, Z.J.; Bird, R.E.; Yu, X.; Ma, J. Lithium-Ion Battery Recycling—Overview of Techniques and Trends. *ACS Energy Lett.* **2022**, *7*, 712–719. [\[CrossRef\]](#)
3. Tang, B.; Shan, L.; Liang, S.; Zhou, J. Issues and Opportunities Facing Aqueous Zinc-Ion Batteries. *Energy Environ. Sci.* **2019**, *12*, 3288–3304. [\[CrossRef\]](#)
4. Shi, Y.; Chen, Y.; Shi, L.; Wang, K.; Wang, B.; Li, L.; Ma, Y.; Li, Y.; Sun, Z.; Ali, W.; et al. An Overview and Future Perspectives of Rechargeable Zinc Batteries. *Small* **2020**, *16*, 2000730. [\[CrossRef\]](#)
5. Zhang, T.; Tang, Y.; Guo, S.; Cao, X.; Pan, A.; Fang, G.; Zhou, J.; Liang, S. Fundamentals and Perspectives in Developing Zinc-Ion Battery Electrolytes: A Comprehensive Review. *Energy Environ. Sci.* **2020**, *13*, 4625–4665. [\[CrossRef\]](#)
6. Zhang, X.; Wang, L.; Fu, H. Recent Advances in Rechargeable Zn-Based Batteries. *J. Power Sources* **2021**, *493*, 229677. [\[CrossRef\]](#)
7. Borchers, N.; Clark, S.; Horstmann, B.; Jayasayee, K.; Juel, M.; Stevens, P. Innovative Zinc-Based Batteries. *J. Power Sources* **2021**, *484*, 229309. [\[CrossRef\]](#)
8. Xu, C.; Li, B.; Du, H.; Kang, F. Energetic Zinc Ion Chemistry: The Rechargeable Zinc Ion Battery. *Angew. Chemie-Int. Ed.* **2012**, *51*, 933–935. [\[CrossRef\]](#)
9. Chen, L.; An, Q.; Mai, L. Recent Advances and Prospects of Cathode Materials for Rechargeable Aqueous Zinc-Ion Batteries. *Adv. Mater. Interfaces* **2019**, *6*, 1900387. [\[CrossRef\]](#)
10. Liu, X.; Yi, J.; Wu, K.; Jiang, Y.; Liu, Y.; Zhao, B.; Li, W.; Zhang, J. Rechargeable Zn–MnO<sub>2</sub> Batteries: Advances, Challenges and Perspectives. *Nanotechnology* **2020**, *31*, 122001. [\[CrossRef\]](#) [\[PubMed\]](#)
11. Bensalah, N.; De Luna, Y. Recent Progress in Layered Manganese and Vanadium Oxide Cathodes for Zn-Ion Batteries. *Energy Technol.* **2021**, *9*, 2100011. [\[CrossRef\]](#)
12. Liang, R.; Fu, J.; Deng, Y.P.; Pei, Y.; Zhang, M.; Yu, A.; Chen, Z. Parasitic Electrodeposition in Zn–MnO<sub>2</sub> Batteries and Its Suppression for Prolonged Cyclability. *Energy Storage Mater.* **2021**, *36*, 478–484. [\[CrossRef\]](#)
13. Liu, Z.; Qin, L.; Lu, B.; Wu, X.; Liang, S.; Zhou, J. Issues and Opportunities Facing Aqueous Mn<sup>2+</sup>/MnO<sub>2</sub>-based Batteries. *ChemSusChem* **2022**, *15*, e202200348. [\[CrossRef\]](#) [\[PubMed\]](#)
14. Yadav, P.; Kumari, N.; Rai, A.K. A Review on Solutions to Overcome the Structural Transformation of Manganese Dioxide-Based Cathodes for Aqueous Rechargeable Zinc Ion Batteries. *J. Power Sources* **2023**, *555*, 232385. [\[CrossRef\]](#)
15. Zhang, Z.; Li, W.; Shen, Y.; Wang, R.; Li, H.; Zhou, M.; Wang, W.; Wang, K.; Jiang, K. Issues and Opportunities of Manganese-Based Materials for Enhanced Zn-Ion Storage Performances. *J. Energy Storage* **2022**, *45*, 103729. [\[CrossRef\]](#)
16. Soundharajan, V.; Sambandam, B.; Kim, S.S.; Islam, S.; Jo, J.; Kim, S.S.; Mathew, V.; Sun, Y.K.; Kim, J. The Dominant Role of Mn<sup>2+</sup> Additive on the Electrochemical Reaction in ZnMn<sub>2</sub>O<sub>4</sub> Cathode for Aqueous Zinc-Ion Batteries. *Energy Storage Mater.* **2020**, *28*, 407–417. [\[CrossRef\]](#)
17. Qiu, C.; Zhu, X.; Xue, L.; Ni, M.; Zhao, Y.; Liu, B.; Xia, H. The Function of Mn<sup>2+</sup> Additive in Aqueous Electrolyte for Zn/δ-MnO<sub>2</sub> Battery. *Electrochim. Acta* **2020**, *351*, 136445. [\[CrossRef\]](#)



18. Perez-Antolin, D.; Sáez-Bernal, I.; Colina, A.; Ventosa, E. Float-Charging Protocol in Rechargeable Zn–MnO<sub>2</sub> Batteries: Unraveling the Key Role of Mn<sup>2+</sup> Additives in Preventing Spontaneous pH Changes. *Electrochem. Commun.* **2022**, *138*, 107271. [[CrossRef](#)]
19. Lv, H.; Song, Y.; Qin, Z.; Zhang, M.; Yang, D.; Pan, Q.; Wang, Z.; Mu, X.; Meng, J.; Sun, X.; et al. Disproportionation Enabling Reversible MnO<sub>2</sub>/Mn<sup>2+</sup> Transformation in a Mild Aqueous Zn-MnO<sub>2</sub> Hybrid Battery. *Chem. Eng. J.* **2022**, *430*, 133064. [[CrossRef](#)]
20. Bischoff, C.F.; Fitz, O.S.; Burns, J.; Bauer, M.; Gentischer, H.; Birke, K.P.; Henning, H.-M.; Biro, D. Revealing the Local pH Value Changes of Acidic Aqueous Zinc Ion Batteries with a Manganese Dioxide Electrode during Cycling. *J. Electrochem. Soc.* **2020**, *167*, 020545. [[CrossRef](#)]
21. Yong, B.; Ma, D.; Wang, Y.; Mi, H.; He, C.; Zhang, P. Understanding the Design Principles of Advanced Aqueous Zinc-Ion Battery Cathodes: From Transport Kinetics to Structural Engineering, and Future Perspectives. *Adv. Energy Mater.* **2020**, *10*, 2002354. [[CrossRef](#)]
22. Zhang, B.; Chen, J.; Sun, W.; Shao, Y.; Zhang, L.; Zhao, K. Challenges and Perspectives for Doping Strategy for Manganese-Based Zinc-Ion Battery Cathode. *Energies* **2022**, *15*, 4698. [[CrossRef](#)]
23. Xie, Q.; Cheng, G.; Xue, T.; Huang, L.; Chen, S.; Sun, Y.; Sun, M.; Wang, H.; Yu, L. Alkali Ions Pre-Intercalation of δ-MnO<sub>2</sub> Nanosheets for High-Capacity and Stable Zn-Ion Battery. *Mater. Today Energy* **2022**, *24*, 100934. [[CrossRef](#)]
24. Chen, C.; Shi, M.; Zhao, Y.; Yang, C.; Zhao, L.; Yan, C. Al-Intercalated MnO<sub>2</sub> Cathode with Reversible Phase Transition for Aqueous Zn-Ion Batteries. *Chem. Eng. J.* **2021**, *422*, 130375. [[CrossRef](#)]
25. Alfaruqi, M.H.; Islam, S.; Mathew, V.; Song, J.; Kim, S.; Tung, D.P.; Jo, J.; Kim, S.; Baboo, J.P.; Xiu, Z.; et al. Ambient Redox Synthesis of Vanadium-Doped Manganese Dioxide Nanoparticles and Their Enhanced Zinc Storage Properties. *Appl. Surf. Sci.* **2017**, *404*, 435–442. [[CrossRef](#)]
26. Kataoka, F.; Ishida, T.; Nagita, K.; Kumbhar, V.; Yamabuki, K.; Nakayama, M. Cobalt-Doped Layered MnO<sub>2</sub> Thin Film Electrochemically Grown on Nitrogen-Doped Carbon Cloth for Aqueous Zinc-Ion Batteries. *ACS Appl. Energy Mater.* **2020**, *3*, 4720–4726. [[CrossRef](#)]
27. Ko, W.Y.; Lubis, A.L.; Wang, H.Y.; Wu, T.C.; Lin, S.T.; Lin, K.J. Facile Construction of Zn-Doped Mn<sub>3</sub>O<sub>4</sub>–MnO<sub>2</sub> Vertical Nanosheets for Aqueous Zinc-Ion Battery Cathodes. *ChemElectroChem* **2022**, *9*, e202200750. [[CrossRef](#)]
28. Li, X.; Qu, J.; Xu, J.; Zhang, S.; Wang, X.; Wang, X.; Dai, S. K-Preintercalated MnO<sub>2</sub> Nanosheets as Cathode for High-Performance Zn-Ion Batteries. *J. Electroanal. Chem.* **2021**, *895*, 115529. [[CrossRef](#)]
29. Lin, M.; Shao, F.; Tang, Y.; Lin, H.; Xu, Y.; Jiao, Y.; Chen, J. Layered Co Doped MnO<sub>2</sub> with Abundant Oxygen Defects to Boost Aqueous Zinc-Ion Storage. *J. Colloid Interface Sci.* **2022**, *611*, 662–669. [[CrossRef](#)]
30. Ni, Z.; Liang, X.; Zhao, L.; Zhao, H.; Ge, B.; Li, W. Tin Doping Manganese Dioxide Cathode Materials with the Improved Stability for Aqueous Zinc-Ion Batteries. *Mater. Chem. Phys.* **2022**, *287*, 126238. [[CrossRef](#)]
31. Chen, Q.; Jin, J.; Kou, Z.; Liao, C.; Liu, Z.; Zhou, L.; Wang, J.; Mai, L. Zn<sup>2+</sup> Pre-Intercalation Stabilizes the Tunnel Structure of MnO<sub>2</sub> Nanowires and Enables Zinc-Ion Hybrid Supercapacitor of Battery-Level Energy Density. *Small* **2020**, *16*, 2000091. [[CrossRef](#)] [[PubMed](#)]
32. Ni, Z.; Liang, X.; Zhao, L.; Zhao, H.; Ge, B.; Li, W. MnO<sub>2</sub> Cathode Materials with High Reversible Stability through Li Intercalating for Aqueous Zinc Ion Battery. *Solid State Ionics* **2022**, *386*, 116049. [[CrossRef](#)]
33. Wu, Y.; Wang, M.; Tao, Y.; Zhang, K.; Cai, M.; Ding, Y.; Liu, X.; Hayat, T.; Alsaedi, A.; Dai, S. Electrochemically Derived Graphene-Like Carbon Film as a Superb Substrate for High-Performance Aqueous Zn-Ion Batteries. *Adv. Funct. Mater.* **2020**, *30*, 1907120. [[CrossRef](#)]
34. Lin, M.X.; Shao, F.; Weng, S.; Xiong, S.; Liu, S.; Jiang, S.; Xu, Y.; Jiao, Y.; Chen, J. Boosted Charge Transfer in Oxygen Vacancy-Rich K<sup>+</sup> Birnessite MnO<sub>2</sub> for Water Oxidation and Zinc-Ion Batteries. *Electrochim. Acta* **2021**, *378*, 138147. [[CrossRef](#)]
35. Lv, W.; Meng, J.; Li, Y.; Yang, W.; Tian, Y.; Lyu, X.; Duan, C.; Ma, X.; Wu, Y. Inexpensive and Eco-Friendly Nanostructured Birnessite-Type δ-MnO<sub>2</sub>: A Design Strategy from Oxygen Defect Engineering and K<sup>+</sup> Pre-Intercalation. *Nano Energy* **2022**, *98*, 107274. [[CrossRef](#)]
36. Wang, D.; Zhang, S.; Li, C.; Chen, X.; Wang, W.; Han, Y.; Lin, H.; Shi, Z.; Feng, S. Engineering the Interplanar Spacing of K-Birnessite for Ultra-Long Cycle Zn-Ion Battery through “Hydrothermal Potassium Insertion” Strategy. *Chem. Eng. J.* **2022**, *435*, 134754. [[CrossRef](#)]
37. Liu, G.; Huang, H.; Bi, R.; Xiao, X.; Ma, T.; Zhang, L. K<sup>+</sup> Pre-Intercalated Manganese Dioxide with Enhanced Zn<sup>2+</sup> Diffusion for High Rate and Durable Aqueous Zinc-Ion Batteries. *J. Mater. Chem. A* **2019**, *7*, 20806–20812. [[CrossRef](#)]
38. Tan, J.; Feng, T.; Hu, S.; Liang, Y.; Zhang, S.; Xu, Z.; Zhou, H.; Wu, M. In Situ Synthesis of a Self-Supported MnO<sub>2</sub>-Based Cathode for High-Performance Zinc-Ion Batteries by K<sup>+</sup> Pre-Intercalation. *Appl. Surf. Sci.* **2022**, *604*, 154578. [[CrossRef](#)]
39. Xu, T.H.; Liou, S.; Hou, F.L.; Li, Y.Y. Potassium-Doped Hydrated Manganese Dioxide Nanowires-Carbon Nanotubes on Graphene for High-Performance Rechargeable Zinc-Ion Batteries. *J. Alloys Compd.* **2022**, *913*, 165278. [[CrossRef](#)]
40. Sun, T.; Nian, Q.; Zheng, S.; Shi, J.; Tao, Z. Layered Ca<sub>0.28</sub>MnO<sub>2</sub>·0.5H<sub>2</sub>O as a High Performance Cathode for Aqueous Zinc-Ion Battery. *Small* **2020**, *16*, 2000597. [[CrossRef](#)]
41. Wang, J.; Wang, J.-G.; Liu, H.; Wei, C.; Kang, F. Zinc Ion Stabilized MnO<sub>2</sub> Nanospheres for High Capacity and Long Lifespan Aqueous Zinc-Ion Batteries. *J. Mater. Chem. A* **2019**, *7*, 13727–13735. [[CrossRef](#)]
42. Shi, M.; Zhu, H.; Chen, C.; Jiang, J.; Zhao, L.; Yan, C. Synergistically Coupling of Graphene Quantum Dots with Zn-Intercalated MnO<sub>2</sub> Cathode for High-Performance Aqueous Zn-Ion Batteries. *Int. J. Miner. Metall. Mater.* **2023**, *30*, 25–32. [[CrossRef](#)]

43. Li, Y.; Li, X.; Duan, H.; Xie, S.; Dai, R.; Rong, J.; Kang, F.; Dong, L. Aerogel-Structured MnO<sub>2</sub> Cathode Assembled by Defect-Rich Ultrathin Nanosheets for Zinc-Ion Batteries. *Chem. Eng. J.* **2022**, *441*, 136008. [[CrossRef](#)]
44. Li, H.; Huang, Z.; Chen, B.; Jiang, Y.; Li, C.; Xiao, W.; Yan, X. A High-Performance MnO<sub>2</sub> Cathode Doped with Group VIII Metal for Aqueous Zn-Ion Batteries: In-Situ X-Ray Diffraction Study on Zn<sup>2+</sup> Storage Mechanism. *J. Power Sources* **2022**, *527*, 231198. [[CrossRef](#)]
45. Zhong, Y.; Xu, X.; Veder, J.-P.; Shao, Z. Self-Recovery Chemistry and Cobalt-Catalyzed Electrochemical Deposition of Cathode for Boosting Performance of Aqueous Zinc-Ion Batteries. *iScience* **2020**, *23*, 100943. [[CrossRef](#)]
46. Yang, S.; Zhang, L.; Luo, M.; Cui, Y.; Wang, J.; Zhao, D.; Yang, C.; Wang, X.; Cao, B. Synergistic Combination of a Co-Doped  $\sigma$ -MnO<sub>2</sub> Cathode with an Electrolyte Additive for a High-Performance Aqueous Zinc-Ion Battery. *ChemPhysMater* **2022**, *2*, 77–82. [[CrossRef](#)]
47. Zhao, Q.; Song, A.; Zhao, W.; Qin, R.; Ding, S.; Chen, X.; Song, Y.; Yang, L.; Lin, H.; Li, S.; et al. Boosting the Energy Density of Aqueous Batteries via Facile Grotthuss Proton Transport. *Angew. Chem.* **2021**, *133*, 4215–4220. [[CrossRef](#)]
48. Zhang, R.; Liang, P.; Yang, H.; Min, H.; Niu, M.; Jin, S.; Jiang, Y.; Pan, Z.; Yan, J.; Shen, X.; et al. Manipulating Intercalation-Extraction Mechanisms in Structurally Modulated  $\delta$ -MnO<sub>2</sub> Nanowires for High-Performance Aqueous Zinc-Ion Batteries. *Chem. Eng. J.* **2022**, *433*, 133687. [[CrossRef](#)]
49. Long, F.; Xiang, Y.; Yang, S.; Li, Y.; Du, H.; Liu, Y.; Wu, X.; Wu, X. Layered Manganese Dioxide Nanoflowers with Cu<sup>2+</sup> and Bi<sup>3+</sup> Intercalation as High-Performance Cathode for Aqueous Zinc-Ion Battery. *J. Colloid Interface Sci.* **2022**, *616*, 101–109. [[CrossRef](#)]
50. Liao, Y.; Yang, C.; Xu, Q.; Zhao, W.; Zhao, J.; Wang, K.; Chen, H.C. Ag-Doping Effect on MnO<sub>2</sub> Cathodes for Flexible Quasi-Solid-State Zinc-Ion Batteries. *Batteries* **2022**, *8*, 267. [[CrossRef](#)]
51. Zheng, Z.; Yang, G.; Yao, J.; Li, J.; Zheng, J.; Wu, Z.; Gan, Y.; Wang, C.; Lv, L.; Wan, H.; et al. High-Valence Molybdenum Promoted Proton Migration and Inhibited Dissolution for Long-Life Aqueous Zn-MnO<sub>2</sub> Batteries. *Appl. Surf. Sci.* **2022**, *592*, 153335. [[CrossRef](#)]
52. Wang, Z.; Han, K.; Wan, Q.; Fang, Y.; Qu, X.; Li, P. Mo-Pre-Intercalated MnO<sub>2</sub> Cathode with Highly Stable Layered Structure and Expanded Interlayer Spacing for Aqueous Zn-Ion Batteries. *ACS Appl. Mater. Interfaces* **2023**, *15*, 859–869. [[CrossRef](#)]
53. Zhang, H.; Liu, Q.; Wang, J.; Chen, K.; Xue, D.; Liu, J.; Lu, X. Boosting the Zn-Ion Storage Capability of Birnessite Manganese Oxide Nanoflorets by La<sup>3+</sup> Intercalation. *J. Mater. Chem. A* **2019**, *7*, 22079–22083. [[CrossRef](#)]
54. Wang, J.; Sun, X.; Zhao, H.; Xu, L.; Xia, J.; Luo, M.; Yang, Y.; Du, Y. Superior-Performance Aqueous Zinc Ion Battery Based on Structural Transformation of MnO<sub>2</sub> by Rare Earth Doping. *J. Phys. Chem. C* **2019**, *123*, 22735–22741. [[CrossRef](#)]
55. Song, Y.; Li, J.; Qiao, R.; Dai, X.; Jing, W.; Song, J.; Chen, Y.; Guo, S.; Sun, J.; Tan, Q.; et al. Binder-Free Flexible Zinc-Ion Batteries: One-Step Potentiostatic Electrodeposition Strategy Derived Ce Doped-MnO<sub>2</sub> Cathode. *Chem. Eng. J.* **2022**, *431*, 133387. [[CrossRef](#)]
56. Xu, J.; Hu, X.; Alam, M.A.; Muhammad, G.; Lv, Y.; Wang, M.; Zhu, C.; Xiong, W. Al-Doped  $\alpha$ -MnO<sub>2</sub> coated by Lignin for High-Performance Rechargeable Aqueous Zinc-Ion Batteries. *RSC Adv.* **2021**, *11*, 35280–35286. [[CrossRef](#)]
57. Zhou, S.; Wu, X.; Du, H.; He, Z.; Wu, X.; Wu, X. Dual Metal Ions and Water Molecular Pre-Intercalated  $\delta$ -MnO<sub>2</sub> Spherical Microflowers for Aqueous Zinc Ion Batteries. *J. Colloid Interface Sci.* **2022**, *623*, 456–466. [[CrossRef](#)] [[PubMed](#)]
58. Li, Y.; Zhang, H.; Tian, T.; Weng, Q.; Zan, L.; Zhao, S.; Liu, T.; Tang, Z.; Tang, H. Boosting High-Rate Zn-Ion Storage Capability of  $\alpha$ -MnO<sub>2</sub> through Tri-Ion Co-Intercalation. *J. Alloys Compd.* **2023**, *939*, 168813. [[CrossRef](#)]
59. Ma, Y.; Xu, M.; Liu, R.; Xiao, H.; Liu, Y.; Wang, X.; Huang, Y.; Yuan, G. Molecular Tailoring of MnO<sub>2</sub> by Bismuth Doping to Achieve Aqueous Zinc-Ion Battery with Capacitor-Level Durability. *Energy Storage Mater.* **2022**, *48*, 212–222. [[CrossRef](#)]
60. Wang, D.; Wang, L.; Liang, G.; Li, H.; Liu, Z.; Tang, Z.; Liang, J.; Zhi, C. A Superior  $\delta$ -MnO<sub>2</sub> Cathode and a Self-Healing Zn- $\delta$ -MnO<sub>2</sub> Battery. *ACS Nano* **2019**, *13*, 10643–10652. [[CrossRef](#)]
61. Kim, J.J.H.; Lee, J.; You, J.; Park, M.S.; Al Hossain, M.S.; Yamauchi, Y.; Kim, J.J.H. Conductive Polymers for Next-Generation Energy Storage Systems: Recent Progress and New Functions. *Mater. Horizons* **2016**, *3*, 517–535. [[CrossRef](#)]
62. Balint, R.; Cassidy, N.J.; Cartmell, S.H. Conductive Polymers: Towards a Smart Biomaterial for Tissue Engineering. *Acta Biomater.* **2014**, *10*, 2341–2353. [[CrossRef](#)]
63. Zhang, F.; Wang, C.; Pan, J.; Tian, F.; Zeng, S.; Yang, J.; Qian, Y. Polypyrrole-Controlled Plating/Stripping for Advanced Zinc Metal Anodes. *Mater. Today Energy* **2020**, *17*, 100443. [[CrossRef](#)]
64. Ciric-Marjanovic, G. Recent Advances in Polyaniline Research: Polymerization Mechanisms, Structural Aspects, Properties and Applications. *Synth. Met.* **2013**, *177*, 1–47. [[CrossRef](#)]
65. Huang, J.; Tu, J.; Lv, Y.; Liu, Y.; Huang, H.; Li, L.; Yao, J. Achieving Mesoporous MnO<sub>2</sub>@polyaniline Nanohybrids via a Gas/Liquid Interfacial Reaction between Aniline and KMnO<sub>4</sub> Aqueous Solution towards Zn-MnO<sub>2</sub> Battery. *Synth. Met.* **2020**, *266*, 116438. [[CrossRef](#)]
66. Huang, J.; Wang, Z.; Hou, M.; Dong, X.; Liu, Y.; Wang, Y.; Xia, Y. Polyaniline-Intercalated Manganese Dioxide Nanolayers as a High-Performance Cathode Material for an Aqueous Zinc-Ion Battery. *Nat. Commun.* **2018**, *9*, 2906. [[CrossRef](#)]
67. Mao, J.; Wu, F.-F.; Shi, W.-H.; Liu, W.-X.; Xu, X.-L.; Cai, G.-F.; Li, Y.-W.; Cao, X.-H. Preparation of Polyaniline-Coated Composite Aerogel of MnO<sub>2</sub> and Reduced Graphene Oxide for High-Performance Zinc-Ion Battery. *Chinese J. Polym. Sci.* **2020**, *38*, 514–521. [[CrossRef](#)]
68. Ruan, P.; Xu, X.; Gao, X.X.; Feng, J.; Yu, L.; Cai, Y.; Gao, X.X.; Shi, W.; Wu, F.; Liu, W.; et al. Achieving Long-Cycle-Life Zn-Ion Batteries through Interfacial Engineering of MnO<sub>2</sub>-Polyaniline Hybrid Networks. *Sustain. Mater. Technol.* **2021**, *28*, e00254. [[CrossRef](#)]
69. Li, N.; Hou, Z.; Liang, S.; Cao, Y.; Liu, H.; Hua, W.; Wei, C.; Kang, F.; Wang, J.G. Highly Flexible MnO<sub>2</sub>@polyaniline Core-Shell Nanowire Film toward Substantially Expedited Zinc Energy Storage. *Chem. Eng. J.* **2023**, *452*, 139408. [[CrossRef](#)]

70. Li, Y.; Liu, Y.; Chen, J.; Zheng, Q.; Huo, Y.; Xie, F.; Lin, D. Polyaniline Intercalation Induced Great Enhancement of Electrochemical Properties in Ammonium Vanadate Nanosheets as an Advanced Cathode for High-Performance Aqueous Zinc-Ion Batteries. *Chem. Eng. J.* **2022**, *448*, 137681. [CrossRef]
71. Zhang, Y.; Xu, L.; Jiang, H.; Liu, Y.; Meng, C. Polyaniline-Expanded the Interlayer Spacing of Hydrated Vanadium Pentoxide by the Interface-Intercalation for Aqueous Rechargeable Zn-Ion Batteries. *J. Colloid Interface Sci.* **2021**, *603*, 641–650. [CrossRef] [PubMed]
72. Li, R.; Xing, F.; Li, T.; Zhang, H.; Yan, J.; Zheng, Q.; Li, X. Intercalated Polyaniline in  $V_2O_5$  as a Unique Vanadium Oxide Bronze Cathode for Highly Stable Aqueous Zinc Ion Battery. *Energy Storage Mater.* **2021**, *38*, 590–598. [CrossRef]
73. Hao, L.; Yu, D. Progress of Conductive Polypyrrole Nanocomposites. *Synth. Met.* **2022**, *290*, 117138. [CrossRef]
74. Kausar, A. Overview on Conducting Polymer in Energy Storage and Energy Conversion System. *J. Macromol. Sci. Part A* **2017**, *54*, 640–653. [CrossRef]
75. Chavan, U.D.; Prajith, P.; Kandasubramanian, B. Polypyrrole Based Cathode Material for Battery Application. *Chem. Eng. J. Adv.* **2022**, *12*, 100416. [CrossRef]
76. Ruan, P.; Xu, X.; Feng, J.; Yu, L.; Gao, X.; Shi, W.; Wu, F.; Liu, W.; Zang, X.; Ma, F.; et al. Boosting Zinc Storage Performance via Conductive Materials. *Mater. Res. Bull.* **2021**, *133*, 111077. [CrossRef]
77. Morávková, Z.; Taboubi, O.; Minisy, I.M.; Bober, P. The Evolution of the Molecular Structure of Polypyrrole during Chemical Polymerization. *Synth. Met.* **2021**, *271*, 116608. [CrossRef]
78. Huang, J.; Tang, X.; Liu, K.; Fang, G.; He, Z.; Li, Z. Interfacial Chemical Binding and Improved Kinetics Assisting Stable Aqueous Zn– $MnO_2$  Batteries. *Mater. Today Energy* **2020**, *17*, 100475. [CrossRef]
79. Liao, X.; Pan, C.; Pan, Y.; Yin, C. Synthesis of Three-Dimensional  $\beta$ - $MnO_2$ /PPy Composite for High-Performance Cathode in Zinc-Ion Batteries. *J. Alloys Compd.* **2021**, *888*, 161619. [CrossRef]
80. Shen, X.; Wang, X.; Yu, N.; Yang, W.; Zhou, Y.; Shi, Y.; Wang, Y.; Dong, L.; Di, J.; Li, Q. A Polypyrrole-Coated  $MnO_2$ /Carbon Nanotube Film Cathode for Rechargeable Aqueous Zn-Ion Batteries. *Acta Phys. Chim. Sin.* **2020**, *38*, 2006059. [CrossRef]
81. Zhang, Y.; Xu, G.; Liu, X.; Wei, X.; Cao, J.; Yang, L. Scalable In Situ Reactive Assembly of Polypyrrole-Coated  $MnO_2$  Nanowire and Carbon Nanotube Composite as Freestanding Cathodes for High Performance Aqueous Zn-Ion Batteries. *ChemElectroChem* **2020**, *7*, 2762–2770. [CrossRef]
82. Niu, T.; Li, J.; Qi, Y.; Huang, X.; Ren, Y. Preparation and Electrochemical Properties of  $\alpha$ - $MnO_2$ /RGO-PPy Composite as Cathode Material for Zinc-Ion Battery. *J. Mater. Sci.* **2021**, *56*, 16582–16590. [CrossRef]
83. Huang, A.; Zhou, W.; Wang, A.; Chen, M.; Chen, J.; Tian, Q.; Xu, J. Self-Initiated Coating of Polypyrrole on  $MnO_2$ / $Mn_2O_3$  Nanocomposite for High-Performance Aqueous Zinc-Ion Batteries. *Appl. Surf. Sci.* **2021**, *545*, 149041. [CrossRef]
84. Xu, J.W.; Gao, Q.L.; Xia, Y.M.; Lin, X.S.; Liu, W.L.; Ren, M.M.; Kong, F.G.; Wang, S.J.; Lin, C. High-Performance Reversible Aqueous Zinc-Ion Battery Based on Iron-Doped Alpha-Manganese Dioxide Coated by Polypyrrole. *J. Colloid Interface Sci.* **2021**, *598*, 419–429. [CrossRef]
85. Wang, Z.; Ruan, Z.; Liu, Z.; Wang, Y.; Tang, Z.; Li, H.; Zhu, M.; Hung, T.F.; Liu, J.; Shi, Z.; et al. A Flexible Rechargeable Zinc-Ion Wire-Shaped Battery with Shape Memory Function. *J. Mater. Chem. A* **2018**, *6*, 8549–8557. [CrossRef]
86. Sun, K.; Zhang, S.; Li, P.; Xia, Y.; Zhang, X.; Du, D.; Isikgor, F.H.; Ouyang, J. Review on Application of PEDOTs and PEDOT:PSS in Energy Conversion and Storage Devices. *J. Mater. Sci. Mater. Electron.* **2015**, *26*, 4438–4462. [CrossRef]
87. Chen, H.W.; Li, C. PEDOT: Fundamentals and Its Nanocomposites for Energy Storage. *Chin. J. Polym. Sci. (Engl. Ed.)* **2020**, *38*, 435–448. [CrossRef]
88. Heywang, G.; Jonas, F. Poly(Alkylenedioxythiophene)s—New, Very Stable Conducting Polymers. *Adv. Mater.* **1992**, *4*, 116–118. [CrossRef]
89. Petsagkourakis, I.; Kim, N.; Tybrandt, K.; Zozoulenko, I.; Crispin, X. Poly(3,4-ethylenedioxythiophene): Chemical Synthesis, Transport Properties, and Thermoelectric Devices. *Adv. Electron. Mater.* **2019**, *5*, 1800918. [CrossRef]
90. Zeng, Y.; Zhang, X.; Meng, Y.; Yu, M.; Yi, J.; Wu, Y.; Lu, X.; Tong, Y. Achieving Ultrahigh Energy Density and Long Durability in a Flexible Rechargeable Quasi-Solid-State Zn– $MnO_2$  Battery. *Adv. Mater.* **2017**, *29*, 1700274. [CrossRef]
91. Zhang, X.; Wu, S.; Deng, S.; Wu, W.; Zeng, Y.; Xia, X.; Pan, G.; Tong, Y.; Lu, X. 3D CNTs Networks Enable  $MnO_2$  Cathodes with High Capacity and Superior Rate Capability for Flexible Rechargeable Zn– $MnO_2$  Batteries. *Small Methods* **2019**, *3*, 1900525. [CrossRef]
92. Shi, X.; Liu, X.; Wang, E.; Cao, X.; Yu, Y.; Cheng, X.; Lu, X. Boosting the Zn Ion Storage Ability of Amorphous  $MnO_2$  via Surface Engineering and Valence Modulation. *Carbon Neutraliz.* **2023**, *2*, 28–36. [CrossRef]
93. Fu, N.; Zhao, Q.; Xu, Y.; Wang, H.; Hu, J.; Wu, Y.; Yang, L.; Wu, X.; Zeng, X. Exploiting the Synergistic Effect of Multiphase  $MnO_2$  Stabilized by an Integrated Conducting Network for Aqueous Zinc-Ion Batteries. *Mater. Chem. Front.* **2022**, *6*, 1956–1963. [CrossRef]
94. Zhang, H.; Wang, J.; Liu, Q.; He, W.; Lai, Z.; Zhang, X.; Yu, M.; Tong, Y.; Lu, X. Extracting Oxygen Anions from  $ZnMn_2O_4$ : Robust Cathode for Flexible All-Solid-State Zn-Ion Batteries. *Energy Storage Mater.* **2019**, *21*, 154–161. [CrossRef]
95. Wang, L.; Wang, X.; Song, B.; Wang, Z.; Zhang, L.; Lu, Q. Facile in Situ Synthesis of PEDOT Conductor Interface at the Surface of  $MnO_2$  Cathodes for Enhanced Aqueous Zinc-Ion Batteries. *Surfaces and Interfaces* **2022**, *33*, 102222. [CrossRef]
96. Chen, H.; Ma, W.; Guo, J.; Xiong, J.; Hou, F.; Si, W.; Sang, Z.; Yang, D. PEDOT-Intercalated  $MnO_2$  Layers as a High-Performance Cathode Material for Aqueous Zn-Ion Batteries. *J. Alloys Compd.* **2023**, *932*, 167688. [CrossRef]

97. Kamenskii, M.A.; Volkov, F.S.; Eliseeva, S.N.; Holze, R.; Kondratiev, V.V. Comparative Study of PEDOT- and PEDOT:PSS Modified  $\delta$ -MnO<sub>2</sub> Cathodes for Aqueous Zinc Batteries with Enhanced Properties. *J. Electrochem. Soc.* **2023**, *170*, 010505. [[CrossRef](#)]
98. Chen, J.; Liang, J.; Zhou, Y.; Sha, Z.; Lim, S.; Huang, F.; Han, Z.; Brown, S.A.; Cao, L.; Wang, D.; et al. A Vertical Graphene Enhanced Zn–MnO<sub>2</sub> Flexible Battery towards Wearable Electronic Devices. *J. Mater. Chem. A* **2021**, *9*, 575–584. [[CrossRef](#)]
99. Kamenskii, M.A.; Eliseeva, S.N.; Kondratiev, V.V. The Electrochemical Performance of  $\delta$ -MnO<sub>2</sub> Cathode Material for Aqueous Zinc-Ion Batteries: The Role of Current Collector. *ECS Trans.* **2021**, *105*, 135–142. [[CrossRef](#)]
100. Yamamoto, T.; Shoji, T. Rechargeable Zn|ZnSO<sub>4</sub>|MnO<sub>2</sub>-Type Cells. *Inorg. Chim. Acta* **1986**, *117*, L27–L28. [[CrossRef](#)]
101. Xue, T.; Fan, H.J. From Aqueous Zn-Ion Battery to Zn–MnO<sub>2</sub> Flow Battery: A Brief Story. *J. Energy Chem.* **2021**, *54*, 194–201. [[CrossRef](#)]
102. Zhao, Y.; Zhu, Y.; Zhang, X. Challenges and Perspectives for Manganese-Based Oxides for Advanced Aqueous Zinc-Ion Batteries. *InfoMat* **2020**, *2*, 237–260. [[CrossRef](#)]
103. Fitz, O.; Bischoff, C.; Bauer, M.; Gentischer, H.; Birke, K.P.; Henning, H.M.; Biro, D. Electrolyte Study with in Operando pH Tracking Providing Insight into the Reaction Mechanism of Aqueous Acidic Zn//MnO<sub>2</sub> Batteries. *ChemElectroChem* **2021**, *8*, 3553–3566. [[CrossRef](#)]
104. Li, L.; Hoang, T.K.A.; Zhi, J.; Han, M.; Li, S.; Chen, P. Functioning Mechanism of the Secondary Aqueous Zn- $\beta$ -MnO<sub>2</sub> Battery. *ACS Appl. Mater. Interfaces* **2020**, *12*, 12834–12846. [[CrossRef](#)]
105. Aguilar, I.; Lemaire, P.; Ayouni, N.; Bendadesse, E.; Morozov, A.V.; Sel, O.; Balland, V.; Limoges, B.; Abakumov, A.M.; Raymundo-Piñero, E.; et al. Identifying Interfacial Mechanisms Limitations within Aqueous Zn–MnO<sub>2</sub> Batteries and Means to Cure Them with Additives. *Energy Storage Mater.* **2022**, *53*, 238–253. [[CrossRef](#)]
106. Wu, Y.; Zhi, J.; Han, M.; Liu, Z.; Shi, Q.; Liu, Y.; Chen, P. Regulating Proton Distribution by Ion Exchange Resin to Achieve Long Lifespan Aqueous Zn–MnO<sub>2</sub> Battery. *Energy Storage Mater.* **2022**, *51*, 599–609. [[CrossRef](#)]
107. Guo, X.; Zhou, J.; Bai, C.; Li, X.; Fang, G.; Liang, S. Zn/MnO<sub>2</sub> Battery Chemistry with Dissolution-Deposition Mechanism. *Mater. Today Energy* **2020**, *16*, 100396. [[CrossRef](#)]
108. Jin, Y.; Zou, L.; Liu, L.; Engelhard, M.H.; Patel, R.L.; Nie, Z.; Han, K.S.; Shao, Y.; Wang, C.; Zhu, J.; et al. Joint Charge Storage for High-Rate Aqueous Zinc–Manganese Dioxide Batteries. *Adv. Mater.* **2019**, *31*, 1900567. [[CrossRef](#)] [[PubMed](#)]
109. Li, Y.; Wang, S.; Salvador, J.R.; Wu, J.; Liu, B.; Yang, W.; Yang, J.; Zhang, W.; Liu, J.; Yang, J. Reaction Mechanisms for Long-Life Rechargeable Zn/MnO<sub>2</sub> Batteries. *Chem. Mater.* **2019**, *31*, 2036–2047. [[CrossRef](#)]
110. Zhou, T.; Zhu, L.; Xie, L.; Han, Q.; Yang, X.; Chen, L.; Wang, G.; Cao, X. Cathode Materials for Aqueous Zinc-Ion Batteries: A Mini Review. *J. Colloid Interface Sci.* **2022**, *605*, 828–850. [[CrossRef](#)] [[PubMed](#)]
111. Huang, Y.; Mou, J.; Liu, W.; Wang, X.; Dong, L.; Kang, F.; Xu, C. Novel Insights into Energy Storage Mechanism of Aqueous Rechargeable Zn/MnO<sub>2</sub> Batteries with Participation of Mn<sup>2+</sup>. *Nano-Micro Lett.* **2019**, *11*, 49. [[CrossRef](#)] [[PubMed](#)]
112. Guo, C.; Liu, H.; Li, J.; Hou, Z.; Liang, J.; Zhou, J.; Zhu, Y.; Qian, Y. Ultrathin  $\delta$ -MnO<sub>2</sub> Nanosheets as Cathode for Aqueous Rechargeable Zinc Ion Battery. *Electrochim. Acta* **2019**, *304*, 370–377. [[CrossRef](#)]
113. Liu, D.-S.; Mai, Y.; Chen, S.; Liu, S.; Ang, E.H.; Ye, M.; Yang, Y.; Zhang, Y.; Geng, H.; Li, C.C. A 1D–3D Interconnected  $\delta$ -MnO<sub>2</sub> Nanowires Network as High-Performance and High Energy Efficiency Cathode Material for Aqueous Zinc-Ion Batteries. *Electrochim. Acta* **2021**, *370*, 137740. [[CrossRef](#)]
114. Zhou, W.; Wang, A.; Huang, A.; Chen, M.; Tian, Q.; Chen, J.; Xu, X. Hybridizing  $\delta$ -Type MnO<sub>2</sub> With Lignin-Derived Porous Carbon as a Stable Cathode Material for Aqueous Zn–MnO<sub>2</sub> Batteries. *Front. Energy Res.* **2020**, *8*, 182. [[CrossRef](#)]
115. Liao, Y.; Chen, H.C.; Yang, C.; Liu, R.; Peng, Z.; Cao, H.; Wang, K. Unveiling Performance Evolution Mechanisms of MnO<sub>2</sub> Polymorphs for Durable Aqueous Zinc-Ion Batteries. *Energy Storage Mater.* **2022**, *44*, 508–516. [[CrossRef](#)]
116. Siamionau, U.; Aniskevich, Y.; Mazanik, A.; Kokits, O.; Ragoisha, G.; Jo, J.H.; Myung, S.T.; Streltsov, E. Rechargeable Zinc-Ion Batteries with Manganese Dioxide Cathode: How Critical Is Choice of Manganese Dioxide Polymorphs in Aqueous Solutions? *J. Power Sources* **2022**, *523*, 231023. [[CrossRef](#)]
117. Stoševski, I.; Bonakdarpour, A.; Fang, B.; Lo, P.; Wilkinson, D.P. Formation of Mn<sub>x</sub>Zn<sub>y</sub>(OH)<sub>z</sub>SO<sub>4</sub>·5H<sub>2</sub>O—Not Intercalation of Zn—Is the Basis of the Neutral MnO<sub>2</sub>/Zn Battery First Discharge Reaction. *Electrochim. Acta* **2021**, *390*, 138852. [[CrossRef](#)]
118. Liu, Z.; Yang, Y.; Liang, S.; Lu, B.; Zhou, J. pH-Buffer Contained Electrolyte for Self-Adjusted Cathode-Free Zn–MnO<sub>2</sub> Batteries with Coexistence of Dual Mechanisms. *Small Struct.* **2021**, *2*, 2100119. [[CrossRef](#)]
119. Efremova, A.O.; Volkov, A.I.; Tolstopyatova, E.G.; Kondratiev, V.V. EQCM Study of Intercalation Processes into Electrodeposited MnO<sub>2</sub> Electrode in Aqueous Zinc-Ion Battery Electrolyte. *J. Alloys Compd.* **2022**, *892*, 162142. [[CrossRef](#)]
120. Kim, S.J.; Wu, D.; Sadique, N.; Quilty, C.D.; Wu, L.; Marschilok, A.C.; Takeuchi, K.J.; Takeuchi, E.S.; Zhu, Y. Unraveling the Dissolution-Mediated Reaction Mechanism of  $\alpha$ -MnO<sub>2</sub> Cathodes for Aqueous Zn-Ion Batteries. *Small* **2020**, *16*, 2005406. [[CrossRef](#)]
121. Han, S.D.; Kim, S.; Li, D.; Petkov, V.; Yoo, H.D.; Phillips, P.J.; Wang, H.; Kim, J.J.; More, K.L.; Key, B.; et al. Mechanism of Zn Insertion into Nanostructured  $\delta$ -MnO<sub>2</sub>: A Nonaqueous Rechargeable Zn Metal Battery. *Chem. Mater.* **2017**, *29*, 4874–4884. [[CrossRef](#)]

**Disclaimer/Publisher’s Note:** The statements, opinions and data contained in all publications are solely those of the individual author(s) and contributor(s) and not of MDPI and/or the editor(s). MDPI and/or the editor(s) disclaim responsibility for any injury to people or property resulting from any ideas, methods, instructions or products referred to in the content.